Institute of Physics

Doctoral Thesis

Viscoelastic and plastic characterization of cellulosic materials on the submicrometer scale

Dipl.-Ing. Caterina Marina Czibula

April 2020

ii

AFFIDAVIT

I declare on oath that I wrote this thesis independently, did not use other than the specified sources and aids, and did not otherwise use any unauthorized aids.

I declare that I have read, understood, and complied with the guidelines of the senate of the Montanuniversitaet Leoben for "Good Scientific Practice".

Furthermore, I declare that the electronic and printed version of the submitted thesis is identical, both, formally and with regard to content.

Date 20.04.2020

_____
Signature Author
Caterina Czibula
Matriculation Number: 00835114

Abstract

Cellulosic fibers are extensively used in paper and textile industries, but structure-property relations on the fiber scale are quite complicated and not yet fully understood. Changes in moisture content of single fibers have a strong impact on the physical properties and performance of paper. Therefore, it is of considerable interest to characterize the time dependency of the mechanical properties of single pulp fibers. In particular, the viscoelastic behavior of single pulp fibers, especially in the transverse direction of the fibers, has not been thoroughly studied in literature so far. One reason is that it is difficult to access the transverse direction with available experimental methods.

Most industrial cellulosic fibers are processed wood fibers, which consist of several cell wall layers that differ in thickness, chemical composition, and alignment of cellulose microfibrils. The S2 layer, where the cellulose microfibrils arrange in an angle close to the longitudinal axis, is the thickest layer. Therefore, this layer dominates the mechanical behavior of the fibers, especially in longitudinal direction. Several investigations with depth-sensing methods have focused on the characterization of the mechanical properties of the S2 layer. However, studies on the influence of relative humidity (RH) and the viscoelastic behavior of this layer are still missing.

Furthermore, wood pulp fibers have not only anisotropic properties but also exhibit a very rough surface due to their severe shrinkage in the production process. For this reason, an atomic force microscopy (AFM) method was developed here to overcome the limitations of conventional nanoindentation. The high roughness of the surface influences the contact between the AFM tip and the sample surface which should not be ignored. To provide, therefore, comparable results of local viscoelastic properties in longitudinal and transverse direction at different RH and in water, an experimental protocol needed to be established to reduce the roughness of the pulp fibers. The evaluation of the experimental data combines contact mechanics in the form of the Johnson-Kendall-Roberts (JKR) model and viscoelastic models, which consist of springs and dashpots in series or parallel describing elastic and viscous behavior, respectively. It will be demonstrated that the so-called Generalized Maxwell model (GM) yields reasonable results for single fibers – viscose and pulp fibers – at different RH values and in water in transverse direction. The experimental curves have been fitted with a GM2 model. With increasing RH – starting at 10 % RH until 75 % RH – the elastic and the viscous parameters are decreasing, whereas

the relaxation times stay constant. In water, the GM3 model with an additional Maxwell element – introducing a third relaxation time – is used to fit the data properly. Compared to the results at different RH, the values of the elastic and viscous parameters show a pronounced drop in values of a few orders of magnitude.

Furthermore, microtome cuts of the S2 layer are chemically and morphologically characterized. The viscoelastic properties from 25 % RH to 75 % RH are studied, and transverse and longitudinal direction are compared. Here, the GM3 model was applied to fit the experimental data for the S2 layer in longitudinal direction accurately. The same trend of decreasing parameters is found for the longitudinal as previously for the transverse direction.

Additionally, the suitability of the experimental results for material modeling is presented. Experimental AFM indentation data can be used for the viscoelastic characterization of the matrix material in a minimum-input material model of the pulp fiber. This model is based on an incompressibility constraint. It can be applied in paper network simulations and for fibers in the dry state, if compressibility is not important.

The influence of RH is further investigated with bending experiments of cellulose thin films. A cantilever coated with a cellulose film on one side will bend upwards due to the swelling of the cellulose film if the RH is increased. This effect is visible on a short-time scale. However, on a long-time scale, the behavior gets more complicated and is also reproducible with an uncoated cantilever, leaving open questions.

Besides cellulose-water interaction, the frictional behavior and morphology of different cellulose blend films are studied as well and are compared. The morphology changes due to phase separation of the different blend film ratios are investigated. Furthermore, the applicability of friction force microscopy (FFM) to obtain semi-quantitatively mechanical parameters of cellulose blend films is demonstrated. It is revealed that it is possible by blending to tune the frictional, morphological, and mechanical properties of such films.

Kurzfassung

Cellulosefasern werden in Papier- und Textilindustrie häufig verwendet, aber Struktur-Eigenschafts-Beziehungen auf der Faserskala sind ziemlich kompliziert und noch nicht vollständig verstanden. Änderungen des Feuchtigkeitsgehalts von Einzelfasern haben einen starken Einfluss auf die physikalischen Eigenschaften und das Verhalten von Papier. Daher ist es von erheblichem Interesse, die Zeitabhängigkeit der mechanischen Eigenschaften einzelner Zellstofffasern zu charakterisieren. Insbesondere das viskoelastische Verhalten einzelner Zellstofffasern, vor allem in Querrichtung der Fasern, wurde in der Literatur bisher nicht gründlich untersucht. Ein Grund ist, dass es mit den verfügbaren experimentellen Methoden schwierig ist, auf die Querrichtung zuzugreifen.

Die meisten industriellen Cellulosefasern sind verarbeitete Holzfasern, die aus mehreren Zellwandschichten bestehen, welche sich in Dicke, chemischer Zusammensetzung und Ausrichtung der Cellulosemikrofibrillen unterscheiden. Die S2-Schicht, in der die Cellulosemikrofibrillen in einem Winkel nahe der Längsachse angeordnet sind, ist die dickste Schicht. Daher dominiert diese Schicht das mechanische Verhalten der Fasern, insbesondere in Längsrichtung. Mehrere Untersuchungen mit Nanoindentations-Methoden haben sich auf die Charakterisierung der mechanischen Eigenschaften der S2-Schicht konzentriert. Studien zum Einfluss der relativen Luftfeuchtigkeit (RH) und zum viskoelastischen Verhalten dieser Schicht fehlen jedoch noch.

Darüber hinaus weisen Zellstofffasern nicht nur anisotrope Eigenschaften auf, sondern aufgrund ihres starken Schrumpfens im Produktionsprozess auch eine sehr raue Oberfläche. Aus diesem Grund wurde hier eine Rasterkraftmikroskopie (AFM)-Methode entwickelt, um die Einschränkungen der konventionellen Nanoindentation zu überwinden. Die hohe Rauheit der Oberfläche hat einen Einfluss auf den Kontakt zwischen der AFM-Spitze und der Probenoberfläche, der nicht ignoriert werden sollte. Um daher vergleichbare Ergebnisse lokaler viskoelastischer Eigenschaften in Längs- und Querrichtung bei unterschiedlicher RH und in Wasser zu messen, musste ein experimentelles Protokoll erstellt werden, um die Rauheit der Zellstofffasern zu verringern. Die Auswertung der experimentellen Daten kombiniert Kontaktmechanik in Form des Johnson-Kendall-Roberts (JKR)-Modells und viskoelastische Modelle, die aus Federn und Dämpfern in Reihe oder parallel zueinander bestehen und das elastische bzw.

viskose Verhalten beschreiben. Es wird gezeigt, dass das sogenannte Generalized Maxwell-Modell (GM) vernünftige Ergebnisse für Einzelfasern – Viskose- und Zellstofffasern – bei unterschiedlicher RH und in Wasser in Querrichtung liefert. Die experimentellen Kurven wurden mit einem GM2-Modell gefittet. Mit zunehmender RH – beginnend bei 10% RH bis 75% RH – nehmen die elastischen und viskosen Parameter ab, während die Relaxationszeiten konstant bleiben. In Wasser wird das GM3-Modell mit einem zusätzlichen Maxwell-Element – das eine dritte Relaxationszeit einführt – verwendet, um die Daten richtig zu fitten. Im Vergleich zu den Ergebnissen bei unterschiedlicher RH zeigen die Werte der elastischen und viskosen Parameter in Wasser einen deutlichen Abfall um einige Größenordnungen.

Weiters werden Mikrotomschnitte der S2-Schicht chemisch und morphologisch charakterisiert. Die viskoelastischen Eigenschaften von 25% RH bis 75% RH werden untersucht und die Quer- und Längsrichtung verglichen. Hier wurde das GM3-Modell angewendet, um die experimentellen Daten für die S2-Schicht in Längsrichtung genau zu fitten. Für die Längsrichtung zeigt sich der gleiche Trend abnehmender Parameter wie zuvor für die Querrichtung.

Zusätzlich wird die Eignung der experimentellen Ergebnisse für die Materialmodellierung vorgestellt. Experimentelle AFM-Nanoindentationsdaten können zur viskoelastischen Charakterisierung des Matrixmaterials in einem Materialmodell der Zellstofffaser mit minimalem Input verwendet werden. Dieses Modell basiert auf einer Inkompressibilitätsbeschränkung. Es kann in Papiernetzwerksimulationen und auch für Fasern im trockenen Zustand angewendet werden, solange die Kompressibilität nicht wichtig ist.

Der Einfluss der relativen Luftfeuchtigkeit wird mit Biegeexperimenten an Cellulosedünnfilmen weiter untersucht. Ein Cantilever, der auf einer Seite mit einem Cellulosefilm beschichtet ist, biegt sich aufgrund der Quellung des Cellulosefilms nach oben, wenn die relative Luftfeuchtigkeit erhöht wird. Dieser Effekt ist in kurzer Zeit sichtbar. Auf einen längeren Zeitraum hin wird das Verhalten jedoch komplizierter und ist auch mit einem unbeschichteten Cantilever reproduzierbar, so dass offene Fragen bleiben.

Neben der Cellulose-Wasser-Wechselwirkung werden auch das Reibungsverhalten und die Morphologie verschiedener Cellulose-Blendfilme untersucht und verglichen. Die Morphologieänderungen aufgrund der Phasentrennung der verschiedenen Mischfilmverhältnisse werden untersucht. Darüber hinaus wird die Anwendbarkeit der

Reibungskraftmikroskopie (FFM) zum Erhalt semi-quantitativer mechanischer Parameter von Cellulose-Blendfilmen demonstriert. Es zeigt sich, dass es durch Mischen möglich ist, die Reibung sowie die morphologischen und mechanischen Eigenschaften solcher Filme zu beeinflussen.

Abbreviations

AFM	Atomic force microscop(e/y)
AFM-NI	AFM-based nanoindentation
AM-AFM	Amplitude modulated-AFM
BLSM	Brillouin light scattering microspectroscopy
CS_2	Carbon disulfide
DP	Degree of polymerization
FFM	Friction force microscopy
FM-AFM	Frequency modulated-AFM
GMA	Glycolmethacrylate
GMn	Generalized Maxwell model of order n
H_2O	Water
H_2SO_4	Sulphuric acid
HCl	Hydrochloric acid
HPCE	Hydroxypropyl cellulose stearate
JKR	Johnson-Kendall-Roberts
L	Lumen
LB	Langmuir-Blodgett
LFM	Lateral Force Microscopy
MFA	Microfibril angle
ML	Middle lamella
NaOH	Sodium hydroxide
NI	Nanoindentation
PDMS	Polydimethylsiloxane
PMMA	Polymethylmethacrylate
PC	Polycarbonate
P	Primary layer
RH	Relative humidity
RMS	Root mean square roughness
S1	Secondary 1 layer
S2	Secondary 2 layer
S3	Secondary 3 layer
SLS	Standard Linear Solid
TMSC	Trimethylsilyl cellulose
UHV	Ultra-high vacuum

Table of content

1 Motivation

Cellulosic fibers are essential for our daily life. Without wood as a construction and building material, society as we know it would hardly exist. An example of the daily use of lignocellulosic fibers by modern society are paper products: From office paper to packaging of our online orders, from food delivery to hygienic products, paper has multiple applications. Still, the knowledge of the mechanical behavior of the tiny fibers – in particular, in a humid environment – is limited.

Cellulosic fibers find not only application in paper, but also in nonwovens, fiber composites, hygiene products, textiles, and garments. With a bio-based economy driving the replacement of oil-based polymer materials, the applications for cellulosic fibers will increase and gain even more importance.

Mechanical modeling is nowadays an essential component of product development. However, material models need to be verified by carefully designed experiments. Therefore, it is of considerable interest to gain more experimental insight on how mechanical properties of cellulose fibers are related to properties of end-products like paper.

1.1   Micromechanical characterization

Apart from the complex cell wall structure, the geometrical dimensions (width: 20-50 µm, length: 1-3 mm) of cellulose fibers are limiting factors. This leads to difficulties in handling the individual fibers experimentally. Therefore, the investigation of individual cellulosic fibers is not straightforward, especially in transverse direction [1] and even more so for shear deformations [1],[2]. Most mechanical investigations of single fibers only focus on the longitudinal direction. In recent years, the utilization of depth-sensing instruments like nanoindentation (NI) led to the investigation of mechanical properties on the level of the cell wall. The S2 layer of wood and pulp fibers has been thoroughly studied with NI [3]–[7].

With atomic force microscopy (AFM)-based methods, accessing the surface of the single fibers on the nanoscale became possible. Starting with morphological surface

investigation, AFM has been adapted and established for the investigation of single fibers and has lately been increasingly used for mechanical characterization as well. With AFM-based methods, the influence of relative humidity (RH) on single pulp fibers [8],[9] as well as the strength of fiber-fiber bonds [10] have been studied. Furthermore, fiber-fiber joint strength [11],[12] has been characterized and the mechanisms of fiber-fiber bonds have been revealed [13].

1.2 Viscoelasticity

It is known that viscoelasticity plays a major role for paper products, but there is no information available on the level of a single fiber. In paper production and processing, there are varying speeds. Dynamic loading is very common during some end-use scenarios of paper like printing and converting. Mechanical simulation of paper converting and end-use processes are becoming an increasingly relevant tool in the paper industry. Cellulosic fibers are hygroscopic, and with increasing moisture content, the fibers become softer. This makes it necessary to cover a range of different humidity levels during experiments and in the ideal case, also to measure in water.

1.3 This work

In this thesis, several AFM-based methods are used to investigate the mechanical behavior of cellulosic materials. The main focus of this work is a method to characterize the viscoelastic properties of pulp fibers as a function of RH in different directions related to the long fiber axis. Here, an AFM-based experiment has been developed and validated with well-known polymers and established methods. Furthermore, the experimental data has been applied to establish a minimum-input material model for single pulp fibers based on an incompressibility constraint. The influence of hygroscopicity has been tested with thin cellulose films deposited on AFM tipless cantilevers by recording the cantilever at different relative humidity. Finally, the morphology and frictional behavior of cellulose blend films have been studied.

2

2 Theoretical background

2.1 Wood fibers

All cellulose fibers investigated in this work originated from wood. What is referred to as wood, is also called the secondary xylem in biological terms. These are cells or fibers which are mostly responsible for structural support and water transport between the soil and the leaves. Wood fibers have a hierarchical organization of polymer composites involving mainly cellulose, hemicellulose, and lignin. On the molecular level, cellulose, hemicellulose and lignin aggregate to form larger structures. Here, cellulose is the main structural polymer and forms microfibrils. Hemicellulose and lignin act as reinforcement and glue around the cellulose microfibrils, forming the matrix of the polymer composite and lignin is furthermore contributing to the compressive strength of wood. The result is a multi-layered cell wall structure where each layer differs in cellulose microfibril alignment, chemical composition, and thickness. Wood fibers, called tracheids in softwood, provide strength and transport water and nutrients in trees. To guarantee a continuous flow of water from the root up to the leaf, the fibers need to be interconnected with each other which is provided by so-called bordered pits. Since in this work only softwood fibers are considered, the discussion will focus on tracheid cells, which are the dominant cell type in softwood.

Main components of wood fibers: cellulose, hemicelluloses, and lignin

Cellulose is the main structural polymer of plant fibers. As illustrated in Figure 2.1a, it is a linear polysaccharide with a high degree of polymerization (DP) of up to 15 000 and consists of glucose monomer units, which are alternately rotated 180°. The cellulose molecules align to form microfibrils, with a diameter of just a few nanometers. These microfibrils consist of crystalline and non-crystalline regions which further align themselves into fibril aggregates or so-called microfibrils with a diameter of about 20 nm. The microfibrils also contain a matrix of hemicelluloses and lignin [14]. Unlike cellulose, the matrix polysaccharides are less ordered, and their non-crystalline character is a consequence of their branching structure. However, there is a partial order because these polymers tend to align along the long axis of cellulose [15],[16]. Hemicelluloses are short-

3

chain, amorphous polysaccharides with a much lower DP and a greater solvent reactivity than cellulose. They are branched and consist of several different types of cyclic sugars and glucuronic acids which leads to a large diversity. The most common hemicelluloses include xyloglucans, xylans, glucomannans, and galactoglucomannans [14]. In Figure 2.1b, the heterogeneous chemical structure of hemicellulose is represented schematically. Lignin is a highly branched polymer of phenylpropanoid groups. The units of lignin form a complex, three-dimensional structure, as illustrated in Figure 2.1c, and there is a lot of structural variation of lignin for the single-cell wall, plant organs as well as plant species. The mechanical rigidity of lignin plays an important role in the upward growth of plants and the conduction of water and minerals through the xylem under negative pressure without collapse of the tissue. Additionally, it contains protective functions against fungi and animals [15].
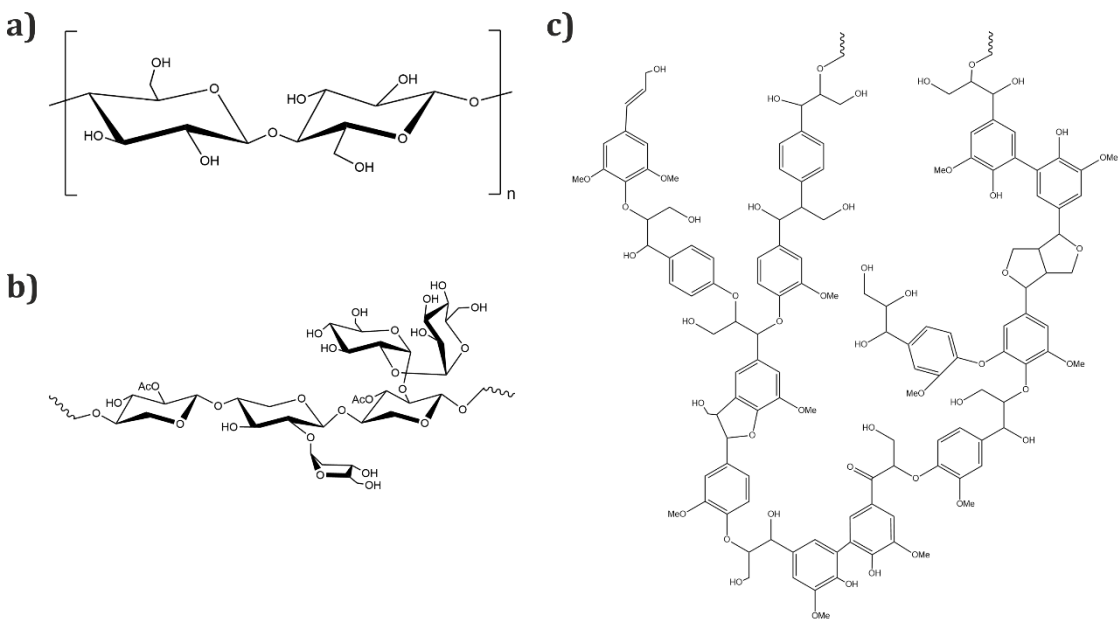

Figure 2.1: Chemical structures of (a) cellulose, (b) hemicellulose (adapted from [17]), and (c) lignin (adapted from [18]).

Cell wall formation

Wood cells form and grow in the so-called cambium layer right under the bark of the tree. Within only a few weeks, the cells grow to their mature dimensions with secondary layers being formed and lignified. Cellulose microfibrils are synthesized by protein complexes, which are called particle rosettes or terminal complexes, and are embedded in

the plasma membrane. During cellulose microfibril synthesis, the microfibrils are deposited into the wall which contains a high concentration of other polysaccharides. Hemicelluloses such as xyloglucan and xylan can interact with – and perhaps modify – the growing microfibril. There are indications that some hemicelluloses might get trapped within the microfibril during its formation, leading to a reduction of the crystallinity and the order in the microfibril. The matrix itself is a highly hydrated phase in which the cellulose microfibrils are embedded. The primary (P) wall starts getting formed by growing cells in the final stages of cell division and after wall formation, the growth process includes several steps: synthesis, secretion, assembly, expansion (in growing cells), cross-linking, and secondary (S) wall formation. The assembly of the polymers in the wall is crucial since the arrangement and bonding between the polysaccharides is determining the physical properties of the cell wall. However, the details of wall assembly are still not fully understood. After the expansion of the growing cells stops, the cells continue to synthesize a wall, which is known as S wall. It differs in structure and composition from the P wall. In wood, the S wall contains a higher amount of cellulose; xylans are preferred instead of xyloglucans and the wall is impregnated with lignin. The formation of lignin in the wall displaces water from the matrix due to lignin's hydrophobic character. S walls are quite thick and, therefore, offer mechanical support for the tree [15],[19].

The hierarchical structure of wood fibers

Wood cells are hollow, layered structures consisting of a P cell wall, which is surrounded by a middle lamella (ML) on the outside and an S cell wall on the inside. The hollow center of the fibers is called lumen (L) [20]. In this hierarchical structure, which is sketched in Figure 2.2b, the cell wall layers are responsible for the mechanical strength of the fiber whereas the L provides water and nutrients transport in the living tree. The thin, lignin-rich ML mostly acts as a glue between adjacent cells. The P cell wall is lignin-rich and thin, containing randomly oriented cellulose microfibrils. The S cell wall has three different layers (S1, S2, S3) which differ in chemical composition, alignment of the cellulose microfibrils, and layer thickness.
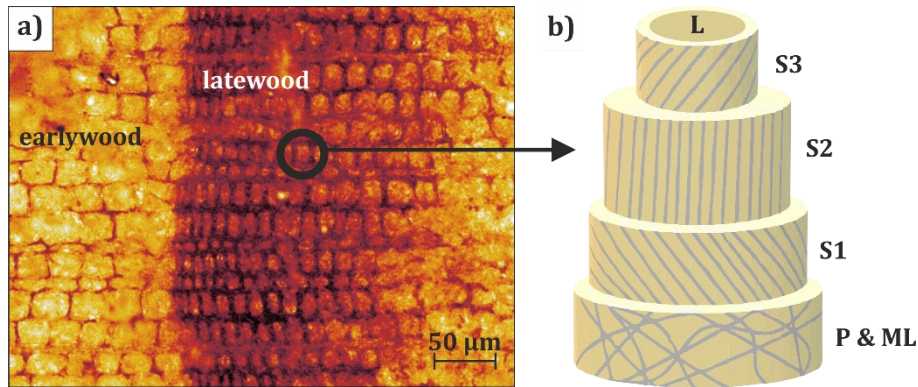
Figure 2.2. (a) Optical micrograph of a wood piece cut in longitudinal direction. Cross-sections of fibers with thin cell walls and large lumen (earlywood) and with thick walls and smaller lumen (latewood) can be seen. In (b), the different cell wall layers (middle lamella ML, primary layer P, secondary layers S1, S2, S3) and the lumen L for an individual wood fiber are illustrated. After [14],[16].

In the S layer, the S1 layer is slightly thicker than the P cell wall, and the microfibrils are wound circumferentially around the cell wall. It is common to describe the orientation of the microfibrils in relation to the long fiber axis with the so-called microfibrillar angle (MFA). In the S1 layer, the MFA is usually > 60° [20]. As can be seen in Table 1, the S2 layer accounts for most of the thickness of the cell wall, whereas the other layers are quite thin and together less than 500 nm in thickness. For example, in Norway spruce, the S2 layer contributes to about 80 percent of the cell wall [14]. It also contains the highest amount of cellulose and the microfibrils in the S2 layer are arranged in a right-handed helix with an MFA of 5-25°. Finally, the S3 layer is slightly thinner than the S1, having also a similarly high MFA. The transition between the different S layers is probably not abrupt, but there are reported to be transition layers between S1/S2 and S2/S3 [21].

Table 1: Estimated values for the different cell wall layer thicknesses of the fiber. After [22].

Cell wall layer thicknesses / μm	
Middle lamella	≥ 0.1
Primary cell wall (P)	0.03
S1	0.2
S2	≥ 5
S3	0.07-0.08

6

Woods can be grouped in softwoods, which are called gymnosperms and hardwoods, which are called angiosperms. In softwood, two types of cells exist: the longitudinally aligned tracheids or fibers which make up 85-95 % of the wood, and rays, which connect the tracheids radially and contribute up to 15 % to the wood [14]. Tracheids/fibers in softwood provide channels for water transport in their lumen, and the thick lignified cell wall is responsible for the tree's mechanical stability. Water needs to be transported from the root to the leaf through the fibers, therefore, a lumen inside the fiber is not sufficient, since the fibers need to be also laterally connected. This is possible due to small openings in the fiber cell wall which are called bordered pits in softwood. In Figure 2.3a, an optical micrograph depicts a tangential cut of a wood piece. In this top view of a softwood fiber, bordered pits are visible. Figure 2.3b illustrates the bordered pit in side view. A bordered pit pair has pit apertures between two adjacent longitudinal fibers. Each bordered pit pair encloses a web-like microfibril structure called a margo that supports a central and much less permeable torus. This assembly acts as a valve to open or close the openings between the fibers [20]. This is crucial for the survival of the tree. Bordered pit membranes create a porous boundary between adjacent fibers, that prevents the spread of so-called embolism. Embolism is the hydraulic disconnection of leaves and roots due to fibers that are filled with air and water vapor. This halts water transport and ultimately causes plant death [15],[23],[24]. Pits differ in geometrical shape with species and can be used to identify and differentiate different types of fibers [25].
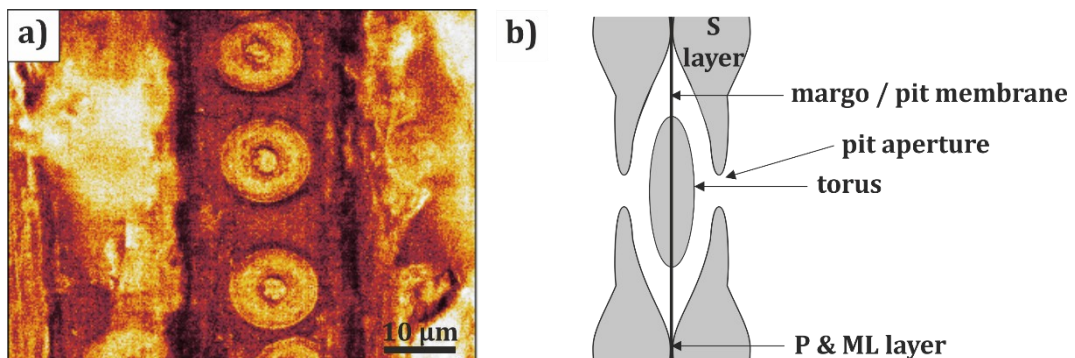

Figure 2.3: (a) Optical micrograph of a softwood fiber with bordered pits from a softwood sample cut in tangential direction (top view). (b) Sideview of a bordered pit, showing the typical structural components. The S layer is disconnected at the pit aperture and the P and ML layer form a membrane-like structure composed of torus and margo. After [15].

2.1.1 Pulp fibers

For paper production, wood cells first need to be extracted from the wood. This can be achieved by mechanical, chemical or combined methods. These processes are referred to as pulping processes and the separated wood cells are called pulp fibers. In chemical pulping, wood is disintegrated chemically into fibers by cooking wood chips. Very common is the so-called kraft (sulfate) process. In this pulping process, lignin is removed chemically from the wood, leading to the separation into single fibers. Due to the loss of hemicelluloses and lignin, the matrices of the pulp fibers are weakened which can often result in fiber collapse. So much matrix material is removed that the structure is not stable anymore and instead of a donut-like structure, the cell walls get pressed together and, in many cases, the lumen is completely gone. Thinner cell walls collapse more easily, therefore, earlywood fibers show less resistance to collapsing than latewood fibers. Often the lignin-rich P and S1 layers are lost in pulping. In general, pulping, and further process steps like bleaching and beating have a crucial effect on the pulp properties. Possible defects of the cell wall of a pulp fiber include inhomogeneities such as dislocations and micro-compressions. From the chipping of wood up to the paper machine, defects can arise and especially deformations in the axial direction of fibers like kinks, folds and twists are additional weak points [26]. Of course, further inhomogeneities are caused by the wooden material used itself, if one considers the differences between species, where spruce has, e. g., a different pit structure compared to pine. Variations are given in between the same species too if one considers the different cell features of earlywood and latewood.

2.1.2 Viscose fibers

Viscose fibers are used in everyday life, e. g., in textiles and hygiene articles. Even for research purposes, viscose fibers proved to be a good model system for investigations of more complex pulp fibers [27]. The viscose process is based on the derivatization of cellulose using carbon disulfide (CS_2). First, the pulp is treated with sodium hydroxide (NaOH) to form sodium cellulose. During xanthation, the swollen alkali cellulose reacts with CS_2 to form sodium cellulose xanthate, which is soluble in aqueous NaOH. After

dissolving the sodium cellulose xanthate in 5-8 % aqueous NaOH, a yellow cellulose xanthate solution, which is called viscose dope, is formed. The dissolved cellulose xanthate is extruded through a spinneret into a coagulation bath containing mostly sulphuric acid (H_2SO_4) to obtain a fiber and to convert cellulose xanthate into cellulose. The shape of the fibers' cross-section is determined by the holes in the spinneret and can be varied. To increase the tenacity of the fibers, the viscose fibers are stretched to orientate the cellulose molecule chains along the fiber axis [28]. In contrast to cellulose in wood fibers, the cellulose in viscose fibers exhibits a different crystalline structure. The crystalline wood cellulose is called cellulose I whereas the regenerated crystalline cellulose is cellulose II and believed to be thermodynamically more stable [29]. Furthermore, the DP of cellulose in viscose is only approximately 300, which is much lower than in pulp fibers (DP ≈ 1000 to 2000) [30]–[32]. The fraction of crystalline domains in viscose fibers is reported to vary between 30 % and 50 % and strongly depends on process parameters and modifications [28]. In contrast to wood fibers, viscose fibers do not exhibit a complex hierarchical structure like wood fibers, but a skin-core structure that can be also controlled and adjusted by variations of process parameters. Compositional modifications are achieved by adding substances directly into the viscose dope [28].

2.1.3 Cellulose thin films

Cellulose is known for its insolubility but, in industrial fiber production, e. g., in the viscose process, cellulose insolubility has been circumvented by a derivatization procedure followed by conversion to cellulose which is also called regeneration. Similar approaches involving derivatization, dissolution, film formation, and regeneration of the derivatized film to cellulose have been also applied for thin film fabrication [33],[34]. Cellulose thin films can be used as a model system for studying pulp fiber properties [8],[35] but are also interesting for protein adsorption studies [36],[37]. The solubility of cellulose is poor which is an issue with thin film preparation. For cellulose thin films, two deposition methods are dominating: spin coating and Langmuir-Blodgett (LB) deposition [38]. In spin coating, the solution is deposited at high speed onto a substrate. The procedure is very easy and reproducible. In LB deposition, a solution of the to-be-coated substance is first deposited on water to have time for the solvent to evaporate. In the

second step, a monolayer thin film of the floating substance is formed on the water. By dipping a solid substrate through the monolayer thin film, ideally, a monomolecular film is deposited on the substrate. The film thickness can be tuned by the number of dips [38]. In this work, spin coating is the method of choice. Here, the highly soluble cellulose derivative trimethylsilyl cellulose (TMSC), as illustrated in Figure 2.4, dissolved in toluene or chloroform is used to serve as a precursor for single-component cellulose but it can be used for blend films as well [36],[39],[40]. The regeneration to cellulose takes place by exposing the TMSC films to hydrochloric acid vapor [33].
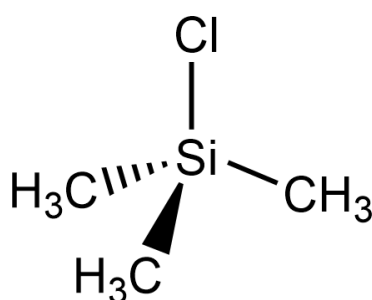

Figure 2.4: Chemical structure of trimethylsilyl cellulose (TMSC) (adapted from [41]) .

2.2 Mechanical properties of cellulose fibers

Cellulose dominates the strength properties of wood fibers. Many theoretical and experimental data have determined a longitudinal elastic modulus of crystalline cellulose, at about 140-150 GPa. The mechanical properties in the longitudinal fiber direction are mostly influenced by the S2 layer due to its thickness and cellulose microfibril alignment. Usually, the MFA is in the range of 5-10° and less than 30° and makes the fiber highly anisotropic [16]. A higher MFA in the S2 layer decreases the longitudinal elastic modulus and tensile strength of the cell wall. For example, the longitudinal elastic modulus of a pine fiber decreases from roughly 45 GPa for 10° MFA to 10 GPa for 40° MFA [14]. The preferred alignment of cellulose microfibrils in longitudinal direction and the softer matrix, which consists of amorphous wood polymers (hemicellulose and lignin), indicates that the transverse elastic modulus will be lower than the longitudinal. In modeling approaches, it was shown that, in the transverse direction, the MFA of the S2 layer has

little effect on the transverse elastic modulus. It rather seems that the S1 layer and the properties of the matrix, especially of hemicellulose, are more relevant [14]. Here, it must be further considered that the polymers of the amorphous matrix are hygroscopic. Therefore, properties will also depend more strongly on environmental conditions. The hygroscopic influence on the mechanical properties has been studied for pulp fibers [8],[9] and shows a decrease in elastic modulus for the transverse direction. The effect of water on the mechanical properties is even more pronounced. In water, the fiber is swelling and softening, resulting in an elastic modulus that is two orders of magnitude lower.

2.3   Swelling behavior of cellulose materials

Swelling is a reversible physicochemical process, in which liquid or gas molecules (e.g., H_2O) penetrate a material prone to swelling (e.g., cellulose). During the process of swelling, the solid material extends in all dimensions and weight as a result of taking up another material. On a microscopic level, the resulting combined phases become and remain homogeneous, and although the cohesion of the solid is reduced, it is not eliminated [42]. When an aqueous solution in water is separated from pure water by a semipermeable membrane, a driving force causes water to move from the pure water into the solution. This driving force is due to osmotic pressure π. Now, water can be prevented from migration through the membrane into the solution by applying a force *F* on a piston. With *F/A*, where *A* is the cross-section area of the piston, equal to π, the so-called swelling pressure is known [43]. This experimental setup is illustrated in Figure 2.5a and has been often used to characterize different wood species not only in water but also at different relative humidity (RH) [44]–[48]. In Figure 2.5b, a typical swelling pressure curve is illustrated. In the beginning, the swelling pressure increases until a maximum is reached, but then it decreases again. It was found that in water the swelling pressure of wood yields not only lower pressure values, but it is also faster decreasing [49],[50]. At lower swelling rates in moist air rather than in water, the inner wood can contribute more until the outer wood decreases in strength due to the high moisture content [49]. Interestingly, the swelling pressure shows the highest values at low humidity conditions [51]. Furthermore, due to the oriented structure, the swelling pressure is strongly anisotropic. It is in

tangential direction higher than in radial direction of the wood [46]. In cyclic loading, it was shown that the swelling pressure is decreasing from cycle to cycle [52].
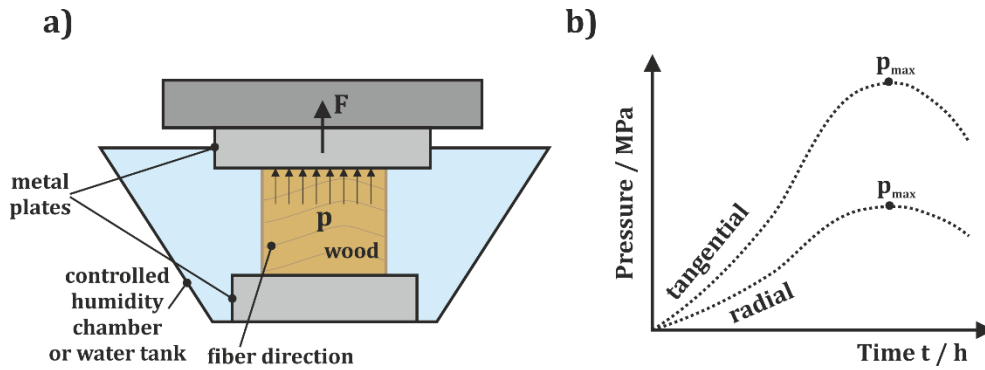

Figure 2.5: (a) Experimental setup to measure the swelling pressure of wood samples in water or at different relative humidity. (b) Scheme illustrating typically measured swelling pressure curves in tangential and radial direction.

Wood can be considered partially dissolved in sorbed water [53]. In general, it should be noted that polysaccharides can form hydrogel-like materials, e.g., cellulose [54],[55], pectin [15], and alginate [56],[57]. A hydrogel is a three-dimensional network of a polymeric material that behaves like a solid due to cross-linking but contains a high amount of water (up to and even beyond 90 % water) because of hydrophilic polymer chains. The high amount of water makes hydrogels behave similarly like biological tissue (~ 70 % water content) and provides – to a certain degree – also mechanical flexibility [58].

It is known that pulp fibers in the wet swollen state form a cellulosic hydrogel-like structure [59],[60]. Comparing wood fibers' properties with those of other hydrophilic solids have proven that many properties of wood fibers are like the typical properties of polymer gels. Changing from dry to wet, the specific surface area of the wood fiber is increasing due to swelling. The amount of swelling depends on the affinity of the solvent for the polymer and can be influenced by variations in temperature and solvent composition. For ionic liquids like salt solutions, the swelling of wood and pulp decreases with increasing ionic strength. This results from the shielding of electrostatic effects. Furthermore, for gels with carboxyl groups, charge content and therefore swelling increases with increasing pH value [59]. Generally, wood pulp fibers contain carboxylic groups which depend on pH, wood species, and the pulping process [59].

12

2.4   Viscoelasticity

The time evolution of mechanical properties of polymers is crucial because – already at room temperature – they can exhibit typical time dependent behavior like creep or stress relaxation. Viscoelastic materials exhibit both, elastic and viscous characteristics when undergoing deformation. In general, viscoelastic materials show three characteristic phenomena: stress relaxation, creep, and hysteresis. In stress relaxation, constant strain results in decreasing stress, while in creep constant stress results in increasing strain. The resulting hysteresis describes a stress-strain phase lag – consequently, the loading and unloading path are not equal – which would not be observed in a purely elastic material [61],[62].

There are different ways to test a viscoelastic material's response [61],[63]. One option is a dynamic approach. Here, stress or strain is varied sinusoidally with time, and the response of strain or stress is measured at different frequencies. The longitudinal viscoelastic properties of hemp fibers have been investigated in this way [64]. Another approach for viscoelastic testing is a transient experiment. While the material is deformed for a chosen time interval, the response is measured. If a constant strain is applied and the stress response is measured, the experiment is called stress relaxation. On the other hand, if the stress is kept constant and the strain is measured, this corresponds to a creep compliance measurement. In this thesis, creep compliance measurements have been carried out, and the viscoelastic analysis has been obtained by solving linear differential equations.

Arbitrary combinations of Hookean elastic springs (denoted elastic moduli E_i) and Newtonian viscous dashpots (denoted viscosities η_i) describing elastic and viscous behavior, respectively [65] (Figure 2.6a, b), are useful to break down a complex behavior of a material.
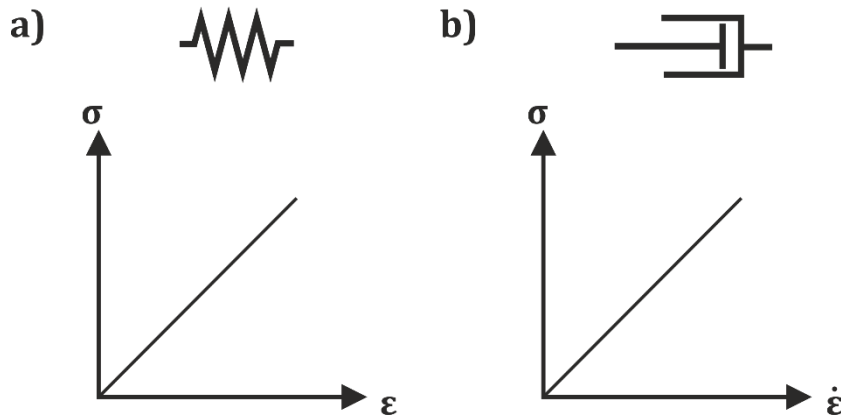
Figure 2.6: (a) A Hookean elastic spring and (b) a Newtonian viscous dashpot are combined to describe the viscoelastic material behavior.

Viscoelastic models with only a spring and a dashpot in series or parallel are too simple to establish a complex material model. In Figure 2.7, the simplest models are illustrated. The Maxwell model is represented by a dashpot and a spring connected in series as depicted in Figure 2.7a. Both elements are subjected to the same stress. The stress decay is predicted exponentially with time, which is accurate for many polymers. For the Maxwell model, it is further possible to define a characteristic time, the so-called relaxation time:

$$\tau = \frac{\eta}{E} \tag{1}$$

which is the ratio between viscosity η and elastic modulus E. In other words, the relaxation time is the time constant τ defining the restoring behavior of a spring-dashpot (Maxwell) element, which relaxes proportionally to $e^{-\frac{t}{\tau}}$. This means that during loading with a constant strain, the stress in a Maxwell element has decayed by factor *1/e* after the time τ has passed. However, the Maxwell model is unable to accurately represent the creep response of solid materials. Most polymers do not exhibit increasing creep over time, more often the strain rate decreases with increasing time [61]. Therefore, the Maxwell model is most useful to model the viscoelastic behavior of fluids but is not appropriate for solids.

Combining the spring and dashpot in parallel results in the so-called Kelvin-Voigt model, which is presented in Figure 2.7b. Here, both elements are subject to the same strain. While the Kelvin-Voigt model is extremely accurate in modeling creep for many materials, the model has limitations in its ability to describe the commonly observed relaxation of

14

stress in numerous strained viscoelastic materials. It has been established as a well-working model for soils [66].
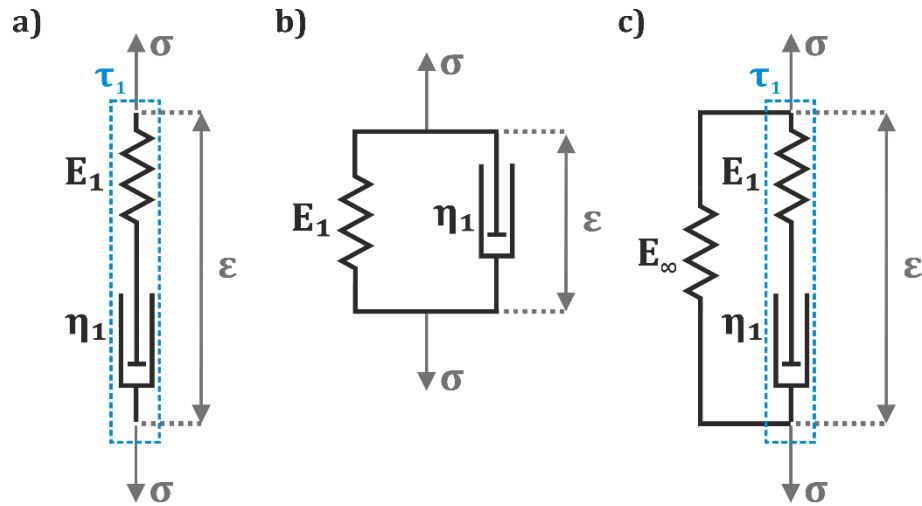

Figure 2.7: Simple viscoelastic models. (a) The Maxwell model consists of a spring E_1 and a dashpot η_1 in series. With the ratio of the two elements, a relaxation time τ_1 can be defined. (b) indicates the Kelvin-Voigt model where a spring and a dashpot are parallel to each other. (c) The Standard Linear Solid (SLS) model consists of a Maxwell model with a relaxation time τ_1 that is parallel to a spring.

The Standard Linear Solid (SLS) model combines a Maxwell model and a spring in parallel as depicted in Figure 2.7c. For many materials of interest, it has proven to predict both, creep and relaxation responses accurately. In this work, it was applied to well-known polymers, such as poly(methyl methacrylate) (PMMA) and polycarbonate (PC) [67]. It is important to use a model that describes the data well, but one has to avoid introducing too many parameters which are difficult to interpret and make parameter fitting hard. In this work, the Generalized Maxwell model of order two (GM2) and order three (GM3) proved to be appropriate for cellulosic fibers [68] and are presented in Figure *2.8*. The GM2 model (Figure 2.8a) consists of three springs (E_∞, E_1, E_2) and two dashpots (η_1, η_2), whereas the GM3 model (Figure 2.8b) contains an additional branch with E_3 and η_3. E_∞ corresponds to a purely elastic response. The combination of spring and dashpot in series (E_i and η_i) are so-called Maxwell elements, as described earlier, and for each of these elements, it is possible to define a relaxation time τ_i.
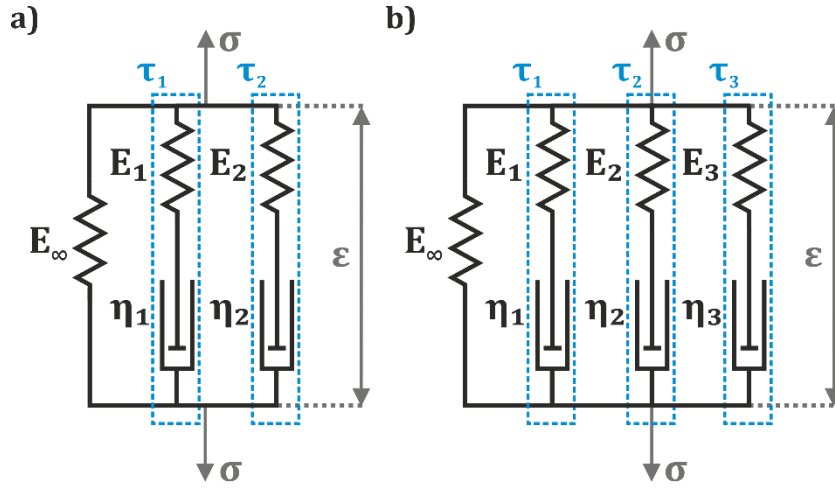
Figure 2.8: Generalized Maxwell model of (a) order two (GM2) and (b) order three (GM3).

The SLS, GM2, and GM3 models provide an upper and lower limit for the material's elastic modulus. If the loading is infinitely slow, the strain rate $\dot{\varepsilon} \rightarrow 0$. This means that only the infinite modulus E_∞ remains and all E_i are zero. At infinitely fast loading, the dashpots become rigid, and only the springs deform leading to an instantaneous elastic modulus $E_0 = E_\infty + \sum E_i$.

For the SLS model, the corresponding constitutive equation is

$$\sigma = A\varepsilon + B\dot{\varepsilon} - C\dot{\sigma}, \tag{2}$$

with the coefficients $A = E_\infty$, $B = \left(\frac{E_1 \tau_1}{E_\infty} + \tau_1\right) E_\infty$, $C = \tau_1$ [67].

The corresponding constitutive equation for the GM2 model is

$$\sigma = A\varepsilon + B\dot{\varepsilon} + C\ddot{\varepsilon} - D\dot{\sigma} - E\ddot{\sigma}, \tag{3}$$

with the coefficients $A = E_\infty$, $B = \left(\frac{E_1 \tau_1 + E_2 \tau_2}{E_\infty} + \tau_1 + \tau_2\right) E_\infty$, $C = \tau_1\tau_2 (E_\infty + E_1 + E_2)$, $D = \tau_1 + \tau_2$, and $E = \tau_1\tau_2$ [67],[68].

Finally, for the GM3 model (Eq. 17), the constitutive equation is due to its complexity and length summarized in Appendix A.

2.5   Contact mechanics

For AFM-based force experiments, a contact mechanics model is required to relate the force and the indentation depth measured in the experiment to stress and strain in the viscoelastic model. In Figure 2.9, the contact between tip and sample (a) before and (b) during deformation is illustrated. Usually, the value for the tip radius R is known and the indentation depth δ can be determined from experimental data. The contact radius a is defined by the contact zone between sample and tip [69]. The simplest and most commonly used model is based on the Hertz theory [70], which allows calculating the contact shape and forces under the influence of an external force but does not include surface forces like adhesion. In Table 2, the corresponding Hertz equations to calculate the stress and strain for a spherical indenter are presented. Also illustrated in Table 2, are the equations of the Johnson-Kendall-Roberts (JKR) model, which is an extension of Hertz theory [71]. This model takes adhesive interactions and their influence on the contact shape into account. JKR applies especially to the contact of a large radius probe with a soft sample surface [72]–[74]. In the JKR model, only adhesive interaction within the contact zone is assumed and interactions outside the contact zone are neglected [69]. In Figure 2.9b, the JKR contact is visualized and as can be seen in the small inset, adhesion F_{ad} results in neck formation at the rim of the contact zone. In Hertz theory, this is not the case. Comparing both models in Table 2, it is clear to see that due to the consideration of adhesion, the equations for stress and strain of the JKR model are more complex. With $F_{ad} = 0$, the JKR equations would be equal to the Hertz equations. F_{ad} can be easily determined from experimental AFM data, which will be explained later.
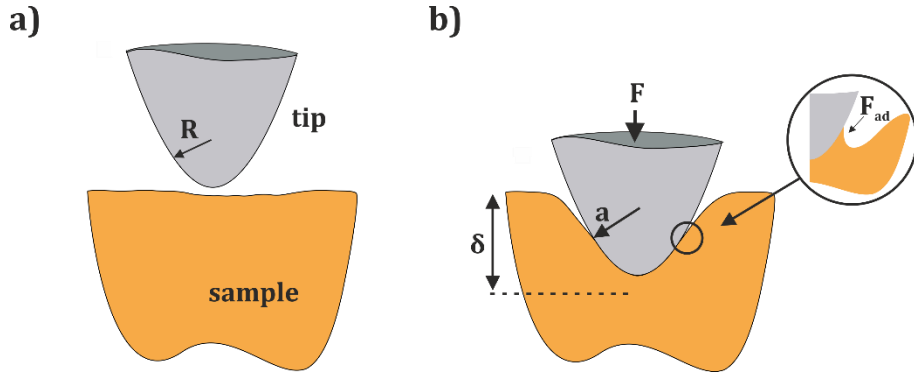
Figure 2.9: Illustration of the JKR contact between a hemispherical tip with a sample surface. (a) shows the tip, which is characterized by the tip radius R, before contact. In (b), a force is applied, and the tip is penetrating the sample surface to an indentation depth δ. The contact radius a indicates the contact zone between tip and sample surface. In the inset, the neck formation at the rim of the contact zone due to the consideration of adhesion (F_{ad}) is illustrated.

In the formulas for the JKR model in Table 2, the definition of the loading force $\tilde{F}$ which accounts for adhesive effects is

$$\tilde{F}(t) = F(t) + 2\,F_{ad} + 2(F_{ad}F(t) +\ F_{ad}{}^2)^{1/2}, \tag{4}$$

where $F(t)$ is the force applied during the experiment and F_{ad} is the adhesion force with

$$F_{ad} = \frac{3}{2}\pi R_{eff}W, \tag{5}$$

where W is the work of adhesion per unit area and R_{eff} is the effective radius of the contact between tip and surface.

Table 2: Overview of the basic equations of important contact mechanics models. These equations relate force F and indentation depth δ to stress σ and strain ε. The Hertz theory is the basic and simplest model, whereas the JKR model is used when adhesive interactions of indenters having large radii with soft materials need to be considered.

	contact radius a	indentation depth δ	stress σ	strain ε
Hertz	$a^3 = \dfrac{3}{4}\dfrac{R}{E}F$	$\delta = \dfrac{a^2}{R}$	$\sigma = \dfrac{3}{8}\dfrac{F}{R\delta}$	$\varepsilon = \dfrac{1}{2}\left(\dfrac{\delta}{R}\right)^{\frac{1}{2}}$
Sneddon	$a^3 = \dfrac{3}{8}\dfrac{R}{E}F$	$\delta = \dfrac{a^2}{R}$	$\sigma = \dfrac{3}{8}\dfrac{F}{R\delta}$	$\varepsilon = \left(\dfrac{\delta}{R}\right)^{\frac{1}{2}}$
JKR	$a^3 = \dfrac{3}{4}\dfrac{R}{E}\tilde{F}$	$\delta = \dfrac{a^2}{R} - \left(\dfrac{4a}{3R}\dfrac{F_{ad}}{E}\right)^{\frac{1}{2}}$	$\sigma = \dfrac{3\tilde{F}}{8R\delta}\left[1 - \dfrac{4}{3}\left(\dfrac{F_{ad}}{\tilde{F}}\right)^{\frac{1}{2}}\right]^2$	$\varepsilon = \dfrac{1}{2}\left(\dfrac{\delta}{R}\right)^{\frac{1}{2}}\left[1 - \dfrac{4}{3}\left(\dfrac{F_{ad}}{\tilde{F}}\right)^{\frac{1}{2}}\right]^{\frac{1}{2}}$

2.6 Nanoindentation

Nanoindentation (NI) is a technique to determine a material's mechanical properties on the nanometer scale. An indenter with a defined shape and known elastic properties (elastic modulus E_i and Poisson's ratio ν_i) is pressed into a material's surface. During this process, the applied force F and the resulting deformation – which is measured by the indentation depth z_i – is recorded constantly.

The Oliver-Pharr method [75] is used to determine the material parameters from the experimental force-indentation depth curves, which are the reduced modulus E_r and hardness H. A typical loading-unloading curve with significant plastic deformation is presented in Figure 2.10. In plastic force-indentation depth curves, the sample does not follow the same path during retraction and the distance at zero force does not correspond to the same probe-sample distance at the beginning. In the force-indentation depth plot, the area between the loading and unloading curve corresponds to the energy dissipated by the plastic deformation. Indentation hardness H can be determined as [75]

$$H = \frac{F_{max}}{A(z_c)},\qquad(6)$$

where F_{max} is the maximum force and $A(z_c)$ is the indenter's projected area at contact indentation depth z_c. The projected area at contact depth $A(z_c)$ is usually determined by evaluating the indenter's area function $A(z)$ at $z = z_c$. $A(z)$ is only dependent on the indenter's geometry and can be obtained by calibrating the indenter on a material with known mechanical properties [75] which is the conventional method for NI or by imaging the indenter with SEM or AFM [8],[76]. A more detailed discussion can be found in [9].

The contact depth z_c can be determined by the relation

$$z_c = z_{max} - \epsilon\frac{F_{max}}{S},\qquad(7)$$

where z_{max} is the maximum indentation depth, S is the slope of the unloading curve and ϵ depends on the probe shape (e.g., 0.75 for a pyramidal indenter).

The reduced elastic modulus E_r can then be determined as

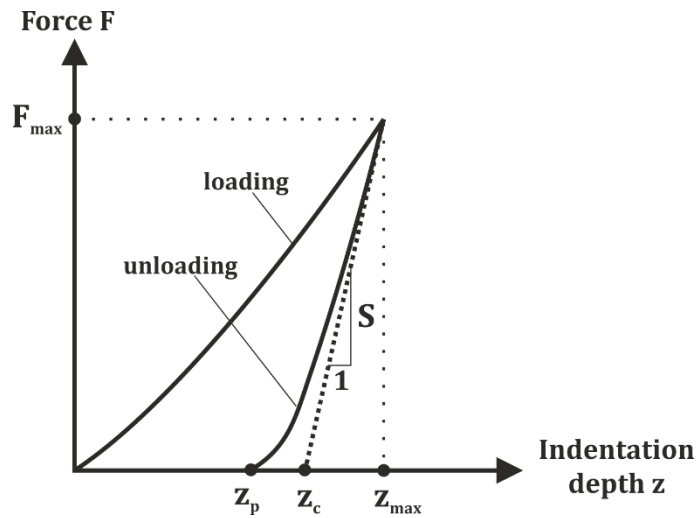$$E_r = \frac{\sqrt{\pi}}{2}\frac{S}{\sqrt{A(z_c)}}.\qquad(8)$$

Figure 2.10: The force-indentation depth (F-z) curve in nanoindentation. The slope S of the unloading curve is used to analyze the material parameters. At the maximum force F_{max}, the maximum indentation depth z_{max} is achieved. The intersection of the slope line with the abscissa indicates the contact indentation depth z_c, while the endpoint of the unloading curve on the abscissa is a measure for the permanent, plastic deformation z_p.

2.7 Atomic force microscopy (AFM)

Atomic force microscopy (AFM) [77] is an experimental technique applying low forces in the pN – µN range and is also well suited for nanomechanical characterization of soft polymer and biological surfaces. The AFM technique is based on scanning a sharp tip – attached to the end of a cantilever – across a surface to record its topography. In Figure *2.11*, the operation principle of AFM is presented. In many commercial systems, the cantilever is mounted with an angle of about 11° in a holder that can move only in z-direction and the sample is scanned in x- and y-directions. These movements in x-, y-, and z-direction are achieved by employing piezo actuators, which provide sub-nm position accuracy. A scan is performed by moving the cantilever back and forth along a line in its longitudinal direction, which is the fast scanning x-axis, and then incrementally increasing in y-direction. The AFM can detect forces between probe and sample in the pN to µN range, covering both, the short-range repulsive and long-range attractive interactions. Of course, the AFM system needs to be sensitive enough to read out these forces. This is most frequently achieved with an optical lever technique. Here, the deflection of the cantilever due to the interaction with the sample surface is detected by a laser beam which is

20

reflected from the cantilever's backside to a position-sensitive detector. In most commercial instruments, the detector is a split photodiode as is illustrated in Figure 2.11 and more closely in Figure 2.12.
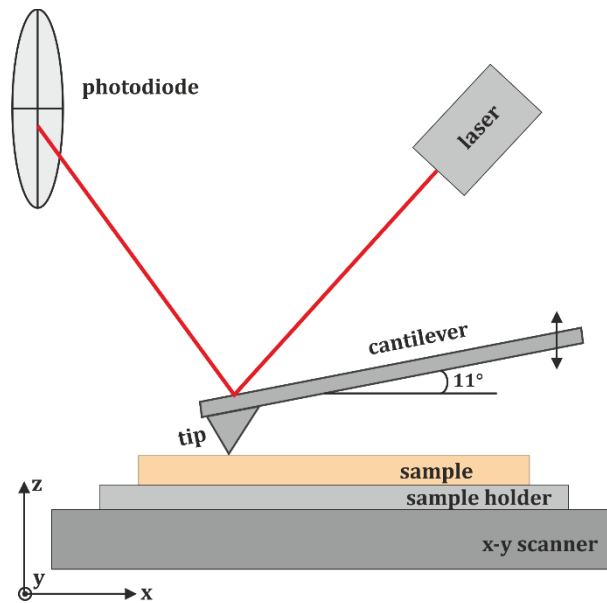

Figure 2.11: Typical AFM setup. The deflection of the cantilever is detected by an optical lever technique and the sample is mounted on an x-y scanner. The cantilever is mounted with an angle of about ~11°.

Here, the detection of the cantilever's deflection in z-direction is achieved by, e. g., subtracting the light intensity recorded at the photodiode's lower half from the one of the upper quarter (Figure 2.12a). Additionally, the intensity difference between the right and left quarters can be analyzed and this way, the cantilever's torsion can be detected, which is essential for friction force measurements (Figure 2.12b).
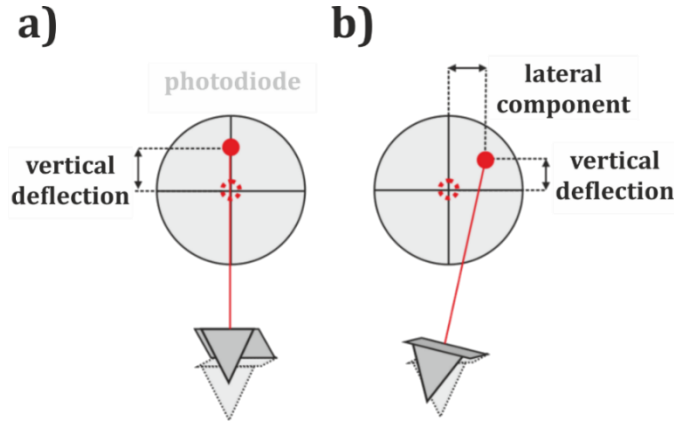
Figure 2.12: Split photodiode. In (a) the movement of the laser beam on the photodiode due to a vertical deflection is illustrated. In (b) an additional lateral movement of the cantilever is indicated.

For small deflections z, the force F that leads to the bending of the cantilever can be calculated by the linear relation

$$F = k\,z\,,\tag{9}$$

where k is the spring constant or stiffness of the cantilever. In the optical lever force detection technique, force sensitivity is depending on the cantilever stiffness. The spring constant k depends only on the cantilever's geometry (width w, length l, and thickness d) and Young's modulus E. For a rectangular, uniform cross-section of the cantilever, the spring constant is

$$k = \frac{Ewd^3}{12l^3}\,.\tag{10}$$

In the simplest measurement procedure called static or contact mode, a feedback loop is used to keep the deflection at a constant value by moving it in z-direction. By scanning the sample in x- and y-directions, the sample's surface topography is recorded as z(x, y). A force in contact measurements is in the range of a few nN but even at the smallest forces possible, tip wear and sample deformations, especially on soft and biological samples, can occur. To prevent this, dynamic measurements can be employed where the acting forces are smaller, and interactions can be solely attractive. Depending on the instrumentation and feedback technique used, two different families of dynamic modes are existing: amplitude modulated AFM (AM-AFM) and frequency modulated AFM (FM-AFM) [72]. FM-AFM is most often used under ultra-high vacuum (UHV) conditions. With dual feedback, the tip-sample distance, as well as the immediate resonance frequency of the cantilever, are preserved. The tip is oscillating above the surface without touching it, therefore

operating in so-called non-contact mode. AM-AFM is mainly used in air and monitors the amplitude and phase shift of the resonance curve of the cantilever during the surface approach. Here, the cantilever is excited slightly below or above its resonance frequency near the surface with the tip apex periodically touching the sample surface. This mode is called tapping mode or intermittent contact mode and can operate in both regimes of long-range attractive and short-range repulsive forces. It is the preferred mode for the investigation of soft and biological materials and can also be performed in liquid [78]. During tapping, the interaction with the surface will dampen the oscillation amplitude A to a value below its free amplitude A_{free}. To keep A at a constant value A_{sp} (setpoint), the feedback loop controls the movement in z and this way the topography z(x,y) is obtained. The ratio of free amplitude and setpoint gives a measure of the applied force. In tapping mode, it is also possible to obtain qualitative information on the mechanical properties of the material's surface [79]–[81]. The phase shift between the exciting oscillation and the cantilever's actual oscillation results from energy dissipation due to the contact with the surface [82]. The recording of the phase shift results in a so-called phase image.

In AFM force measurements, the tip-sample interaction is used for information on local sample properties. If plots of normal force vs. distance between probe and sample are obtained, so-called force-distance (F-d) curves, it is partly possible to distinguish between different force components.
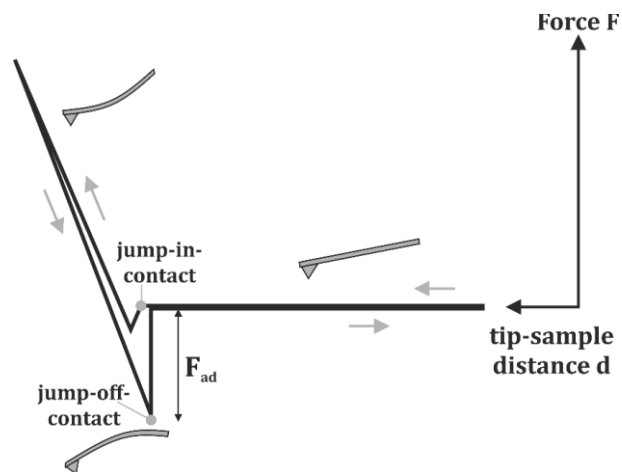

Figure 2.13: Principal of F-d curves under ambient conditions. First, the tip and the sample surface are too far apart to interact. The cantilever is not deflecting. Attractive forces increase the closer the tip gets to the surface and at the point where the surface forces are higher than the cantilever stiffness, the tip jumps into contact (jump-in-contact). During retraction, a higher negative force, which is equal to the adhesion, is needed to separate the tip and the sample surface again at the jump-off-contact point.

The force has a highly nonlinear dependency on the tip-sample distance which is usually defined as the distance of the closest points between probe and sample. A typical F-d curve under ambient conditions is presented in Figure 2.13 and can be divided into different characteristic regions. During the approach, the tip is far away from the surface and there is no interaction, therefore, no deflection of the cantilever. Getting closer to the surface, the attractive forces increase and at one point, the attractive forces become higher than the spring constant of the cantilever and the probe jumps into contact with the surface. This is the jump-in-contact point. Once in contact, also repulsive forces are detected. Depending on the stiffness of the cantilever and on the mechanical properties of the sample, further force application might lead to small elastic deformations of the sample surface. During retraction, the curve should first look the same as the approach curve under the assumption that there is no plastic deformation of probe or sample. Once the point of the jump-in-contact is reached, the curves start to differ. Here, the probe is now still in contact and a point – where the cantilever spring force is higher than the attractive force – called jump-off-contact point is only reached with a negative force. This negative force is the total attractive force in contact and is referred to as adhesion force F_{ad}. At ambient conditions, surfaces are usually covered with a thin water layer. Therefore, a capillary neck between the tip and the sample surface is formed once these surfaces are close together. These capillary forces cause a strong adhesion at retraction. In water, the adhesion forces are reduced because this effect is eliminated. Once the tip is separated from the sample surface, the cantilever follows the same path as it did during the approach [69],[72],[83].

2.7.1 AFM-based nanoindentation (AFM-NI)

Besides testing in an elastic regime, also plastic behavior of soft materials can be probed, namely by adapting the nanoindentation (NI) technique to AFM. Compared to conventional NI as described in Chapter 2.6, in AFM-NI the force applied is not purely vertical due to the 11° tilt of the AFM probe in commercial systems. Therefore, a lateral movement of the tip cannot be avoided but can be reduced by stiffer cantilevers or lower applied load. As in NI, the Oliver-Pharr method [75] is used to determine the material

parameters from plastic deformation, which are hardness H (Equation 6) and the reduced modulus E_r (Equation 8).

The area function $A(z)$ of an indenter describes the projected area at a certain distance z from the tip apex and is an essential input parameter for calculating E_r and H correctly. Whereas in conventional NI this function is usually calibrated by indenting into a material with varying indentation depths, in AFM-NI, the direct imaging of the indenter's geometry can be achieved by scanning the AFM tip across a grid with sharp spikes – a so-called tip characterizer. As long as the opening angle of the spikes is less than the indenter's opening angle, the indenter is imaged. This is commonly known as tip-sample dilation [84] and this way, the area function can be determined [85].

2.7.2 Hygroscopic AFM experiments

In AFM, the bending of the cantilever can be measured by the optical lever method with extremely high accuracy. Sensors utilizing this principle are in the focus of recent research [86]. Cantilever arrays are used to differentiate a spectrum of molecules, creating an artificial "chemical nose", leading to sensor systems which can detect diabetes in the human breath [87] or cancer [88],[89]. By reading out the deflection of the cantilever [90], molecules adsorbing on the cantilever surface can be detected. Usually, the measured deflection is very small. Therefore, bilayer structures, with one of the layers having a large surface area, are used to obtain larger deflections. Inspired by plants, humidity-induced bending of bilayer structures is frequently used for actuation purposes. Two layers undergo different deformation upon changes in RH or hydration, which leads to a bending movement [91]. Examples are the opening of tree cones [92] or the movement of the dispersal units of wild wheat [93]. Also, a mesoporous silica/nonporous silicon bilayer using a commercial AFM cantilever as a substrate has potential as actuation sensor [94],[95]. Here, it was shown that the humidity-induced deformation of mesoporous silica creates a strain in the porous film, which leads to a reversible cantilever deflection of roughly 140 nm. The bilayer principle has been also used for simple artificial actuators based on the swelling of paper–plastic bilayers [96]. Unpublished results also indicate that a cellulose thin film formed on a conventional AFM cantilever induces a deflection at changing RH due to the swelling of the film. The principle is illustrated in Figure 2.14.
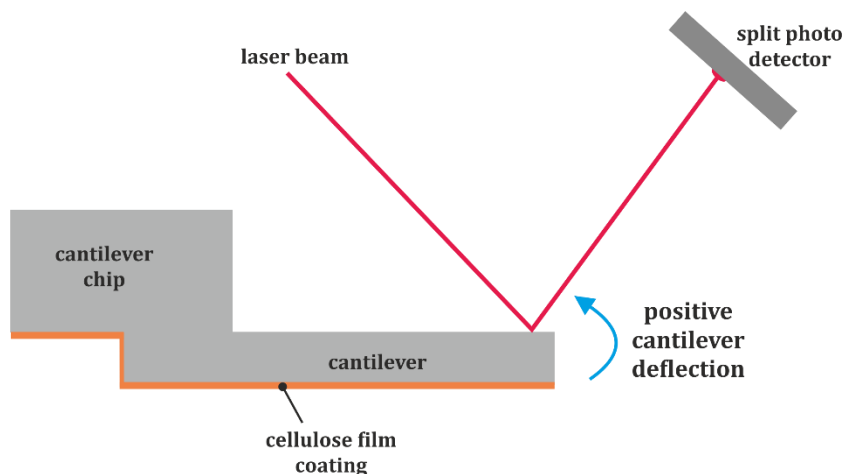
Figure 2.14: Principle of the cantilever bending experiment with a thin cellulose film coating on the lower side of the cantilever. A positive cantilever deflection corresponds to a swelling of the cellulose film.

2.7.3 Friction Force Microscopy (FFM)

On the nanoscale, friction behavior of polymers can be studied by friction force microscopy (FFM) or lateral force microscopy (LFM) [97]. FFM is a contact mode technique that measures variations in frictional forces across a sample surface. In these measurements, the fast scan direction is perpendicular to the cantilever's long axis. FFM measurements are quite straightforward since the position-sensitive detector is also sensitive to lateral movements of the laser beam deflected from the cantilever (see Figure *2.12*). The cantilever torsion due to lateral forces (parallel to the surface) acting on the tip is measured and related to the friction coefficient. This is illustrated in Figure 2.15. Friction was one of the first quantities other than dimensions studied by AFM on graphite or mica surfaces [98],[99]. For phase-separated thin organic films [100],[101], differences in the friction signal between hydrocarbon and fluorocarbon containing domains were found by FFM. Also, the friction behavior of different polymer blend films can be studied [97]–[99]. More recently, FFM was employed to characterize photoreactive organic surface patterns of spin casted thin films [102],[103] and to correlate friction to viscoelastic relaxation [104],[105].
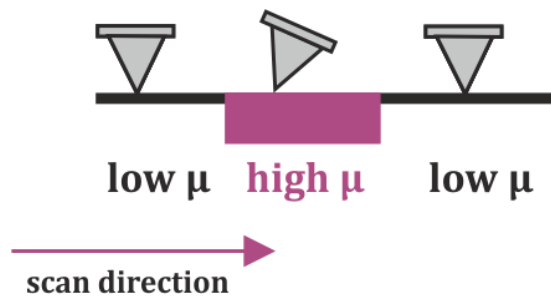
26

Figure 2.15: Principle of FFM. Variations in friction forces across a sample surface result in cantilever torsion due to lateral forces.

3 Experimental

3.1 Samples and sample preparation

3.1.1 Polymer samples

For the validation of the viscoelastic method well-known polymer samples – poly(methylmethacrylate) (PMMA) (Plexiglas 7N, Evonik Industries AG) and polycarbonate (PC) (Makrolon 2405, Covestro AG) – have been investigated. ISO 3167 multi-purpose specimens were manufactured by injection molding. The specimens featured a gauge length of 80 mm and width and thickness of 10 mm and 4 mm, respectively. After the performance of the tensile tests, pieces with a length of about 20 mm were cut out for AFM and NI measurements.

3.1.2 Pulp fibers

Single fibers

The investigated pulp fibers were industrial unbleached (kappa number κ = 42), unrefined, once dried kraft pulp fibers (Mondi Frantschach, Austria). This pulp is a mixture of spruce and pine fibers with a diameter between 20 µm – 30 µm and a length of 3 mm to 5 mm. These fibers were all in the collapsed state. With optical microscopy, the pulp fibers were analyzed to determine the wood species [25]. Representative optical micrographs for spruce and pulp fibers are presented in Figure 3.1. In Figure 3.1a, it can be distinguished that spruce fibers are characterized by oval to round pits, whereas, for pine fibers window-like, rectangular pits as presented in Figure 3.1b are typical [25]. Measurements in transverse direction in this work have been performed on four spruce and two pine fibers. From the shape and size of the pits, it is more likely that earlywood fibers have been investigated.
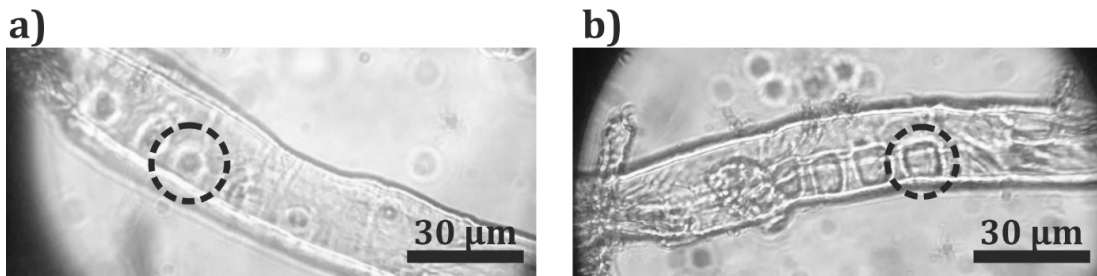
Figure 3.1: Optical micrographs of industrial kraft pulp fibers. (a) Spruce pulp fiber, the dashed circle indicates a spherical pit on the fiber surface which is characteristic for spruce fibers. (b) Pine pulp fiber, the dashed circle indicates a rectangular-shaped pit which is a common feature of pine fibers.

For AFM-NI and viscoelastic measurements under controlled humidity and in water, pulp fibers have been placed on top of a drop of nail polish to ensure that the fibers cannot move vertically during indentation. Ideally, the fiber is fully embedded in the nail polish with only the surface uncovered and accessible to the AFM probe. This is schematically illustrated in Figure 3.2 and has been successfully applied before [9],[106],[107]. The nail polish was left to cure at room temperature for at least 12 h. For measurements in water, the fibers were stored in water for at least 24 h to ensure complete swelling.
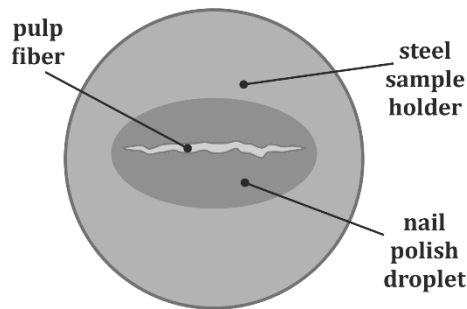
Figure 3.2: Schematic illustration of the preparation of the pulp fibers for the AFM measurements on the circular sample holder.

Microtome cuts for the S2 layer

Microtome cuts of the same industrial, unbleached and unrefined pulp have been carried out by Angela Wolfbauer (Graz University of Technology, Institute for Bioproducts and Paper Technology). As presented in Figure 3.3, paper is embedded in a hydrogel-like material called glycol methacrylate (GMA), and afterward cut by a diamond knife to a slice

thickness of about 7 μm [108],[109]. The dash-lined ellipses in Figure 3.3 indicate fibers which have been cut more along the long fiber axis. On the other hand, dashed circles in Figure 3.3 indicate fibers which have been cut almost perpendicular to the longitudinal fiber axis. These 7 μm thick microtome cut slices of paper have also been prepared for AFM measurements by embedding them in nail polish.
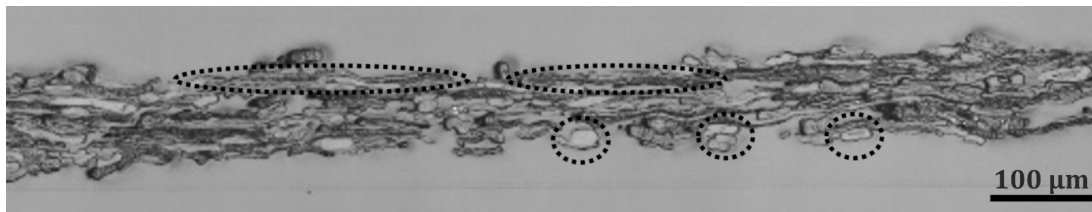

Figure 3.3: Microtome cut slice of a small paper sheet. The fibers are cut in arbitrary directions and are embedded in glycol methacrylate. The dashed ellipses indicate fibers that have been cut more along the long fiber axis whereas the dashed circles mark fibers which have been cut more perpendicular to the long fiber axis. The slice is about 7 μm thick.

3.1.3 Viscose fibers

Viscose fibers with a rectangular cross-section, 200 μm wide and 5 μm thick, have been investigated. All fibers had been already cut to a length of 4 mm by the supplier, Kelheim Fibres GmbH (Kelheim, Germany). The fiber surface is smooth with trenches along the longitudinal direction as can be seen in the optical micrograph in Figure 3.4. For AFM-NI and viscoelastic investigations under controlled humidity and in water, viscose fiber samples were prepared in the same way as the pulp fiber samples, i. e., by embedding in nail polish.
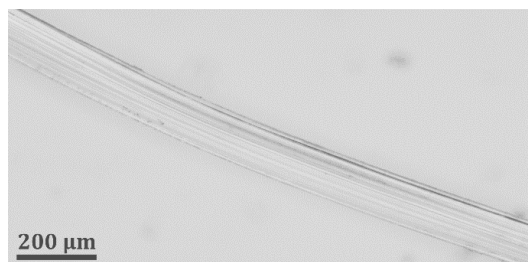

Figure 3.4: Optical micrograph of a viscose fiber with a rectangular cross-section.

3.1.4 Amorphous cellulose films

Cellulose thin film deposition on tipless AFM cantilevers

Thin cellulose films were used as model systems to simulate pure cellulose surfaces for cantilever bending. The films were deposited onto tipless AFM cantilevers in two different ways. The simplest approach was manually depositing a droplet of a TMSC and toluene solution onto the cantilever frontside. The solution has been prepared at Graz University of Technology. Afterward, the whole cantilever with the TMSC film was exposed to a few ml of 10 wt% hydrochloric acid (HCl) solution for 10 min to regenerate TMSC to cellulose. A typical optical micrograph of such a cantilever covered by a cellulose film is presented in Figure 3.5. This deposition method is very simple and fast. However, since the deposition is done manually, it is very common that also the backside of the cantilever gets covered by the TMSC solution which is not ideal. Another disadvantage is that it is difficult to obtain a homogeneous film thickness. Only one out of four cantilevers is suitable for further experiments.
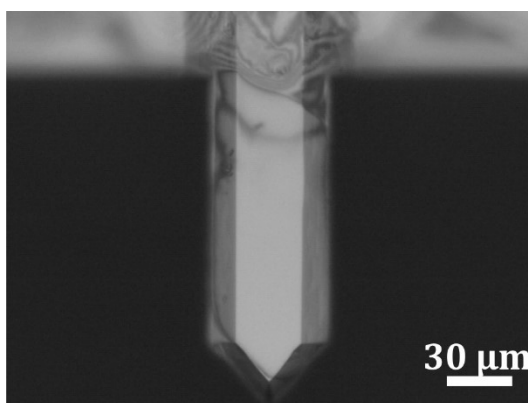

Figure 3.5: Optical micrography of the front side of a tipless AFM cantilever covered with a cellulose thin film of about 100 nm. The length of the cantilever is about 100 μm, the thickness about 3.5 μm and the width approximately 30 μm.

In a second approach, a polydimethylsiloxane (PDMS) based transfer procedure was adapted from [110] and performed by Aleksandar Matković. The stages of the transfer procedure are visualized in Figure 3.6. First, thin TMSC films were produced by spin coating a solution of TMSC and chloroform onto a silicon wafer. The solution has been prepared at Graz University of Technology. After spin coating, part of the TMSC thin film

is mechanically removed by cutting and scratching, leaving the SiO_2 surface exposed. This is presented in Figure 3.6a. Only a few rectangular TMSC pieces which are about 30 μm wide are left purposefully on the surface and picked up by a thin PDMS sheet (Figure 3.6b). Next, the PDMS with the picked-up pieces is aligned above the center of the cantilever ending (Figure 3.6c) and then lowered down to the cantilever. The PDMS sheet is heated and slowly pulled away from the surface, leaving the piece of TMSC film behind (Figure *3.6*d). Afterward, the TMSC film covered cantilever is exposed to a few ml of 10 wt% HCl solution for 10 min to transform TMSC into cellulose. In the optical micrograph in Figure 3.7, the difference between the TMSC film and the cellulose film is visible. The TMSC film (Figure 3.7a) is about 50-100 nm in thickness, whereas the cellulose film in Figure 3.7b shrinks to a thickness below 50 nm, which is typical in the regeneration process [34]. Due to the regeneration process, the cellulose covalently bonds to the silicon oxide surface.
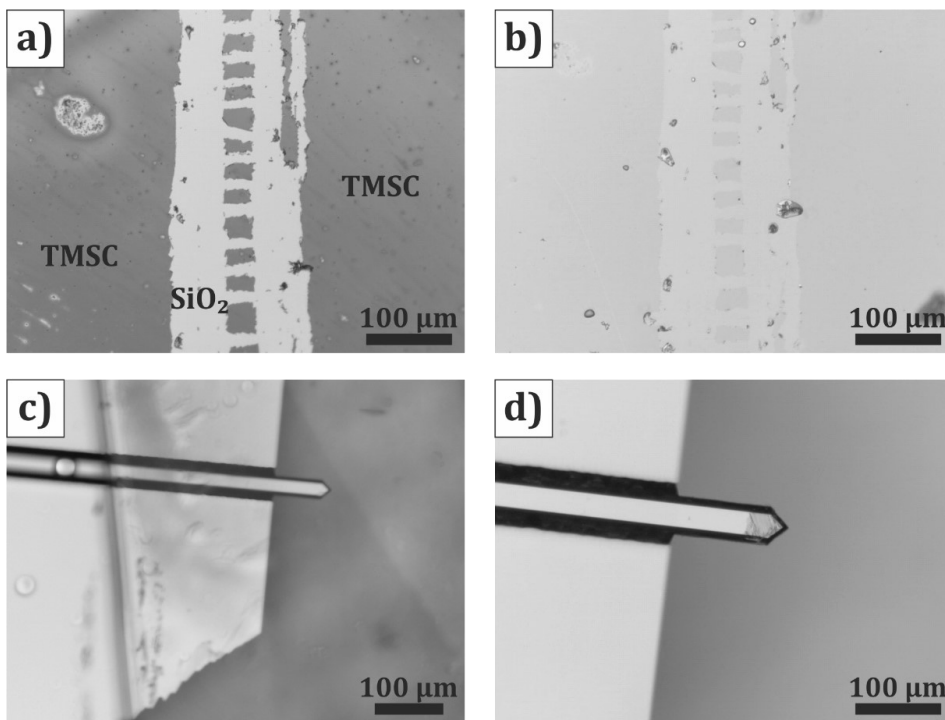

Figure 3.6: Stages of the PDMS based transfer procedure for the TMSC film onto the tipless AFM cantilever. (a) TMSC film with cut clear rectangular-shaped pieces of TMSC. (b) The same area as in (a), now covered with PDMS. (c) PDMS with picked-up TMSC pieces (not visible) above the cantilever for alignment. (d) Successful transfer of a TMSC piece onto the cantilever.
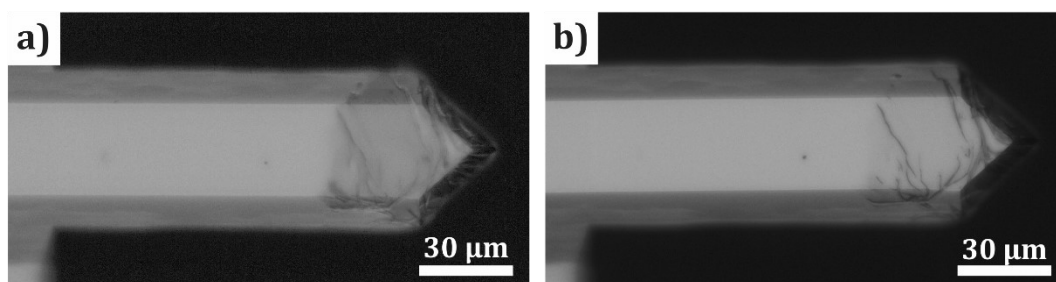
Figure 3.7: (a) TMSC film covered cantilever with a film thickness of about 50 – 100 nm. (b) Cellulose film covered cantilever with a film thickness of less than 50 nm.

Cellulose blend films

Cellulose blend films consisting of different compositions of hydroxypropyl cellulose stearate (HPCE) and TMSC have been prepared at Graz University of Technology. After a cleaning procedure of the silicon substrates, TMSC and HPCE were dissolved in a chloroform concentration of 0.75 wt%. Afterwards, the solutions were filtered through 0.45 µm PVDF filters (Chromafil) and mixed in volumetric ratios TMSC:HPCE 1:0, 1:3, 1:1; 3:1, and 0:1. A volume of 100 µl was used for spin coating and spun for 60 s with an acceleration of 2500 rpm/s and a speed of 4000 rpm. For the conversion of TMSC to cellulose, the substrates have been exposed to 3 ml of 10 wt% HCl vapor in a petri dish. More details on the film preparation can be found in [41].

3.2 Atomic Force Microscopy (AFM)

All measurements in this work were acquired using an MFP-3D stand-alone AFM (Asylum Research, USA). The instrument is equipped with a closed-loop planar x-y-scanner with a scanning range of 85×85 µm² and a z-range of 15 µm.

3.2.1 AFM probes

Imaging

For imaging, AC160TS-R3 silicon probes (Olympus, Japan) with an aluminum reflex coating at the backside of the cantilever were used. These probes have a tetrahedral tip at

the very end of the cantilever with a front angle of 0°, a back angle of 35°, and side angles of 15°. The tip apex radius is typically 7 nm with an average resonance frequency of 300 kHz and an average spring constant of 26 N/m.

AFM-NI

For AFM-NI, so-called ND-DYIRS probes (Advanced Diamond Technologies, USA) were used. These probes are full-diamond probes with aluminum reflecting backside coating and have a regular, four-sided pyramid as a tip. The front, back, and side angles are all 45° and the apex radius is less than 50 nm. The spring constant has been determined to be (81 ± 16) N/m using the thermal sweep method [111]. The thermal Q is 618 ± 48 and the resonance frequency is (369 ± 22) kHz (values are given as mean ± standard deviation calculated from 6 independent measurements). These probes have already been used in [9] and were thoroughly discussed there.

Viscoelastic AFM-NI

For the viscoelastic measurements, LRCH250 silicon probes (Team Nanotec, Germany) have been used. The spring constant of the cantilever in use is (279 ± 52) N/m and has been calibrated by performing the thermal sweep method (values are given as mean ± standard deviation calculated from 17 independent measurements). The thermal Q factor is 716 ± 210 and the resonance frequency is (575 ± 1) kHz. For measurements in water, the calibration of the LRCH250 probes was difficult due to their high stiffness. Therefore, a softer LRCH40 (Team Nanotec, Germany) probe was chosen instead. Again, the calibration of the spring constant was performed after [32]. The spring constant of this cantilever is (70.8 ± 1.2) N/m, the thermal Q is 10.4 ± 0.08 and the resonance frequency is (209 ± 0.5) kHz (values are given as mean ± standard deviation calculated from 6 independent measurements). For the evaluation procedure of the experiments, it was important to determine the tip radius of each probe. Therefore, a commercially available TGT01 calibration grid (NT-MDT, Moscow, Russia) was employed. On this grid, spikes with an opening angle of 30° and a tip radius of 10 nm are arranged periodically. Utilizing the tip-sample dilation principle [84], it is possible to image the AFM tip by scanning across this grid, as presented in Figure 3.8 and by fitting paraboloids to the scan of a single spike (as shown in Figure 3.8b), the tip radius can be obtained. For the hemispherical

34

LRCH250 and the LRCH40 probes, the tip radii were found to be (307 ± 21) nm and 345 nm, respectively.
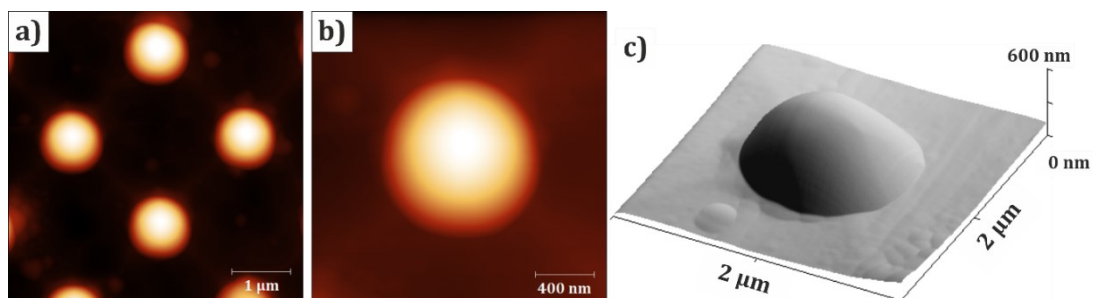

Figure 3.8: (a) 5 x 5 µm² and (b) 2 x 2 µm² topography image of the AFM tip using the calibration grid (z-scale: 600 nm). In (c), a three-dimensional view of (b) is presented.

Cantilever bending experiment

For bending experiments, tipless NSG30 cantilevers (NT-MDT, Russia) with a nominal spring constant of 30 N/m and a resonance frequency of about 300 kHz have been employed. The spring constant has been determined to be 27.8 N/m by the thermal sweep method. The thermal Q is 780 and the resonance frequency is 67 kHz from one measurement. The backside is coated with gold (Au) whilst the frontside was covered by the cellulose film, as described in subsection 3.1.4.

Friction Force Microscopy experiments

For FFM, CSG10/Au probes (NT-MDT, Russia) with a tip radius of about 30 nm and a cantilever spring constant of 0.1 N/m were employed. The probes are made of silicon and covered with a thin gold layer. The spring constant has been determined to be 0.1 N/m by the thermal sweep method. The thermal Q is 10.4 ± 0.08 and the resonance frequency is (209 ± 0.5) kHz (values are given as mean ± standard deviation calculated from 6 independent measurements). AFM force spectroscopy measurements to investigate the adhesion properties of the film surfaces were performed with HSC60 probes (Team Nanotec, Germany) which have a cantilever spring constant of about 50 N/m and a tip radius of 60 nm.

3.2.2 Controlled relative humidity and AFM fluid cell

To investigate single fibers in an environment with defined RH, the AFM is equipped with a closed fluid cell (Asylum Research, USA) which can be flushed by nitrogen in a controlled way. The whole setup is pictured in Figure 3.9. It consists of a nitrogen flow which is divided into two lines (Figure 3.9a, b). One line stays dry and the nitrogen flows directly into a buffer bottle, whereas the nitrogen in the other line flows through a bubbler bottle which is filled with distilled water. From the buffer, the mixture of dry and humid nitrogen, of which the flow ratio can be controlled by valves, flows directly into the fluid cell (Figure 3.9c). Inside, a sensor monitors RH and temperature (SHT21, Sensirion, Staefa, Switzerland) and is placed very close to the sample holder. This RH setup has been successfully employed before, and a more detailed description can be found in [8],[9]. AFM measurements with fiber samples immersed in distilled water were also conducted in the fluid cell to prevent damage of the AFM by leaking water. A water droplet with a diameter of about 8 mm covered the fibers completely and remained there for a whole day enabling long-time stable measurements.
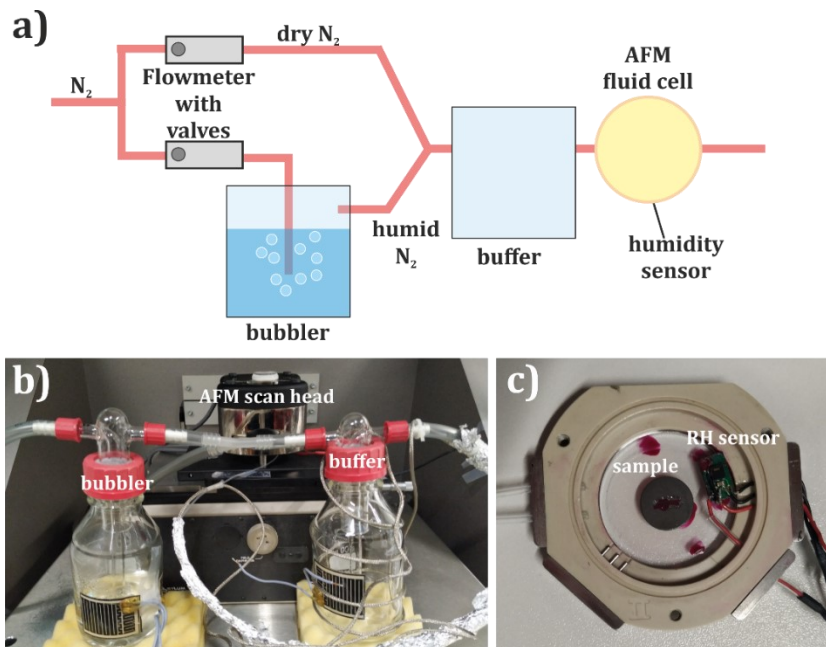

Figure 3.9: Relative humidity (RH) setup. In (a) the schematics of the whole setup are presented with the important elements. In (b), the whole system can be seen during experiments and (c) represents a top view of the AFM fluid cell.

3.2.3 AFM-based nanoindentation (AFM-NI)

First, the surface to be tested is scanned in tapping mode to locate sufficiently flat regions. Then, deflection-z plots were recorded in contact mode at the desired position. For all measurements, the same load schedule was used. The load schedule consists of one hold time at maximum load and a second hold at the end of the unloading segment, as is presented in Figure 3.10. For all un-/loading ramps, a constant load rate was used. The parameters were F_{max} = 10 μN, $\dot{F}$ = 10 μN/s, t_{max} = 10 s, and t_{hold} = 30 s.
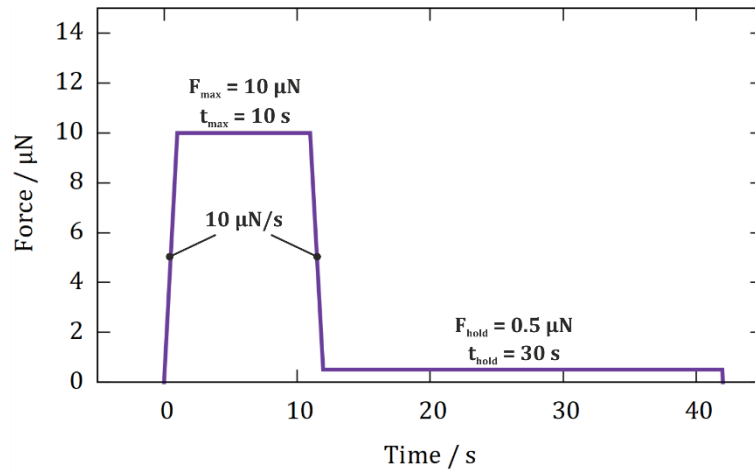
Figure 3.10: Load schedule for AFM-NI experiments.

3.2.4 Viscoelastic AFM-NI experiment

To determine the viscoelastic properties of pulp fibers [68], the load schedule presented in Figure 3.11 is applied. This is a modification of the load schedule used for PMMA and PC which has been thoroughly discussed elsewhere [67]. The load schedule consists of three main parts (a, b, c) which will be explained in the following. Below the load schedule in Figure 3.11, the tip-sample interaction during the experiment is illustrated.
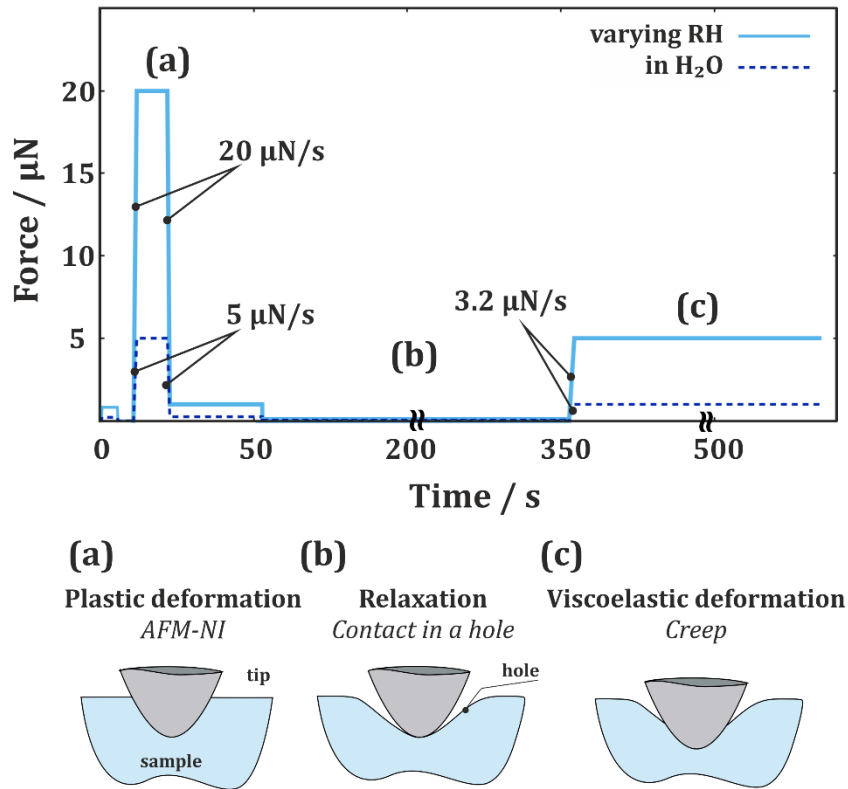
Figure 3.11: Load schedule for the viscoelastic measurements at varying RH (solid line) and in water (dashed line). The schedule consists of three parts. In (a), the sample surface is plastically deformed with a high force. During (b), the sample surface elastically recovers (300 s). As a consequence, the tip is located in a hole due to the plastic deformation. In (c), the surface is viscoelastically deformed (240 s) and this part of the curve is used for fitting with viscoelastic models.

In part (a) shown in Figure 3.11, a high load of 20 µN is applied for 10 s to introduce plastic deformation to the sample surface. Here, also values for the reduced modulus E_r and hardness H, as explained in the AFM-NI subsection, are obtained. Additionally, the plastic deformation makes it possible to characterize the contact between the tip and sample surface in a more defined way. It is assumed that most of the local roughness is reduced due to this deformation, and further plastic response is assumed to be eliminated. As illustrated in part (b) (Figure 3.11), the contact between tip and surface after the plastic deformation can be described as a contact in a hole. This was experimentally proven by scanning the surface after the plastic deformation by an AFM probe with a smaller tip radius and is presented in Figure 3.12 for viscose (Figure 3.12a) and pulp fibers (Figure 3.12b). Here, the ratio between the experimentally determined indent radius $R_{i,exp}$

(12 individual indents have been evaluated for each fiber type) and the tip radius R_{tip} is compared. The radius of the indent or hole – determined always parallel to the x-axis, as indicated in Figure 3.12 – is always larger than the tip radius. The values for the ratio between $R_{i,exp,}$ and R_{tip} are *8.6 ± 5.2* and *4.2 ± 2.3* for viscose fibers and paper fibers, respectively.
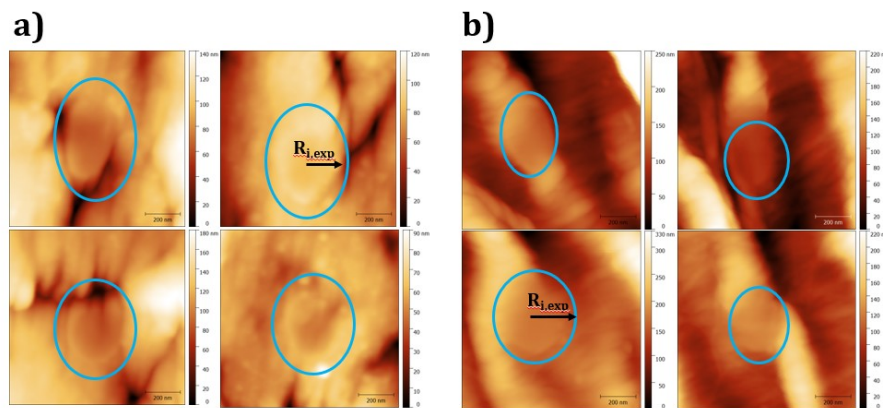

Figure 3.12: 1 x 1 μm² AFM topography images of indents on (a) viscose and (b) pulp fibers proving the assumption that during plastic deformation the tip is forming a hole which has a larger radius than the tip radius.

In part (b) of Figure 3.11, only the trigger force is applied for 300 s to allow the surface to recover. In part (c) of Figure 3.11, the viscoelastic response of the sample surface is tested. Here, a load of 5 μN with a loading rate of 3.2 μN/s is applied for 240 s. The obtained creep curves are analyzed for the evaluation of the viscoelastic properties. With increasing RH value, the indentation depth increased very little with δ_{max} /RH = 0.6 nm / %. This resulted in a maximum penetration depth of about 60 nm at 75% RH. However, measurement attempts of the fiber surfaces in water applying the same load schedule resulted in high indentation depths (more than 1 μm). Consequently, elastic deformation could not be maintained. For this reason, the load schedule was changed to lower force values, as indicated in Figure 3.11 by the dashed line. In Figure 3.11 part (a) only a load of 5 μN instead of 20 μN is applied in water. During the viscoelastic testing in Figure 3.11 part (c) under water, the load is adjusted to 1 μN. The load rates are identical.

For the evaluation of the viscoelastic properties of the polymer samples PMMA and PC, the load schedule presented in Figure 3.11 was slightly modified to a shorter relaxation time (60 s) and shorter holding times (120 s at 5 μN and 60 s after unloading) during the

viscoelastic part, as illustrated in Figure 3.13. The reason is the shorter relaxation behavior of the polymers after the plastic deformation and the less pronounced viscoelastic creep behavior compared to the investigated cellulosic fibers. The load rates are identical as indicated in Figure 3.11.
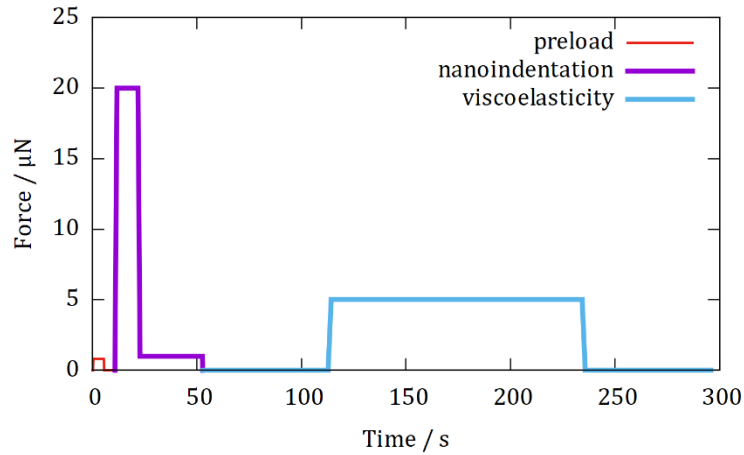

Figure 3.13: Load schedule for the viscoelastic testing of the polymers PMMA and PC.

3.2.5 Viscoelastic parameter study

To properly understand the viscoelastic models that have been used in this work, a comprehensive parameter study has been obtained to understand the function of the single elements in the spring-dashpot models. The effect of certain parameters of the measurement has been studied as well. Some parameters were kept constant and close to experimental conditions.

Influence of different load rates

As presented in Figure 3.14, the loading rate can influence the detection of the viscoelastic properties of a material significantly. Here, the study was obtained for a GM2 model with the parameters E_∞ = 1 GPa, E_1 = 1 GPa, E_2 = 1 GPa, τ_1 = 1 s and τ_2 = 100 s. Three

40

different load rates of 0.8 µN/s, 1.6 µN/s, and 3.2 µN/s were tested for an applied load of 5 µN. If loading is too slow, but viscoelastic effects appear immediately after loading, it is possible that these effects are not – or to a lesser amount – observed once the full load is applied. This difference can be recognized when the load rate of 0.8 µN/s is compared with the load rate of 3.2 µN/s. Whereas the curve with the fast load rate takes about 2 s after loading to reach the maximum indentation depth, the curve with the slow loading rate reaches immediately after loading the maximum indentation depth because any viscoelastic effects have time to happen during this long loading period. This means that all the viscoelastic effects are limited by the load rate. Any relaxation taking place during the load time is not detected. Therefore, it is important to choose a fast loading rate. In this work, 3.2 µN/s was applied to all viscoelastic measurements and proved to be sufficient.
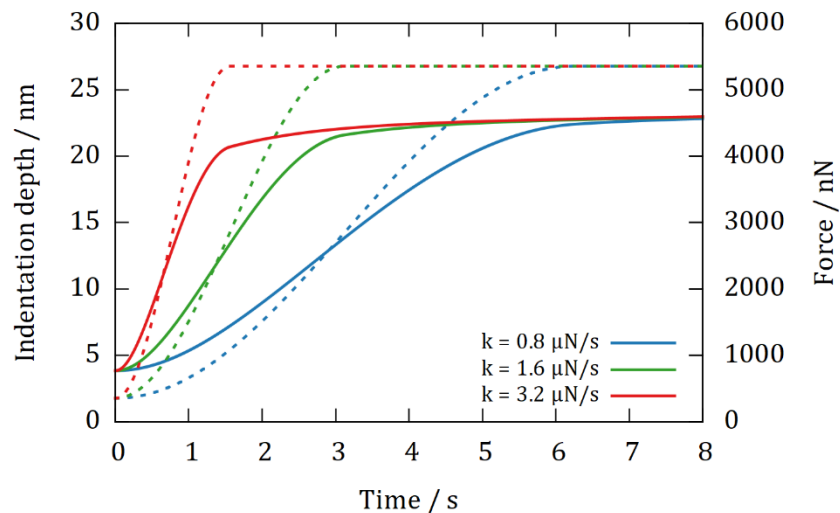

Figure 3.14: Effect of different load rates on the creep curves with the corresponding force loads presented as dashed lines.

Comparison between viscoelastic SLS and GM2 model

In Figure 3.15, the difference between the SLS model (Figure 2.7c) and the GM2 model (Figure 2.8a) is presented. The GM2 model is the SLS model with another Maxwell element added. Therefore, the SLS model is characterized by one relaxation time τ_1, whereas the GM2 model is based on two relaxation times τ_1 and τ_2. For small relaxation times, the difference between the curves is almost negligible and only visible during loading,

whereas for high τ_2, the addition of another Maxwell element exhibits a larger effect and influences the whole curve (red curves).
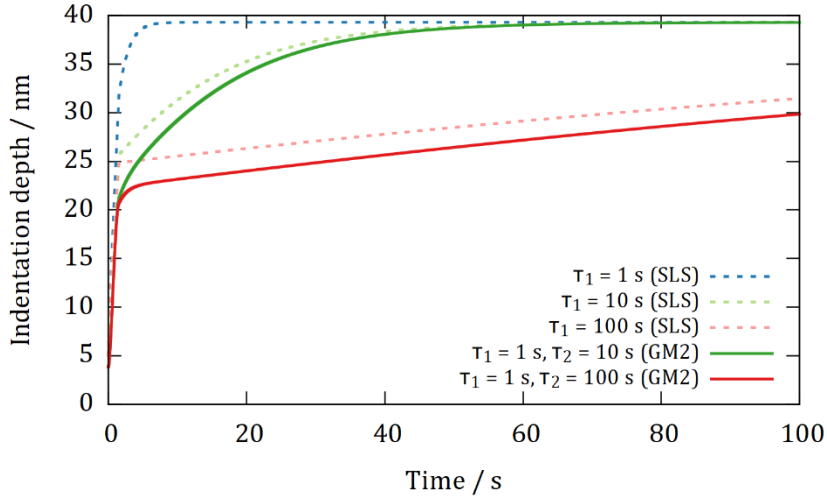

Figure 3.15: Comparison between the viscoelastic SLS (dashed line) and GM2 model (solid line).

For better visualization, a spectral representation of the viscoelastic parameters of the different spring – dashpot models can be useful as well [112]. To calculate the spectrum, the complex modulus $E^* = E' + iE''$ needs to be introduced [113]. It consists of the so-called storage modulus E', which is a measure of the elastic response of the material and the loss modulus E'', describing the viscous response of the material. For the GM model of different modes n, which is used throughout this thesis, the following equations apply.

$$E'(\omega) = E_\infty + \sum_{i=1}^{n} E_i \frac{(\omega\tau_i)^2}{1 + (\omega\tau_i)^2} \tag{11}$$

$$E''(\omega) = \sum_{i=1}^{n} E_i \frac{\omega\tau_i}{1 + (\omega\tau_i)^2} \tag{12}$$

Furthermore, the loss tangent *tanδ*, which is associated with the ratio of the energy dissipated and stored and which provides a measure of the damping in the material can be defined as,

$$\tan\delta(\omega) = \frac{E''}{E'} \tag{13}$$

The spectra of $E'(\omega)$, $E''(\omega)$ and $tan\delta(\omega)$ for the SLS and the GM2 model, which are presented in Figure 3.16, are computed as a sum of the Maxwell elements according to Eq. 11-13. For the SLS model, the elastic parameters E_∞ = 1 GPa, E_1 = 1GPa have been assumed and the relaxation time has been varied to τ_1 = 1, 10, and 100 s. For the GM2 model, the elastic parameters E_∞ = 1 GPa, E_1 = 1GPa, E_2 = 1 GPa have been assumed with the relaxation time τ_1 fixed at 1 s, but varying τ_2 (10 s or 100 s). The relaxation time τ_i of a single Maxwell element determines its active frequency band. Therefore, the spectra are plotted in an angular frequency range between 0.001 and 10 rad/s. Consequently, one Maxwell element is referred to as one mode of the spectrum. This is visible by comparing the two models. The SLS model consists of only one Maxwell element with one relaxation time. This results in one transition for the storage modulus in Figure 3.16a, one peak for the loss modulus in Figure 3.16b, as well as one peak for the loss tangent in Figure 3.16c – always at the corresponding frequency of the relaxation time. For the GM2 model, two Maxwell elements are at play with two relaxation times, which result in two transitions in the storage modulus in Figure 3.16a, as well as two peaks for the loss modulus (Figure 3.16b) and loss tangent (Figure 3.16c). Again, the transitions and peaks are always at the corresponding frequency of the relaxation time. By varying the second relaxation time τ_2, the shape of the transitions and overlaps of the peaks are determined.
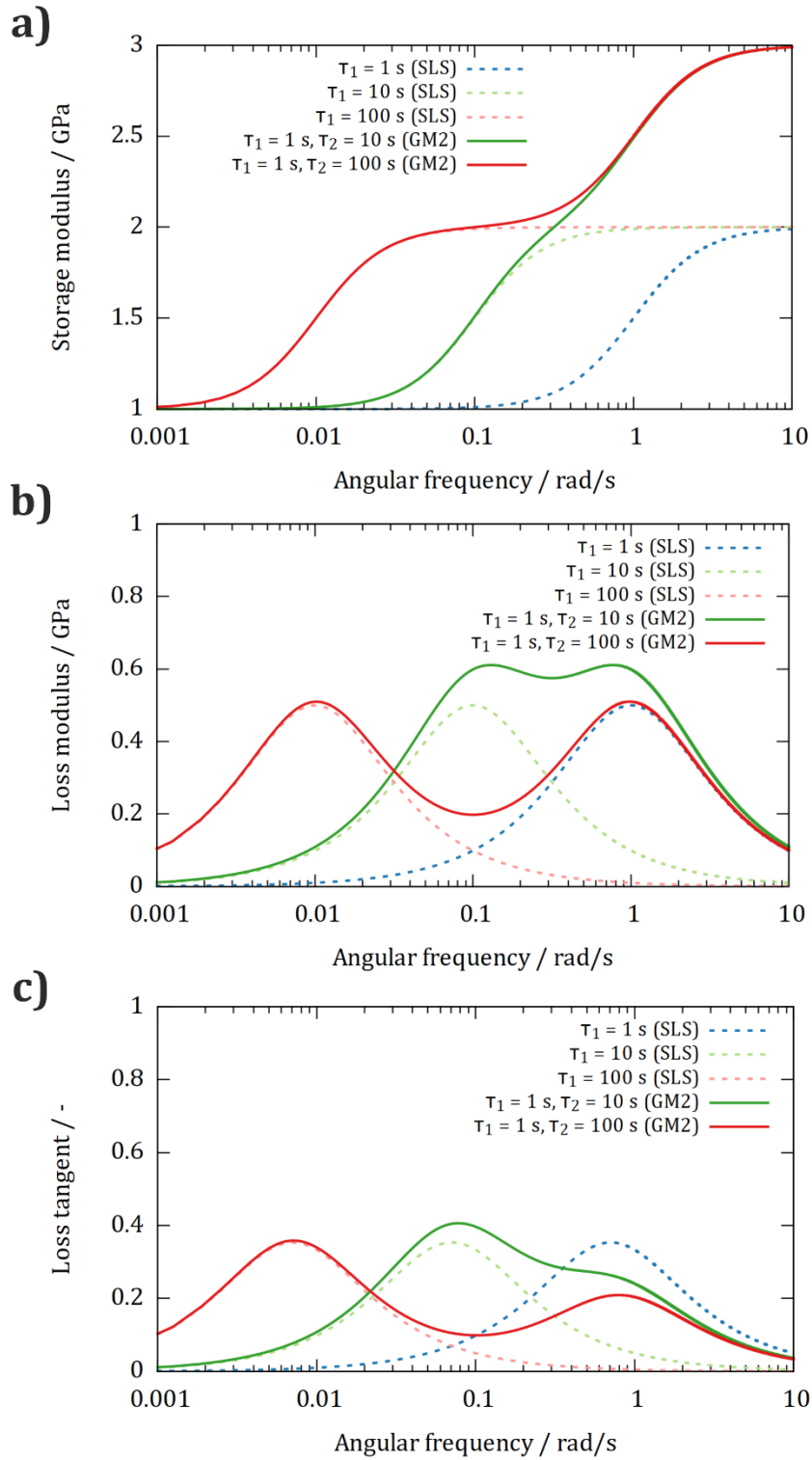
Figure 3.16: Spectral representation of (a) storage modulus E'(ω), (b) loss modulus E''(ω), and (c) loss tangent tanδ(ω) for the SLS and GM2 model with varying relaxation times. SLS parameters: E_∞ = 1 GPa, E_1 = 1 GPa, τ_1 = 1 s, 10 s or 100 s, GM2 parameters: E_∞ = 1 GPa, E_1 = 1 GPa, E_2 = 1 GPa τ_1 = 1 s, τ_2 = 10 s or 100 s.

Influence of varying E_∞ and varying relaxation times τ_i on the curves of the GM2 model

As in this thesis, the GM2 model is frequently used, a study has been performed to investigate the influence of the different parameters of the model on the resulting creep curve. As presented in Figure 2.8a, the GM2 model consists of three springs E_∞, E_1, E_2, and two dashpots η_1, η_2. Additionally, two relaxation times τ_1, τ_2 can be defined. The single spring E_∞ in the GM2 model keeps the whole model elastic. If this spring would not be in place, the dashpots of the Maxwell elements would cause permanent deformation. As is illustrated in Figure 3.17a, the lower the value of E_∞, the higher the indentation depth and the steeper the slope of the indentation curve. The influence on the slope is even bigger when one of the relaxation times is varied, as presented in Figure 3.17b. For $\tau_2 = 100\ s$, the indentation curve is not reaching the maximum indentation in the experimental time window and would continue to creep.
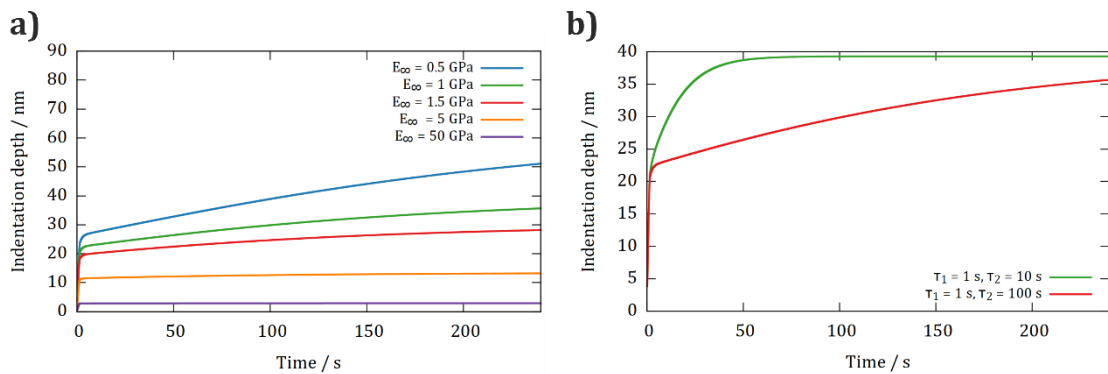

Figure 3.17: Influence of varying (a) E_∞ and (b) τ_2 on the indentation curve.

3.2.6 Force spectroscopy and FFM experiments

Before FFM measurements, AFM force spectroscopy measurements to investigate the adhesion properties of the film surfaces were performed with a scan rate of 2 Hz and a force distance of 0.5 µm. 32 × 32 px^2 maps were obtained on 5 × 5 µm² topography scans. In addition to the adhesion force, the elastic modulus has been evaluated by fitting the Hertz model to the approach part of the force-distance curve. For FFM, 5 × 5 µm² contact mode AFM images including the lateral trace and retrace channel were recorded with a

scan speed of 2.5 μm/s. During these measurements, a vertical force of about 10 nN was applied with the CSG10/Au probes. To eliminate a possible offset and topography artifacts, the raw lateral signals were converted to friction images by subtracting the lateral retrace from the lateral trace signal and dividing it by a factor of two for each image: *friction force = (FFM trace - FFM retrace)/2* [103],[114],[115]. The quantitative interpretation in terms of friction coefficient is not straightforward, and literature includes several calibration methods [72]. Here, the lateral force sensitivity was calibrated according to the wedge calibration method of [116]. Quantitative friction images are obtained by multiplying the resulting friction image data with the lateral force sensitivity using the Gwyddion software [117].

3.3   Nanoindentation (NI) and tensile tests for polymer samples

For the validation of the viscoelastic AFM method, NI and tensile tests have been performed on PMMA and PC samples.

NI experiments were performed by Thomas Schöberl from Erich Schmid Institute, ÖAW Leoben, using a Hysitron Triboscope (Hysitron, Minneapolis, USA), an add-on instrument mounted on the scanner unit of a Dimension D3100 (Bruker, Billerica, USA) AFM. The tests were performed in load-controlled mode with a conical diamond tip having an average tip radius of 4.81 μm and an opening angle of 60°. The load schedule of the viscoelastic AFM tests (Figure 3.11) was adapted for NI to scale the indentation depths with the tip radius. The loading times stayed the same, but the maximum force during the plastic deformation was raised to 3.8 mN, whereas the constant force for the determination of the viscoelastic properties was 1 mN. The part of the load schedule with the maximum force was performed in an open-loop, while the constant force was measured in a closed-loop. The evaluation of the data was performed in the same manner as for the AFM results by Christian Ganser.

Creep tensile tests on PMMA and PC were performed by Daniel Tscharnuter of PCCL Leoben using an Instron 5500 electro-mechanical testing device with pneumatic grips and a 10 kN load cell. Here, monotonic tensile tests were performed to determine the nominal

stress with an initial strain at 0.5 % and 1 % for three samples each. This way, nonlinear effects should be minimized.

3.4   Raman Spectroscopy

Raman analysis was performed with a Horiba HR Evolution Nano system (Horiba, France). The system is equipped with a red (633 nm) and green (532 nm) laser and two different gratings (600 and 1800 gr/mm). Here, the red laser has been used in combination with the 1800 gr/mm grating.

3.5   Confocal Laser Scanning Microscopy (CLSM)

A confocal laser scanning microscope (CLSM) Olympus LEXT 4100 OLS was employed with the help of Oleksandr Glyshko at the Erich Schmid Institute Leoben for optical 2D and 3D imaging of the fiber cross-section samples. The laser wavelength is 405 nm and the lateral resolution is 120 nm. The z-resolution is theoretically as small as 10 nm due to a multi-focusing algorithm.

3.6   AFM Data Analysis

Processing of the recorded AFM images has been performed with the open-source software Gwyddion [117]. The AFM-NI evaluation is based on the automated AFM-NI procedure established by Christian Ganser which has been thoroughly described in [9],[85]. The viscoelastic evaluations have been performed with MATLAB and GNU/Octave compatible codes that have been developed for the GM2 model combined with JKR contact mechanics by Christian Ganser [67] and modified by Tristan Seidlhofer and the author [68]. Furthermore, Tristan Seidlhofer also developed a code for the viscoelastic evaluation of experimental AFM data with a GMn model with n Maxwell

elements [118]. This code has been applied to the experimental data of the water measurements of pulp and viscose fibers and the comparison between longitudinal and transversal direction.

In sections 4.1-4.3, a code by Christian Ganser has been used that solves – for each averaged curve – the differential equation of the GM2 model (Eq. 3) numerically by using an implementation of Hindmarsh's solver [119] in GNU/Octave. This numerical solution is then fitted to the data with a GNU/Octave implementation of the Levenberg-Marquardt method [120].

For the water measurements in section 4.2 and throughout section 4.4, a code written by Tristan Seidlhofer has been applied. Here, the Prony series [121]

$$E(t) = E_\infty + \sum_{i=1}^{n} E_i exp^{\left(\frac{-t}{\tau_i}\right)}$$ (14)

has been applied. It introduces alongside the equilibrium behavior E_∞, n relaxation modes defined by the magnitude E_i and the relaxation time τ_i. As the series approximates a continuous function, the τ_i can be imagined as supporting points in the time domain.

Here, the n relaxation times have been logarithmic evenly distributed over the relevant time scale, to avoid numerical difficulties when E_i had to be identified out of experiments. The logarithmic nature is a result of the exponential form of the Prony series. By introducing the Prony series, the functional representation can be turned into an internal variable representation which further leads to a set of n ordinary differential equations for the evolution of the internal state space. This internal state can be physically interpreted with the generalized Maxwell model (GM), which is mathematically equivalent to the Prony series representation [122].

4 Results

4.1 Validation of the AFM-NI viscoelastic method using polymers

Viscoelastic properties are quite often measured using techniques like nanoindentation (NI) and AFM, however, these measurements have been rarely verified. Here, the viscoelastic AFM-based method has been validated with well-known polymers – poly(methylmethacrylate) (PMMA) and polycarbonate (PC) – and compared to NI and tensile testing measurements. Large parts of chapter 4.1 have already been published in [67]. Here, the most important findings are highlighted, and results are only presented for the GM2 model since this model proved to be the most relevant one for all investigations in this thesis.

First, the topography of PMMA and PC has been investigated with AFM. Representative $5 \times 5\ \mu m^2$ topography images are presented in Figure 4.1. The surface is mostly characterized by scratches that originate from sample preparation. The root mean square (RMS) roughness is *(12.0 ± 1.4) nm* and *(8.5 ± 4.7) nm* for PMMA and PC, respectively. The RMS roughness was determined from three independent $5 \times 5\ \mu m^2$ topography images. Additionally, AFM-NI, as described in subsection 3.2.3, has been performed to characterize the mechanical properties of the polymer samples by the reduced modulus E_r and hardness H. For PMMA, the evaluation resulted in E_r *= (2.8 ± 0.5) GPa* and H *= (450 ± 90) MPa*, whereas for PC, the values are E_r *= (1.5 ± 0.4) GPa* and H *= (145 ± 25) MPa*. (The values are given as mean ± standard deviation and are averages of around 600 single measurements per material.) The results reveal that PMMA has a higher elastic modulus and hardness than PC. This is in agreement with literature values of conventional NI [123],[124].
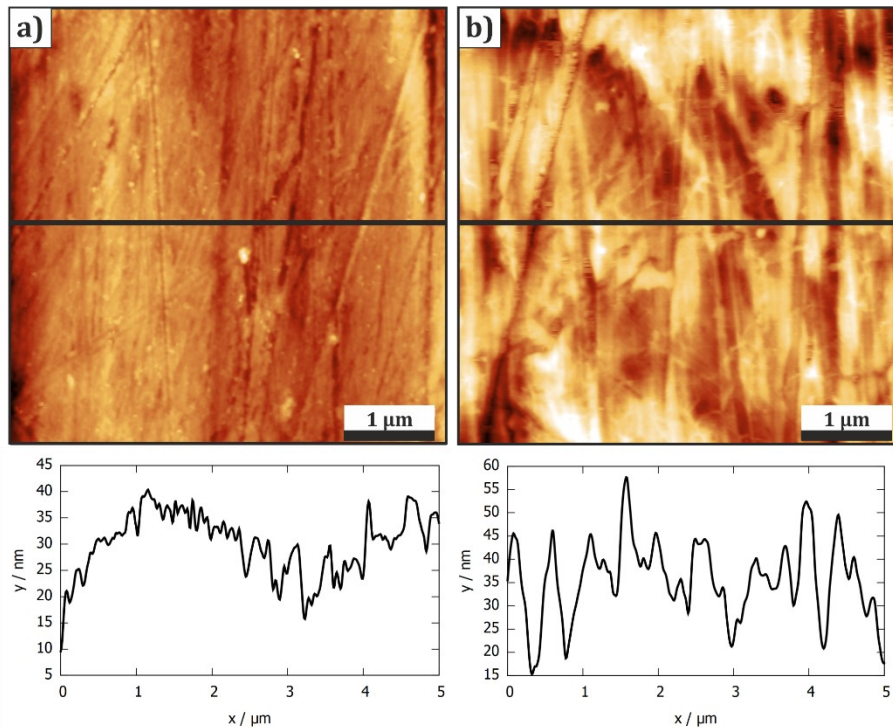
Figure 4.1: Representative 5 x 5 µm² topography images (z-scale: 60 nm) of (a) PMMA and (b) PC with line profiles of the surface which are indicated by a black line in the topography images.

Creep curves of both polymers were recorded by mapping a 5 x 5 µm² topography area with a regular grid of force distance measurements. For PMMA, maps were recorded on 11 positions resulting in 404 curves and for PC, 16 positions were mapped resulting in 576 curves.

Individual evaluation of the creep curves and averaging of the parameters afterward result in large scattering of the data. Reliable detection of the parameters is not possible this way. The cause is most likely thermal drift and noise. In Figure 4.2, creep curves of single measurement points are presented. The maximum indentation depth of these curves does not exceed 20 nm for both, PMMA (Figure 4.2a) and PC (Figure 4.2b). At such low indentation depths, thermal drift and noise become non-negligible and influence the evaluation procedure. To compensate these effects, creep curves of one map (containing 36 single measurement points) were averaged. Afterward, these averaged curves were evaluated according to the viscoelastic method. In Figure 4.2, also averaged curves for PMMA (Figure 4.2a) and PC (Figure 4.2b) are presented. It is visible that the signal-to-noise ratio improved with the averaging strategy.
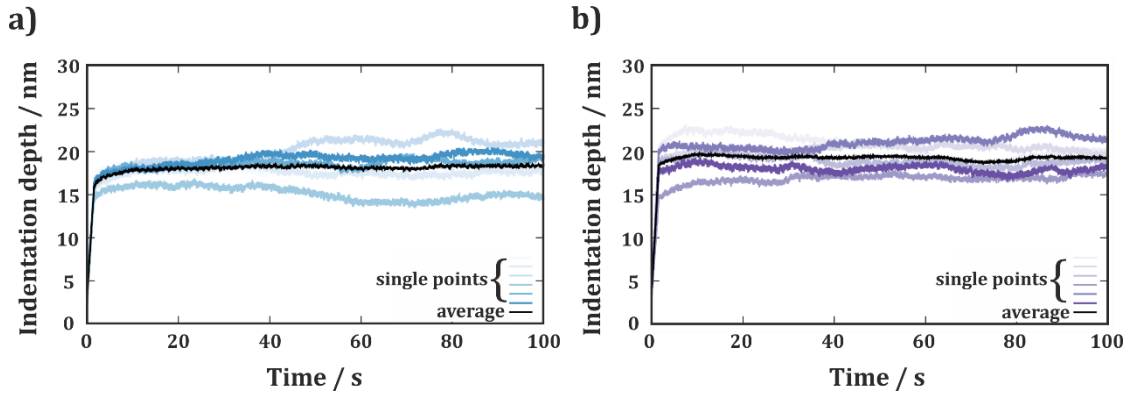
50

Figure 4.2: Creep curves illustrating the improvement of signal-to-noise ratio between curves of single measurement points and average curves (black) of multiple measurement points for (a) PMMA, and (b) PC. After [67].

For the evaluation of the experimental data, JKR contact mechanics is combined with the GM2 model. It was necessary to use the JKR contact model because adhesion forces cannot be neglected and have values of *(314 ± 49) nN* and *(208 ± 44) nN* for PMMA and PC, respectively.

As has been described in 2.4, the viscoelastic characterization of a material by the GM2 model consists of three elastic (E_∞, E_1, E_2) and two viscous (η_1, η_2) parameters. Additionally, two relaxation times τ_1, τ_2, and the instantaneous modulus $E_0 = E_\infty + E_1 + E_2$ can be defined. In Figure 4.3-4.5, the results of the viscoelastic evaluation for PMMA (a) and PC (b) with all experimental methods are presented.

In Figure 4.3, the E_∞ and E_0 values of PMMA are larger than the corresponding values for PC for all the experimental methods. This is confirming the results obtained by AFM-NI and literature values. Furthermore, a trend that $E_\infty > E_1 > E_2$ is clearly visible. The elastic values obtained by AFM show the same trend as the NI values. For the NI results, the E_∞ values for PMMA and PC are identical, and the difference between the elastic parameters is not as pronounced as obtained by AFM. The values for E_∞ and E_0 of the tensile tests are quite similar to those measured by AFM and NI. Only the parameters E_1 and E_2 show a larger deviation, especially for PC (Figure 4.3b).
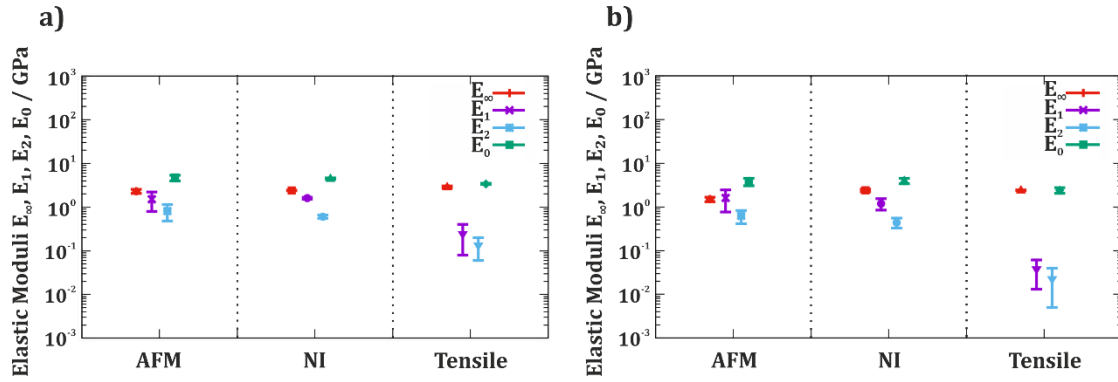
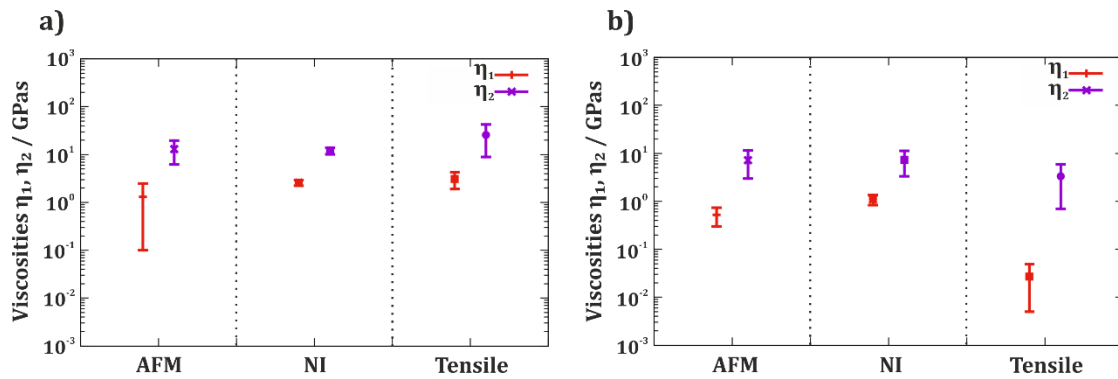*Figure 4.3: Elastic parameters E_∞, E_1, E_2, E_0 obtained by AFM, NI, and tensile testing for (a) PMMA and (b) PC. The values are shown as mean ± standard deviation and are averages of 404 (AFM), 20 (NI) and 6 (tensile) values for PMMA and 576 (AFM), 25 (NI), 6 (tensile) values for PC. After [67].*

In general, the viscosities η_1, η_2 are higher for PMMA compared to PC as presented in Figure 4.4. The values for η_2 are very similar for AFM and NI, but the NI results show a lower scattering of the values. For PMMA, the tensile testing results are in the same range as the values obtained by AFM and NI, but for PC (Figure 4.4b) the value of the viscosity η_1 shows a drop of about one order of magnitude compared to the AFM and NI value.

Figure 4.4: Viscosities η_1, η_2 obtained by AFM, NI, and tensile testing for (a) PMMA and (b) PC. The values are shown as mean ± standard deviation and are averages of 404 (AFM), 20 (NI) and 6 (tensile) values for PMMA and 576 (AFM), 25 (NI), 6 (tensile) values for PC. After [67].

With Equation 1, the corresponding relaxation times τ_1 and τ_2 of the GM2 model can be calculated. This has been done with the mean values of E_1, E_2 and η_1, η_2 and is presented in Figure 4.5. Again, the values obtained for PMMA are higher for all techniques compared

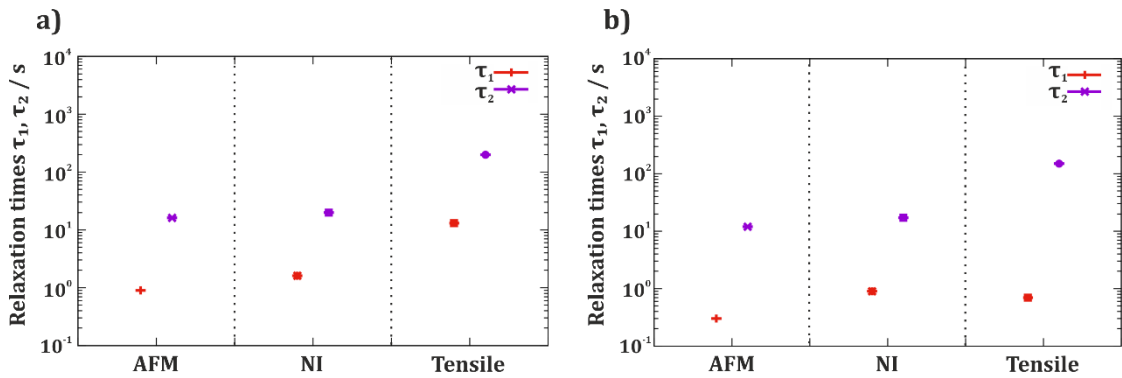to PC. Also, AFM and NI show similar values – as can be expected. The tensile testing results in a larger value for τ_2.

Figure 4.5: Relaxation times τ_1, τ_2 obtained by AFM, NI, and tensile testing for (a) PMMA and (b) PC.

In summary, good agreement between the results of the NI and AFM measurements has been found, the values show the same trend. Also, both indentation techniques are – except for the values of E_1, E_2, and η_1 – comparable to tensile testing. In tensile testing, the whole sample is in tension, whereas in AFM-based methods and NI the surface is only locally compressed, hence the local plastic deformation is hindered by the undeformed surrounding material. Overall, the AFM method to test viscoelasticity can provide results that are well comparable to NI, though showing larger scattering.

4.2 Viscoelastic properties of pulp and viscose fibers

Changes in moisture content of single pulp fibers have an immense influence on the behavior of paper and paper products. In this chapter, the AFM-based method to investigate viscoelastic behavior in transverse direction is applied to study pulp fibers at varying RH and immersed in water. Large parts of chapter 4.2 have already been published in [68]. Furthermore, the results obtained for pulp fibers are compared to measurements of viscose fibers in transverse direction.

In Figure 4.6, 5 x 5 μm^2 topography images of a pulp fiber (Figure 4.6a, b) and a viscose fiber surface (Figure 4.6c, d) are presented at ambient conditions (~45 % RH). The same position on each fiber has been investigated first with a large radius hemispherical AFM probe (Figure 4.6a, c) and later on with a standard AFM probe with a much smaller tip radius (see Chapter 3.2.1) to visualize the influence of the tip radius on the lateral resolution. In the topography images which have been recorded with a large radius probe, the single fibrils and features with smaller sizes are not clearly resolved due to the lower lateral resolution. With the smaller tip radius, more surface details are visible. The pulp fiber has a very rough surface which is characterized by wrinkle-like structures originating from the shrinking of the fiber during drying. The RMS roughness of the topography in Figure 4.6b is *(150 ± 62) nm* (obtained from 6 positions on 3 fibers). Compared to that, the viscose fiber surface in Figure 4.6d appears smoother with an RMS value of *(45 ± 24) nm* (obtained from 8 positions on 2 fibers) and has rather aligned wrinkles and characteristic trenches which are caused by the fabrication process. For the pulp fibers, mostly the surface of the S1 layer is investigated which was confirmed in morphological studies with AFM [125]. This is because during kraft pulp processing most of the primary wall layer is removed due to its high lignin content [26].
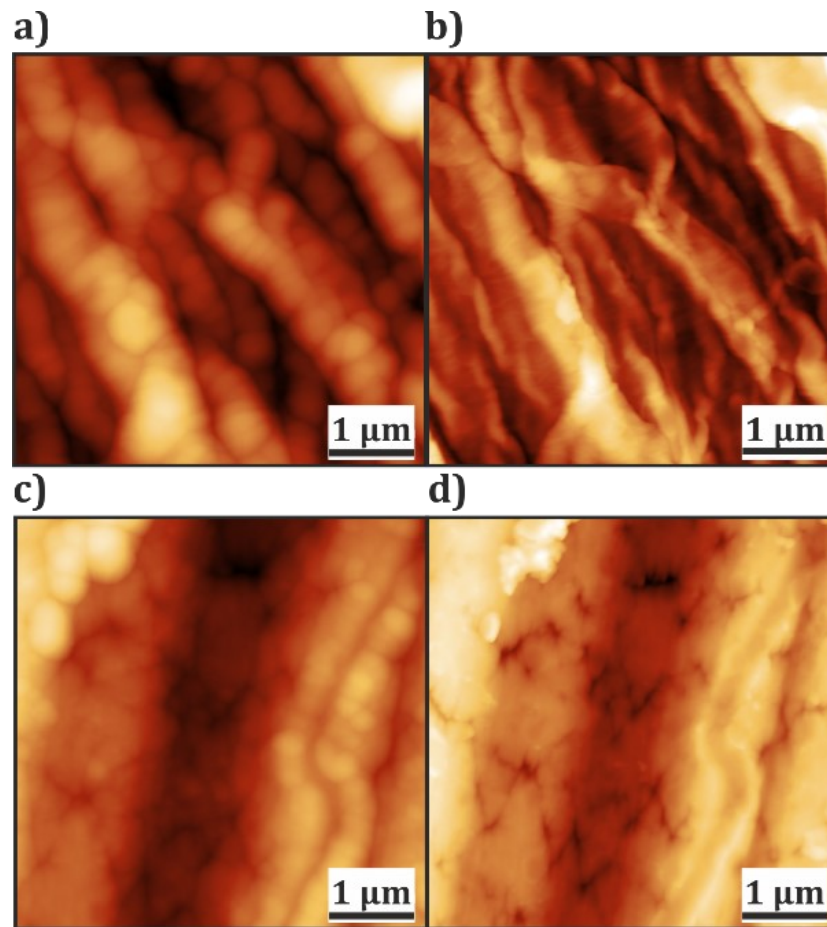
Figure 4.6: 5 x 5 µm² topography images of (a, b) a pulp fiber surface (z-scale: 600 nm) and (c, d) a viscose fiber surface (z-scale: 500 nm) at ambient conditions (~45 % RH). The first images of each row (a, c) have been recorded with a large radius AFM probe, whereas the second images of each row (b, d) have been recorded with a standard AFM probe.

Representative 5 x 5 µm² AFM topography images of a pulp and a viscose fiber surface at 60 % RH and recorded with a 300 nm radius probe are presented in Figure 4.7. On these surface areas, individual measurement points were selected for the viscoelastic experiment. The topography of the pulp and viscose fibers is presented before (Figure *4.7*a, c) and after (Figure 4.7b, d) the AFM experiment. Single positions on the pulp and viscose fiber are indicated in Figure 4.7a, c with black dots. The viscoelastic experiment has been performed on rather smooth positions of the surfaces. The wrinkle-like structures on the surface of the pulp fibers have a similar lateral size as the AFM tip diameter which is indicated by black dots. During the indentation, lateral movement of the wrinkles perpendicular to the longitudinal fiber axis cannot be excluded. However, it is

assumed that most of this movement is taking place during the plastic deformation, where four times higher load is applied than during viscoelastic testing (as has been discussed in section 3.2.4).
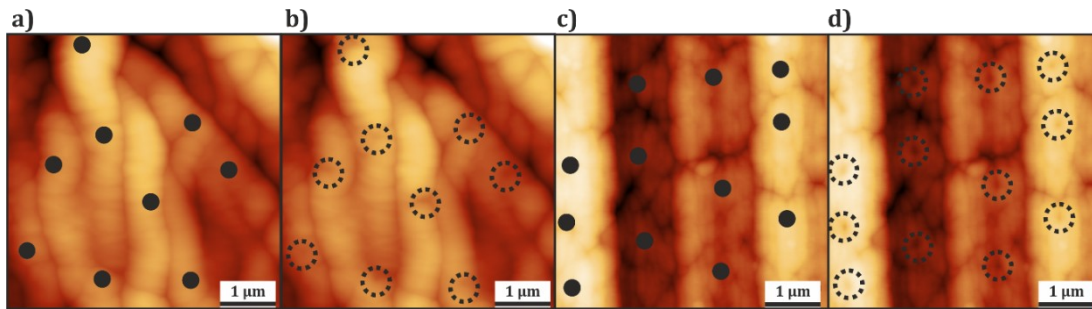

Figure 4.7: 5 x 5 µm² AFM topography images at 60 % RH. Topography images of a pulp fiber surface (a) before and (b) after the viscoelastic testing experiment (z-scale: 900 nm). Topography images of a viscose fiber surface (c) before and (d) after the experiment (z-scale: 350 nm). The black dots indicate measurement points whereas the black dashed circles mark the permanent holes after the experiment.

Averaged experimental creep curves with corresponding GM2 fits at different RH are presented for pulp and viscose fibers in Figure 4.8. For pulp fibers, in Figure 4.8a, curves at 10 %, 25 %, 45 %, 60 %, and 75 % RH have been recorded. The indentation depth increases with increasing RH, ranging from about 10 – 100 nm. The same trend is apparent for the viscose fibers (Figure 4.8b), but the indentation depth is much lower. For 35 %, 60 %, and 80 % RH, the AFM tip is only penetrating 10 – 50 nm into the surface of the viscose fibers. Since experiments with indentation depths smaller than 10 nm show a high influence of signal noise coming mostly from the controlled humidity setup (scattering of the data is about 2 nm), no measurements for viscose fibers at RH lower than 35 % have been performed. In general, the GM2 model fits the data at different RH very well, with slight deviations at the beginning of the curve at 75 % RH.
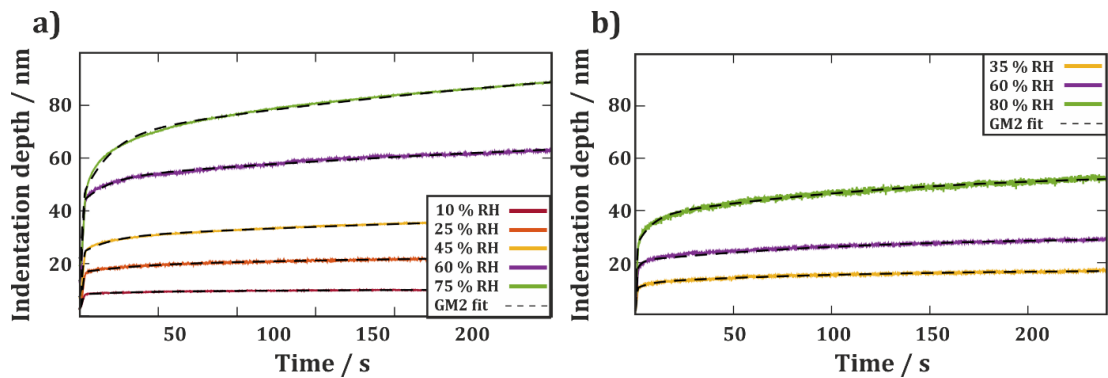
Figure 4.8: Representative experimental creep curves (a) for pulp fibers at 10 %, 25 %, 45 %, 60 %, and 75 % RH, and (b) for viscose fibers at 35 %, 60 %, and 80 % RH with the corresponding fit curves as black dashed lines. After [68].

For measurements of the pulp fibers in water, the situation is different. This can already be seen by looking at the plot of the maximum indentation depth δ_{max} of the viscoelastic experiments depending on RH presented in Figure 4.9. For the RH range from 10 % to 75 %, δ_{max} is increasing linearly with 0.6 nm / %, resulting in a maximum indentation depth of about 60 nm at 75 % RH. However, immersed in water the δ_{max} value increases by a factor of 10 compared to the value at 75 % RH. This results in a maximum indentation depth of about 140 nm though the applied force is only 1 µN instead of 5 µN, as mentioned in chapter 3.2.4.
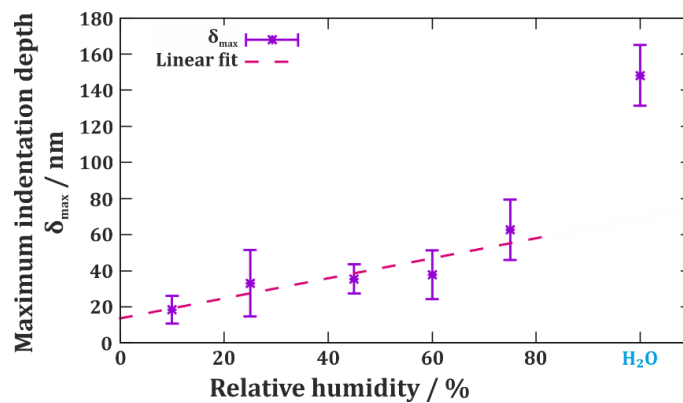

Figure 4.9: Maximum indentation depth δ_{max} for pulp fibers at different RH and in water. The pink dashed line indicates the linear fit of the RH values with δ_{max} (RH) = 0.6 nm / %. The values are plotted as mean ± standard deviation of at least 40 experimental curves per RH value.

Furthermore, it was found that the GM2 fits show deviations for the experimental data of the water measurements, which are presented in Figure 4.10a, b. The GM2 model is not fitting the data appropriately over the whole experimental time scale of 240 s. By adding a third Maxwell element, and – therefore, applying a Generalized Maxwell model of order three (GM3) – the fitting improves (Figure 4.10a, b). For the evaluation procedure of the GM3 model, the values for the relaxation times were fixed (τ_1 = 1 s, τ_2 = 5 s, τ_3 = 100 s), and only the four parameters for the elastic moduli were fitted. Since the fit showed most deviation at the beginning of the curve, the additional relaxation time was needed to be smaller (τ_1 = 1 s), whereas τ_2 and τ_3 are the approximate values obtained at 75 % RH. This was mostly done to avoid convergence problems and too many fitting parameters.

In contrast, similar behavior in water was not found for viscose fibers (Figure 4.10c, d). Although the indentation depth increases to values as high as 300 nm at the much lower load of 1 μN, the GM2 model still fits the data well, as presented in Figure 4.10c, d.
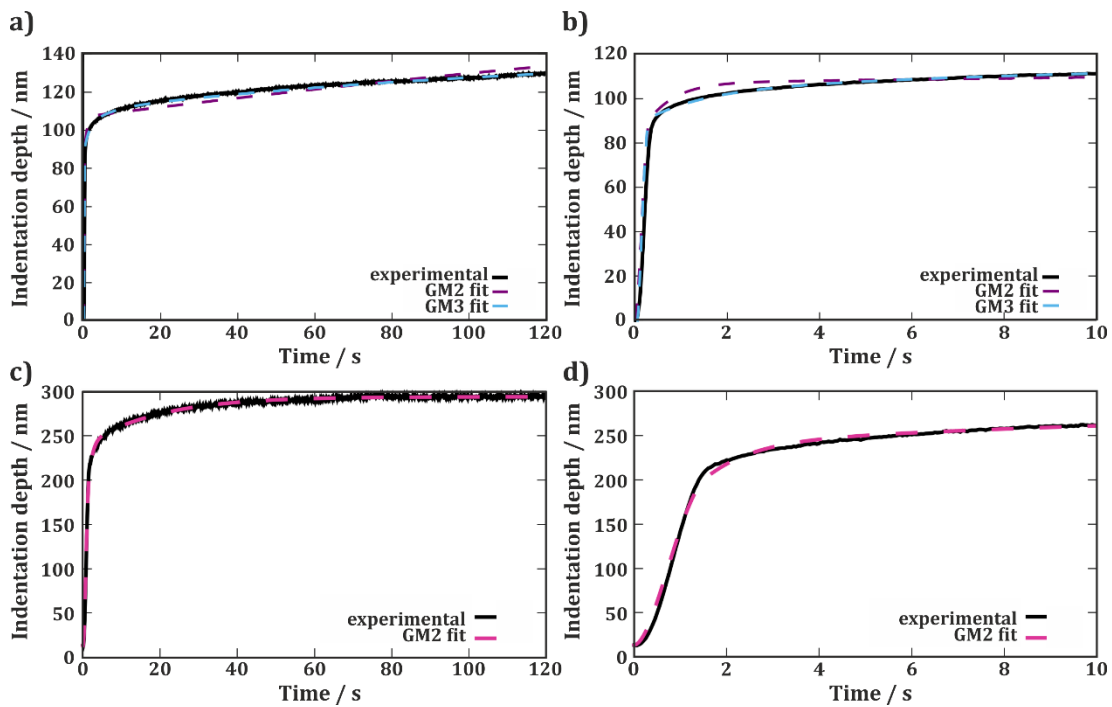

Figure 4.10: (a, b) Comparison of the fits (dashed lines) of the GM2 and the GM3 model for the same representative experimental curve (solid black line) of a measurement position under water for a pulp fiber. In (b), the first 10 s of the same experiment are presented. (c, d) Representative experimental creep curve (solid black line) with the corresponding GM2 fit (dashed line) for a viscose fiber. In (d), the first 10 s of the same experiment are presented.

In Figure 4.11, the results for the viscoelastic properties in transverse direction at different RH and in water from the GM2 model are presented for pulp and viscose fibers. For each RH and water value, at least 30 single measurement points for every fiber type have been evaluated. Figure 4.11a presents a comparison of the elastic moduli E_∞, E_0. Here, pulp and viscose fibers show a slightly decreasing trend from 10 % to 75 % RH and from 35 % to 80 % RH, respectively. Immersed in water, both fiber types exhibit the same drop of a factor of 100 compared to the lowest measured RH. Viscose fibers have at intermediate RH slightly higher elastic moduli than pulp fibers, but in water, they exhibit a decrease to lower values than for pulp fibers. In Figure 4.11b, the viscous behavior is characterized by the viscosities η_1, η_2. Here, both fibers again show a slight decrease with increasing RH and a more pronounced decrease immersed in water. Especially the results for the viscose fibers show little change between 35 % and 80 % RH, compared to the pulp fibers which decrease by one order of magnitude. In water, η_1 and η_2 of the viscose fibers are lower than for the pulp fibers.

For fibers immersed in water, the drop in elastic and viscous parameters indicates that the behavior of both fiber types is different in water compared to changing RH. This pronounced decrease of the elastic properties was already found with AFM-NI investigations [27, 109].
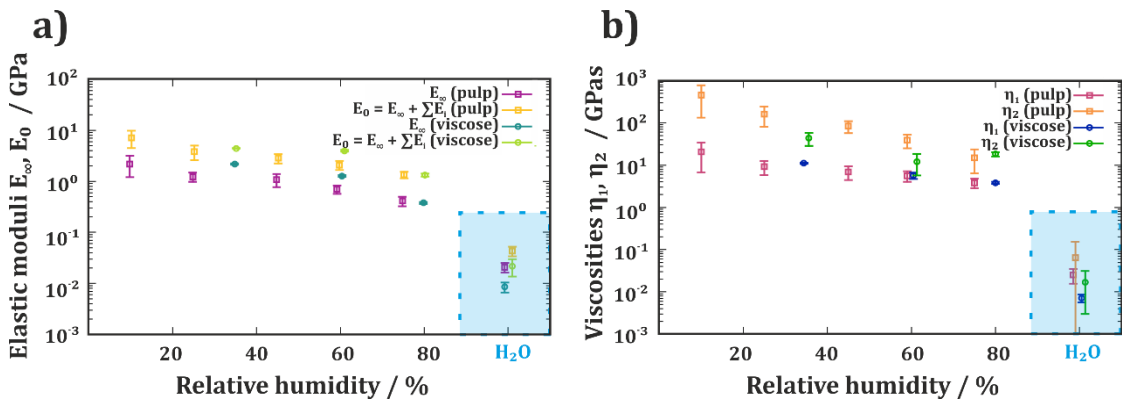

Figure 4.11: Results obtained by the GM2 model for pulp and viscose fibers. In (a) the elastic parameters E_∞ and E_0 are presented. In (b), the viscous parameters η_1 and η_2 are depicted. The squares and spheres indicate the results for pulp and viscose fibers, respectively. The values are plotted as mean ± confidence interval of 95 %.

In the literature, different experimental measurement techniques have been applied to study the elastic properties of wet fibers, like compression testing [110–112], osmotic swelling [129], or several AFM-based approaches. The conformability [130] and flexibility [131] of individual pulp fibers have been tested and AFM-NI has been applied to pulp and viscose fibers at different RH and in water [8],[107]. A comparison of the values for E_0 obtained with the viscoelastic model for the pulp (*28 MPa*) and the viscose (*22 MPa*) fibers in Table 3 reveals that most of the results obtained from AFM-based methods are in good agreement with each other.

Table 3: Overview of different experimental techniques to measure the transverse elastic modulus of pulp and viscose fibers.

Fiber type	Transverse elastic modulus / MPa	Experimental technique
spruce kraft pulp, κ = 42, earlywood, unbeaten	560	macroscopic transverse compression
spruce kraft pulp, κ = 42, earlywood, beaten	440	macroscopic transverse compression
Black spruce kraft and TMP, loblolly pine TMP	6.5-9.3	macroscopic transverse compression
Bleached softwood kraft pulp, κ = 1.2	1-12	fiber flexibility (AFM)
Unbleached, refined TMP pulp	15-190	fiber flexibility (AFM)
Spruce kraft pulp, κ = 61, unbeaten	13	fiber conformability (AFM)
TCF bleached softwood kraft, unbeaten	7	fiber conformability (AFM)
Spruce thermo-mechanical pulp	182	fiber conformability (AFM)
Spruce and pine kraft pulp, κ = 42, unrefined	32	AFM based nanoindentation
Viscose	50	AFM based nanoindentation
Low-yield spruce kraft, rewetted, unbeaten	4	osmotic swelling
Spruce and pine kraft pulp, κ = 42, unrefined	28	viscoelasticity (AFM)
Viscose	22	viscoelasticity (AFM)

Furthermore, it is possible to evaluate the plastic deformation part of the viscoelastic experiment (see Figure 3.11 (a)) with the Oliver and Pharr method, as described in chapter 2.7.1. The results for the reduced modulus E_r and the hardness H at different RH and in water for pulp fibers are presented in Figure 4.12. In Figure 4.12a, E_r is compared to the elastic modulus at infinitely slow loading E_∞ and the elastic modulus at infinitely fast loading E_0. As expected, the E_r value is for all RH values and in water always higher than the E_∞ value. Except for the water measurement, E_r is quite comparable to the E_0 value. The values obtained for H in Figure 4.12b show the same trend, a decrease of the values with increasing RH. In water, the values drop by about one order of magnitude compared to 75 % RH.
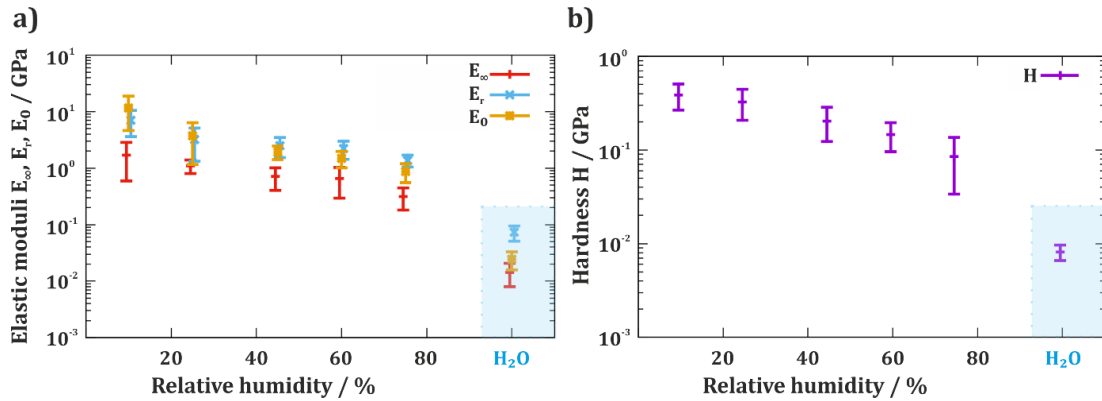
60

Figure 4.12: (a) Comparison of the elastic moduli E_∞ and E_0 from the viscoelastic model with the reduced modulus E_r obtained by AFM-NI for pulp fibers at different RH and in water. (b) Hardness H values obtained by AFM-NI for pulp fibers at different RH and in water. The values are plotted as mean ± standard deviation.

The viscoelastic properties of pulp and viscose fibers in transverse direction have been investigated with an AFM-based method. In this work, the combination of contact mechanics with a viscoelastic GM2 model enabled the measurement of local creep curves on both fiber types at different RH, ranging from 10 % RH to 75 % RH and in water. Moreover, the GM2 model provides for pulp as well as viscose fibers good comparability of the transversal viscoelastic behavior between the different RH. In general, both fiber types show the same trend for the elastic and viscous values. All the results for the parameters of the elastic and viscous behavior show a gradual decrease until the highest RH level. For fibers immersed in water, the decrease is even more pronounced, indicating that the mechanical behavior and, therefore, the interaction of the fibers with water is different. One explanation could be an additional, faster relaxation mechanism, as indicated with the introduction of a third relaxation time ($\tau_1 = 1\ s$) for the measurements of the pulp fibers in water. In water, poroelasticity might also play a larger role. Since the pulp fibers form a cellulose hydrogel-like material [45, 46] in the wet swollen state, the faster relaxation could be related to the displacement of water from the pores due to the pressure induced by the indenter. In summary, the results of the elastic moduli values for the wet pulp and viscose fibers are in good agreement with literature values which were also obtained with AFM-based experiments.

4.3   Model of a transverse isotropic viscoelastic pulp fiber

The availability of experimental mechanical data of the pulp fibers in transverse direction by AFM has initiated the development of a minimum-input material model for pulp fibers, in which the obtained data can be used as input parameters. This model is based on an incompressibility constraint to establish a well-defined parameter evaluation technique. The fibers have been experimentally tested with AFM-NI creep experiments in transverse direction and with creep uniaxial tension tests in longitudinal direction. AFM experimental data from measurements at 25 % RH have been used to characterize the viscoelasticity of the matrix material. The deformation has been kept small in all experiments, which allows parameter comparison to linear elasticity and the application of linear viscoelasticity theory. Large parts of chapter 4.3 have already been published in [112], where the doctoral candidate contributed as a second author. Here, a short description of the material model is given, and the usefulness of experimental AFM data for modeling approaches is presented.

In the model which has been developed by T. Seidlhofer at Graz University of Technology, a single pulp fiber is presented as a transverse isotropic viscoelastic material. The model is based on finite strain theory and includes an invariant-based strain energy function, consisting of an isotropic part which is extended additively with a reinforcing part based on structural tensors. This way, the elastic behavior is defined by two parameters only which can be obtained from the AFM and tensile test experiments. For the model, the pulp fiber was reduced to the S2 layer since it is known that the cell wall consists mostly of this layer (80-95 %) and because it is, therefore, responsible for mechanical strength. The S2 layer consists of a matrix, which is mainly composed of lignin and hemicellulose and reinforced by aligned microfibrils. Therefore, a material model with one preferred direction is needed, which is referred to as transverse isotropic in the literature.

Here, an invariant-based formulation for the isochoric model suitable for transverse isotropy and large deformations is employed. Only two parameters define this model: the shear modulus of the matrix μ_M and the reinforcing modulus E_R for the anisotropic contribution, i. e., the microfibrils. The elastic behavior of the fiber clearly shows a higher stiffness in the longitudinal direction than in the transverse direction. In the longitudinal direction, a combination of μ_M and the reinforcing modulus E_R governs the stiffness, while

in the transverse plane only the isotropic contribution with the matrix modulus μ_M is relevant. The Young's modulus E_L in the longitudinal direction of the fiber can be measured with tensile test experiments, and the Young's modulus E_M of the fiber's matrix can be measured with AFM nanoindentation creep measurements, as illustrated in Figure 4.13. These parameters can be related to the model parameters by

$$\mu_M \approx \frac{E_M}{3} \; and \; E_R \approx E_L - E_M, \tag{15}$$

if infinitesimal strain theory and incompressibility are subjected.
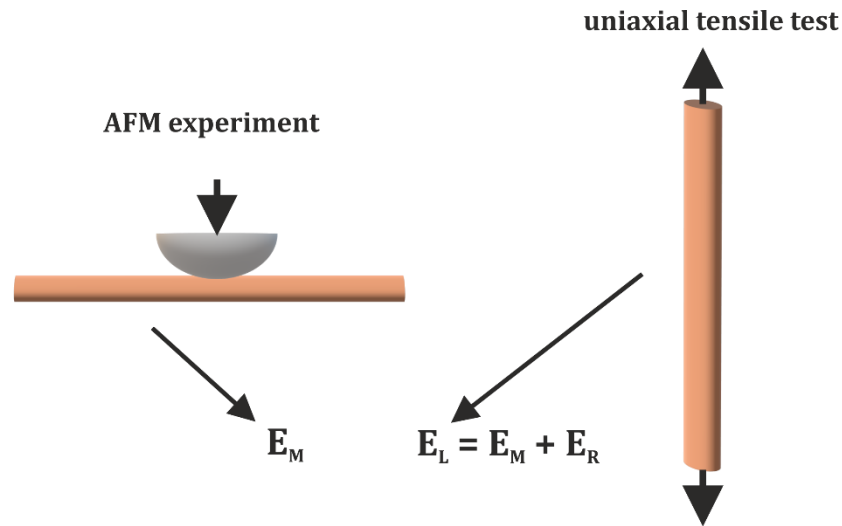
Figure 4.13: Experimental setup to evaluate the parameters of the idealized S2 fiber wall. The Young's modulus E_M of the matrix is obtained by AFM experiments. The longitudinal Young's modulus E_L is measured with uniaxial tensile tests and consists of the sum of E_M and the Young's modulus of the reinforcement (microfibrils) E_R. Adapted from [112].

In Figure 4.14, the AFM nanoindentation experiment with a spherical indenter of about 300 nm radius is illustrated. During indentation, the maximum (von Mises) stress concentration is approximately 100 nm below the surface. The soft matrix material consisting of lignin and hemicellulose deforms due to the local loading and the stiffer microfibrils move like rigid bodies.
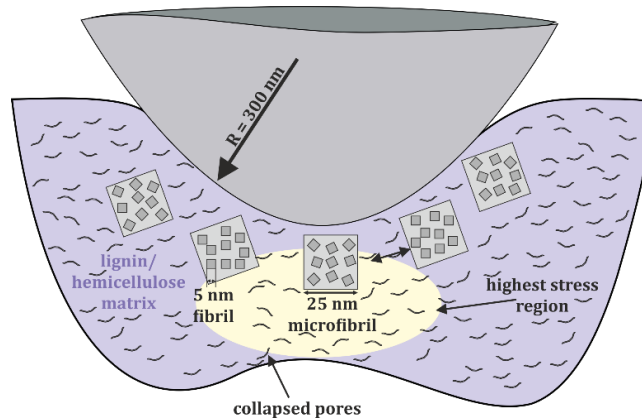
Figure 4.14: Illustration of the AFM experiment measuring the matrix properties. Microfibrils (light grey color) which are formed of elementary fibrils (dark grey color) are surrounded by the lignin/hemicellulose matrix (violet color). The soft matrix material is mainly deformed in the maximum stress region below the surface which is indicated in yellow. Adapted from [112].

The measured viscoelastic parameters of the AFM experiments are related to the stiffness of the matrix and, therefore, to the fiber's transverse elastic modulus E_M. Since the viscoelastic behavior of the matrix is fully present in all directions the material parameter μ_M can be directly extracted from Equation 15. The incorporation of the uniaxial tensile experiment is more difficult. Different relaxation times are present in the matrix and in longitudinal direction, which prevent a simple subtraction. This is further discussed in [112].

Whereas the elastic behavior reveals a higher stiffness in longitudinal than in transverse direction, the viscous behavior seems to be rather similar in magnitude in both directions. This supports the assumption that the matrix contributes in both directions. However, for the longitudinal direction, an additional relaxation mechanism has been observed which could be explained by the non-crystalline cellulose regions in the microfibril reinforcement.

In summary, a transversely isotropic model for pulp fibers that depends on two material parameters has been developed. The two parameters can be extracted from AFM experiments reported here and from macroscopic tensile testing. This model can be applied in paper network simulations or fibers in the dry state when compressibility is not so important.

4.4 Viscoelastic properties of the S2 layer of pulp fibers

One of the main goals of this work was not only the implementation of a working AFM-based technique to obtain local viscoelastic properties, but also to get more insight into the different cell wall layers of the pulp fiber. As has been mentioned before, the S2 layer – constituting to 80-95 % of the thickness – is the predominating cell wall layer and mainly responsible for the mechanical properties of the fiber. Since the S2 layer is not accessible from the surface of the fiber, an approach to measure useful and reliable data needed to be developed. Two possible routines can be chosen: First, it is known that certain enzymes attack the fiber surface and this way the S1 layer could be removed and afterward investigated [116, 117]. Here, it was decided against this approach, because the enzymatic attack is not only selectively removing the S1 layer but presumably damages the S2 layer as well. The approach chosen in this work is that a paper sheet of desired pulp fibers is embedded in a hydrogel-like material called glycol methacrylate (GMA) and cut with a microtome machine utilizing a diamond knife to 7 μm thick samples. This routine is also not straightforward and, therefore, first, a characterization of the chemical and morphological characteristics of these microtome cuts is presented before the viscoelastic properties of the S2 layer are documented and discussed.

First, a Raman analysis has been performed to investigate if GMA is penetrating the fiber cell wall. The Raman spectrum is presented in Figure 4.15. In literature, a Raman analysis of GMA has been found measured at the same laser wavelength of 633 nm [134]. Characteristic GMA modes between 800 and 900 cm^{-1} and a very pronounced mode at 1450 cm^{-1} have been used for the identification of GMA. These modes are clearly visible for the Raman measurements of GMA, but not for the spectra obtained on fibers. Here, a fiber embedded in GMA and a fiber, which has not been in contact with GMA, have been measured and show very similar spectra. In general, no significant amount of GMA in the fiber cell walls can be resolved with Raman analysis. Therefore, it can be assumed that the embedding of the fibers in GMA –to produce microtome slices – will have a negligible influence on further mechanical measurements.
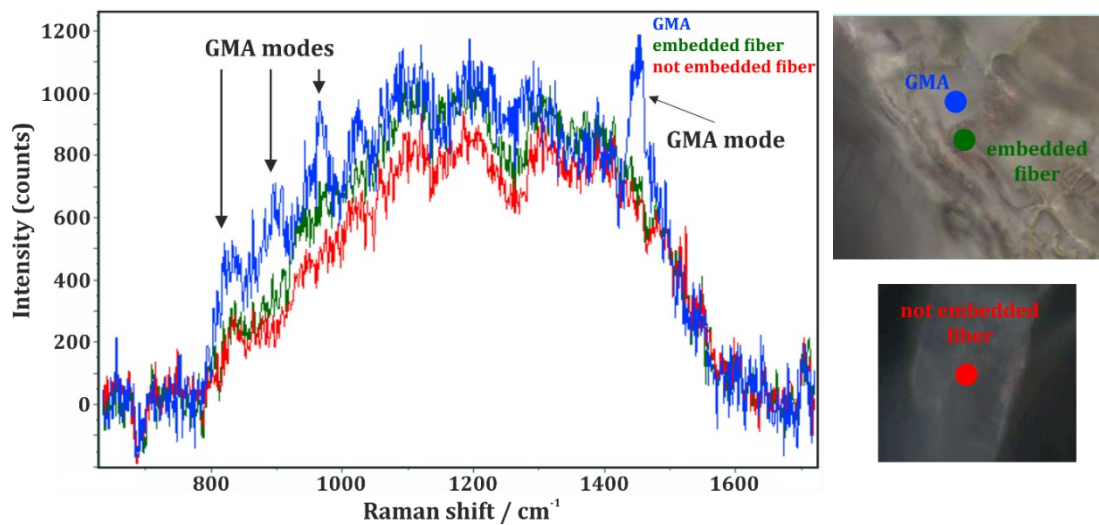
Figure 4.15: Raman spectra for GMA, an embedded pulp fiber, and a not embedded fiber, which has never been in contact with GMA. On the right side, the position of the laser spot is indicated for the different samples.

With confocal laser scanning microscopy (CLSM), the surface of the microtome cuts has been investigated to obtain larger overview images. In Figure 4.16, a CLSM image with the corresponding height image is presented. Most fibers have been cut perpendicular to the longitudinal fiber direction. Fibers that have been cut parallel to the longitudinal direction are not easily distinguishable. In Figure 4.16a, it is clearly visible that most fiber cross-sections show a collapsed lumen. The height image in Figure 4.16b indicates that the GMA is located higher than the fiber cross-sections.
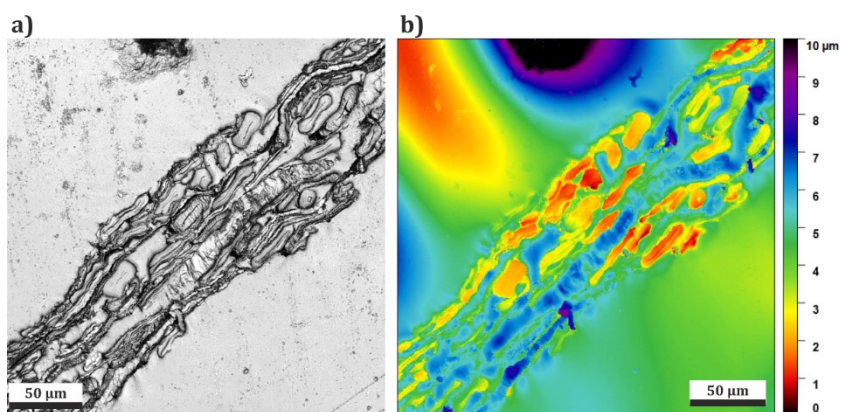
Figure 4.16 (a) CLSM overview image and (b) corresponding height image of a microtome cut.

66

Further CLSM images in Figure 4.17 and Figure 4.18 indicate the influence of the cutting procedure on the surface of the samples. In Figure 4.17b and Figure 4.18b, the white arrows indicate cross-sections of fibers that have a surface that is characterized by cracks or fractures. These cracks appear perpendicular to the cutting direction. An additional surface feature is indicated by a blue arrow in Figure 4.18b. Here, the surface of the fiber seems to corrugate due to rupturing. As there is no lumen visible, this fiber has likely been cut parallel to the longitudinal fiber direction.
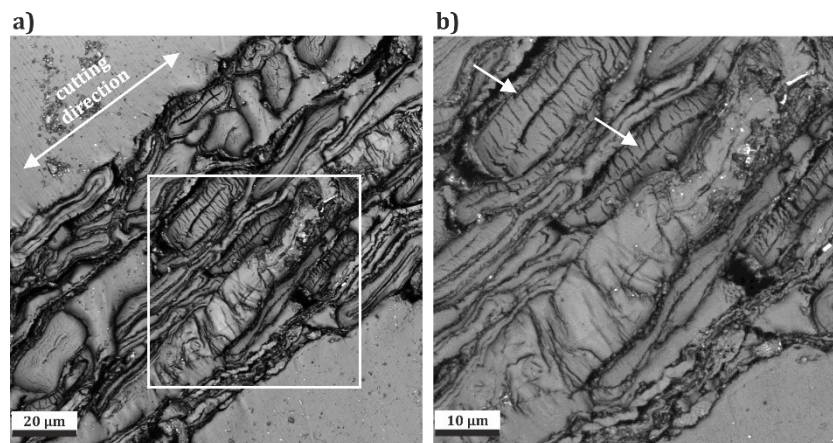
Figure 4.17: CLSM images. (a) The CLSM image shows one position on the microtome sample. The white arrow is indicating the cutting direction. The white square presents the zoom-in region of (b). In (b), the white arrows indicate fiber cross-section surfaces that are characterized by cracks.
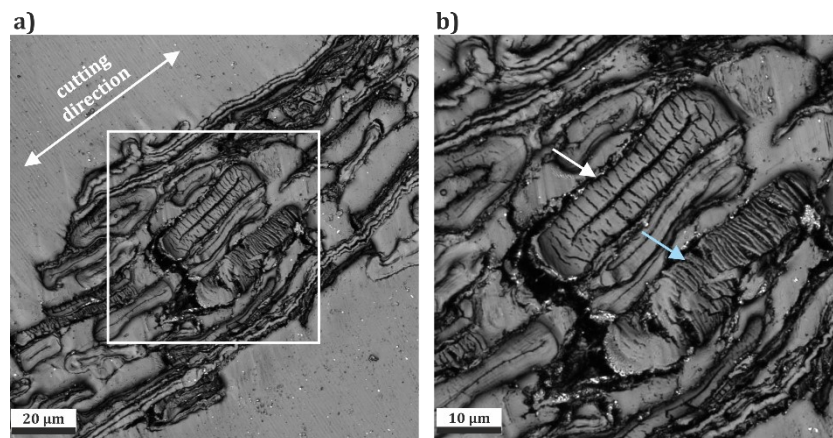
Figure 4.18: CLSM images. (a) The CLSM image shows one position on the microtome sample. The white arrow is indicating the cutting direction. The white square presents the zoom-in region of (b). In (b), the red arrow indicates a fiber cross-section surface that is characterized by cracks whereas the blue arrow indicates a fiber surface that seems ruptured and has probably been cut parallel to the longitudinal fiber direction.

The observed surface features have also been investigated with AFM. Topography images and line profiles are presented in Figure 4.19 and 4.20. In Figure 4.19a, the surface of a fiber cross-section with fractures can be seen with zoom-ins in Figure 4.19b and c. The line profile in Figure 4.19d indicates that the cracks have a width of about *100 nm* and a depth of about *50 nm*. (The values are given as mean ± standard deviation and determined from seven independent line profiles.) In the AFM scans, the direction of the cracks seems rather arbitrary in contrast to the rather parallelly ordered cracks perpendicular to the cutting direction visible in the larger CLSM images.
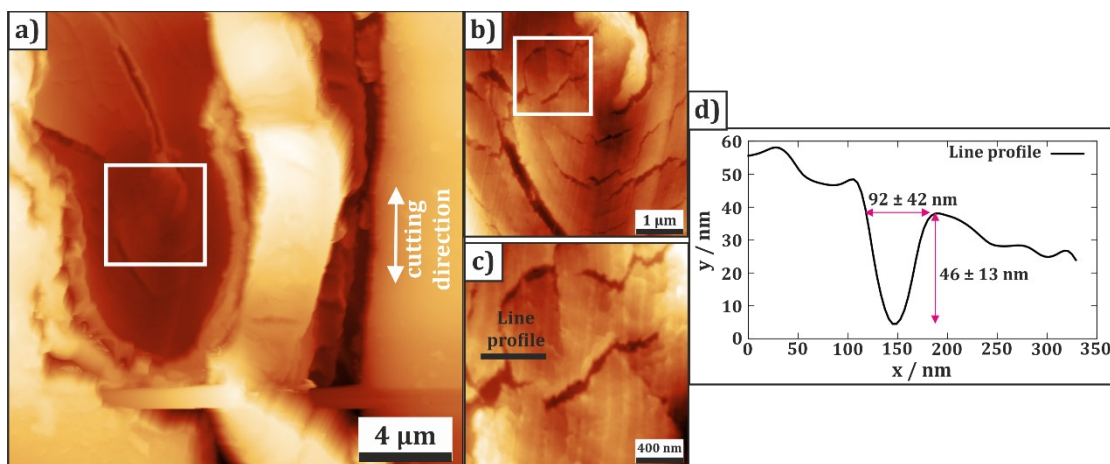
Figure 4.19: Measurement of fiber cracks due to microtome cutting. (a) 20 x 20 µm² topography image of a fiber cross-section cut perpendicular to the longitudinal fiber axis (z-scale: 4 µm). The white squares indicate the zoom-in regions. Zoom-ins: (b) 5 x 5 µm² topography image (z-scale: 650 nm) and (c) 1 x 1 µm² topography image (z-scale: 300 nm) with the corresponding line profile in (d). The values for the depth and width of the cracks are given as mean ± standard deviation.

The fiber surface investigated in Figure 4.20 has apparently been cut parallel to the longitudinal fiber direction. Here, a ruptured fiber surface is clearly visible and as has been indicated in the images, it is possible to distinguish the S1 as well as the S2 layer. It seems that due to the cutting, the S1 layer partly ripped off and exposed the S2 layer. In the zoom-in into the S2 layer in Figure 4.20c, single microfibrils can be distinguished. The width is *(40 ± 12) nm*, which is in good agreement with literature values, considering the dilation effect due to the finite size of the AFM tip. (The values are given as mean ± standard deviation and determined from five independent line profiles.)

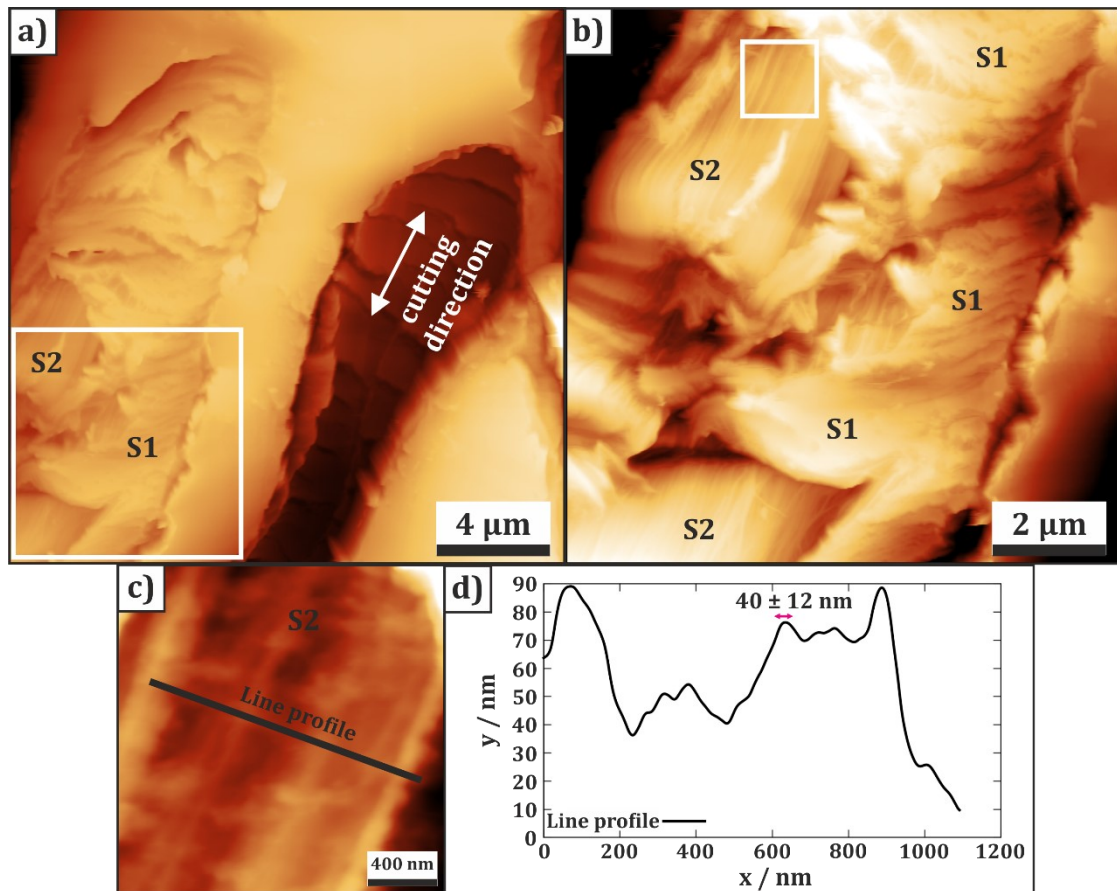68

*Figure 4.20: Measurement of the fiber surface of a transversely cut fiber. (a) 20 x 20 µm²
topography image of a fiber cross-section cut parallel to the longitudinal fiber direction (z-
scale: 5 µm). The white squares indicate the zoom-in regions. Zoom-ins: (b) 10 x 10 µm²
topography image (z-scale: 2.2 µm) exposing the S1 and S2 cell wall layer and (c) 1 x 1 µm²
topography image of the S2 layer showing an individual microfibril (z-scale: 150 nm) with
the corresponding line profile in (d). The width of the microfibrils is given as mean ± standard
deviation.*

As a first step to mechanically characterize the S2 layer, AFM-NI measurements have
been obtained with a pyramidal probe at different RH following the procedures described
in Ref. [9]. The results are presented in Figure 4.21a, b. As can be seen, both E_r and H are
decreasing with increasing RH. At 10 % and 25 % RH, the values for E_r are quite constant
but show a drop at higher RH. Compared to that, the hardness shows a continuous
decrease.

Since the embedding material is a soft hydrogel-like material, the mechanical properties
of GMA have also been investigated by AFM-NI, and the results are presented in Figure
*4.21*c, d. The values of E_r and H are always lower than for the S2 cell wall, and the material

also exhibits a dependence on RH. With increasing RH, the values drop to quite low values. Due to its hydrogel-like nature, GMA swells a lot and, therefore, measurements in water were not possible. For one, the height difference between GMA and fiber surface is increasing a lot due to the swelling of the GMA and – for the necessary large overview topography images of 50 x 50 μm² – the z-range of the AFM is exceeded. Furthermore, GMA might even swell so much that it covers the fiber surfaces which makes them inaccessible for the AFM tip.
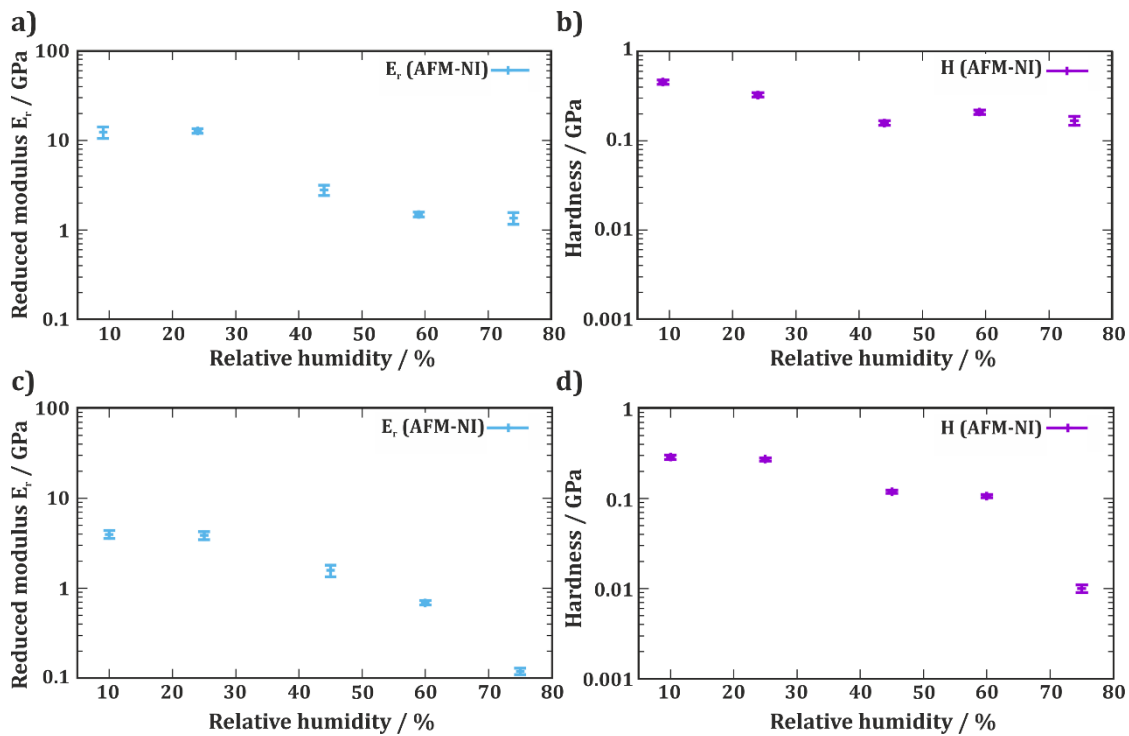
Figure 4.21: AFM-NI results for of the S2 cell wall layer of pulp fibers and the embedding material GMA with a pyramidal probe. In (a) the reduced modulus E_r and (b) the hardness H for pulp fibers at different RH is depicted. In (c) the E_r and (d) the H values for the embedding material GMA are presented at different RH.

In literature, conventional NI has been applied to the S2 wall of spruce wood tracheids [3]–[6] as well as pulp fibers [7] before. The results are summarized in Table 4. The samples have also been embedded and cut by a microtome, but all these measurements have been obtained at ambient conditions. Therefore, it is hard to compare them to the obtained results in this work. However, one trend is clear, the reduced modulus values obtained by NI are higher than for AFM-NI. Only at low RH, the values for the E_r of the S2

layer are similar to those obtained by NI on pulp fibers [7]. The hardness values of all NI measurements are in the same range as the *H* values obtained by AFM-NI at lower RH.

Table 4: Overview and comparison of different NI results for the reduced modulus E$_r$ and the hardness H on spruce tracheids and pulp fibers including information on the investigated material and the indenter geometry.

wood species	detailed information	MFA	pulping grade	probe	E$_r$ / GPa	H / MPa	Literature
spruce	earlywood (EW)	x	x		13.49 ± 5.75	254 ± 69	
spruce	transition wood (TW)	x	x	Berkovich	21.27 ± 3.12	286 ± 39	[3]
spruce	latewood (LW)	x	x		21.00 ± 3.34	335 ± 30	
spruce	compression wood (CW)	50	x	Berkovich	8.2	~450	[4]
spruce	EW/LW	0	x		17.1	~450	
spruce	developing	x	x	Berkovich	15.3/13.5	290/300	[5]
spruce	mature	x	x		17.1/17.5	380/380	
spruce	LW	3	x		15.81 ± 1.61		
spruce	LW	5	x		15.34 ± 0.4		
spruce	LW	5	x	Berkovich	17.08 ± 0.55	x	[6]
spruce	TW	7.5	x		13.46 ± 0.30		
spruce	TW	7	x		17.54 ± 0.37		
eucalyptus		x	unbleached(κ=13)		12.2 ± 1.6	420 ± 50	
eucalyptus	pulp	x	bleached(κ=1.5)	cube corner	10.5 ± 2.1	377 ± 33	[7]
pine		x	unbleached(κ=29)		9.1 ± 1.6	430 ± 50	
pine		x	bleached(κ<1)		10.5 ± 2.1	377 ± 33	

Next, the viscoelastic behavior was tested at the same RH range (10 % - 75 % RH) with a hemispherical probe. In the first experimental series, the same load schedule as for the transverse properties of the S1 layer (5 μN) has been applied for the viscoelastic load. This leads, however, to very small deformations, which are clearly influenced by thermal drift and signal noise as can be seen in Figure 4.22. The increase in indentation depth from 25 % RH to 75 % RH is only about 5 nm and since usually signal noise of up 2 nm is common during the experiments, the interpretation of these results is quite uncertain.
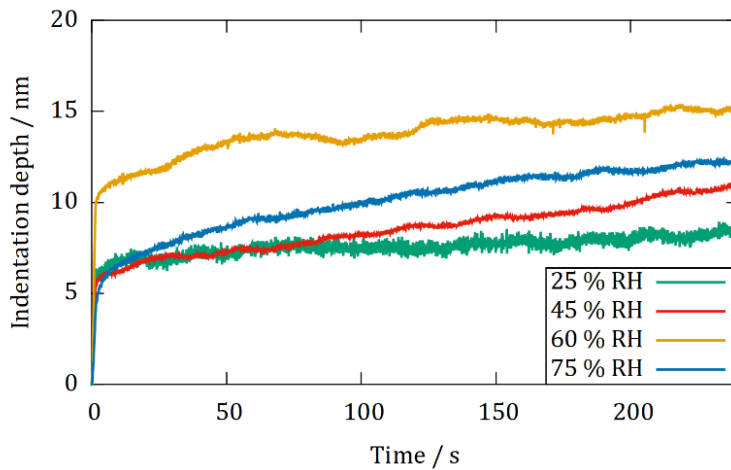
Figure 4.22: Experimental indentation depth curves of the S2 wall layer of pulp fibers for all RH values obtained with an applied load of 5 μN. At all RH values, the indentation depth is clearly < 20 nm.

Applying a higher load of 10 μN with a load rate of 6.4 μN/s resulted in more stable curves with higher deformations. In Figure 4.23, the curves at 5 μN and 10 μN are compared. Whereas the indentation curves with the lower applied load show a maximum indentation depth < 20 nm for all RH and no clear correlation with RH, the curves with the higher load reveal a distinct dependence of the indentation depth on the RH value: With increasing RH, the indentation depth is also increasing, which was already found for the transverse direction as well.
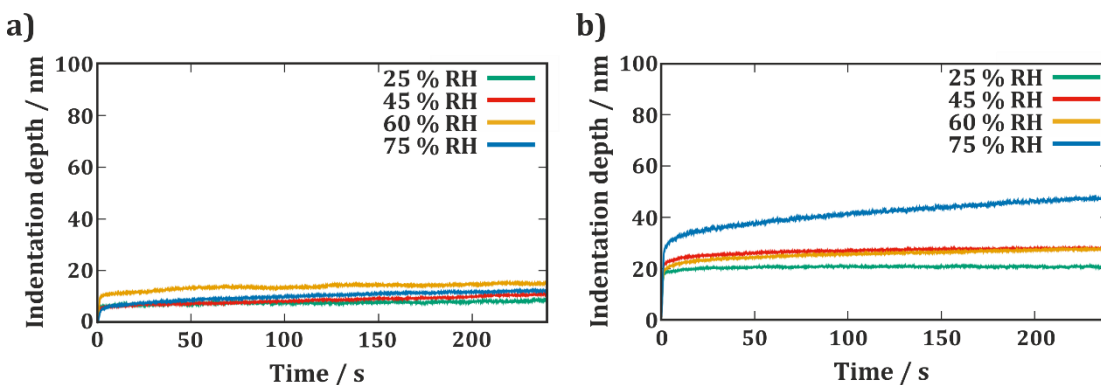
Figure 4.23: Comparison of the experimental curves for the S2 wall layer of pulp fibers at all RH obtained with an applied load of (a) 5 μN, and (b) 10 μN.

For the fitting procedure of the obtained experimental data, only the GM3 model with three relaxation times – which has already been applied to the water measurements of the S1 layer – resulted in sufficient fitting quality. Here, the relaxation times $\tau_1 = 1\ s$, $\tau_2 = 15\ s$, and $\tau_3 = 240\ s$ are a good match by the fitting algorithm. In Figure 4.24, the resulting elastic and viscous parameters are presented for the whole RH range. Whereas the elastic moduli show a decreasing trend with increasing RH, the decrease for the viscous parameters is only slightly visible at best, with η_3 even increasing.
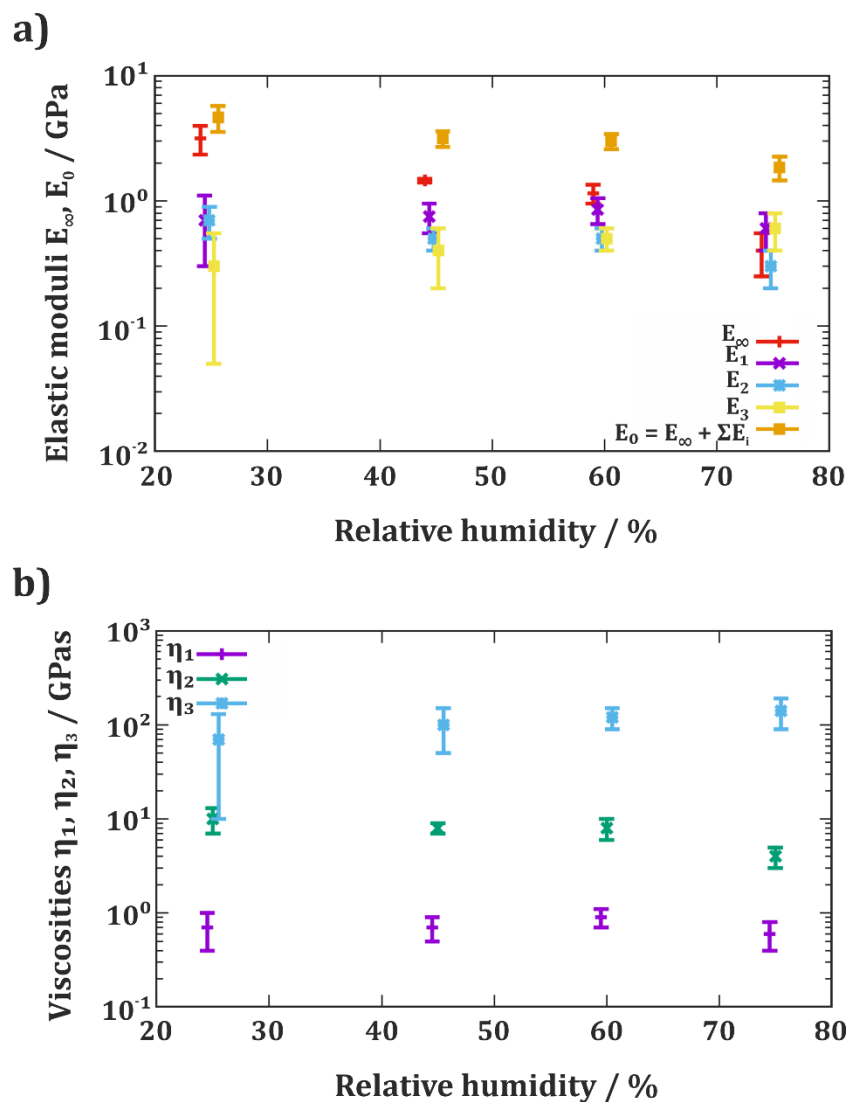
Figure 4.24: Results obtained with the GM3 model for the viscoelastic properties of the S2 cell wall layer of pulp fibers. In (a), the results for the elastic moduli E_∞ and E_0 are presented and in (b), the viscous parameters η_1, η_2, and η_3 are shown.

It is known that the tip geometry influences the results [135] in NI and the same has been found for AFM-NI [85]. Since the AFM-NI and the viscoelastic experiments have been obtained with different probe geometries and at different load rates, the influence of these effects has been further studied.

Here, the difference between varying load rates (*5*, *10*, and *20 μN/s*) has been investigated at two different RH (60 % and 75 % RH) with the hemispherical and pyramidal probe. The results are presented in Figure 4.25, and the mean value of the maximum load rate (*20 μN/s*) has been used to normalize the data. In Figure 4.25a, the load rates have been varied at 60 % RH, and an increase with increasing load rate is observed. The same trend is visible for measurements at 75 % RH presented in Figure *4.25*b, though not as pronounced as for 60 % RH. For the hardness, the opposite trend can be observed: Increasing load rate leads to decreasing hardness values, as can be seen for 60 % RH in Figure 4.25c and for 75 % RH in Figure 4.25d. Considering viscoelasticity, it is reasonable that an increasing load rate results in higher stiffness. However, the apparent lower hardness values for increasing load rates are not so easy to comprehend. Here, one needs to consider that hardness is defined by the maximum force divided by the indenter's projected area $A(z)$ according to Eq. 6. Since the maximum force is constant, $A(z)$ is smaller for lower loading rates, resulting in higher hardness values. As has been described earlier, the load schedule consists of a loading part, a hold time of 10 s, and an unloading part. At low loading rates – for 5 μN/s it takes 4 s to reach maximum force – the slow load time, in the beginning, leads to less viscoelastic effects during the holding time, resulting in a lower maximum indentation depth and, therefore, a lower $A(z)$.
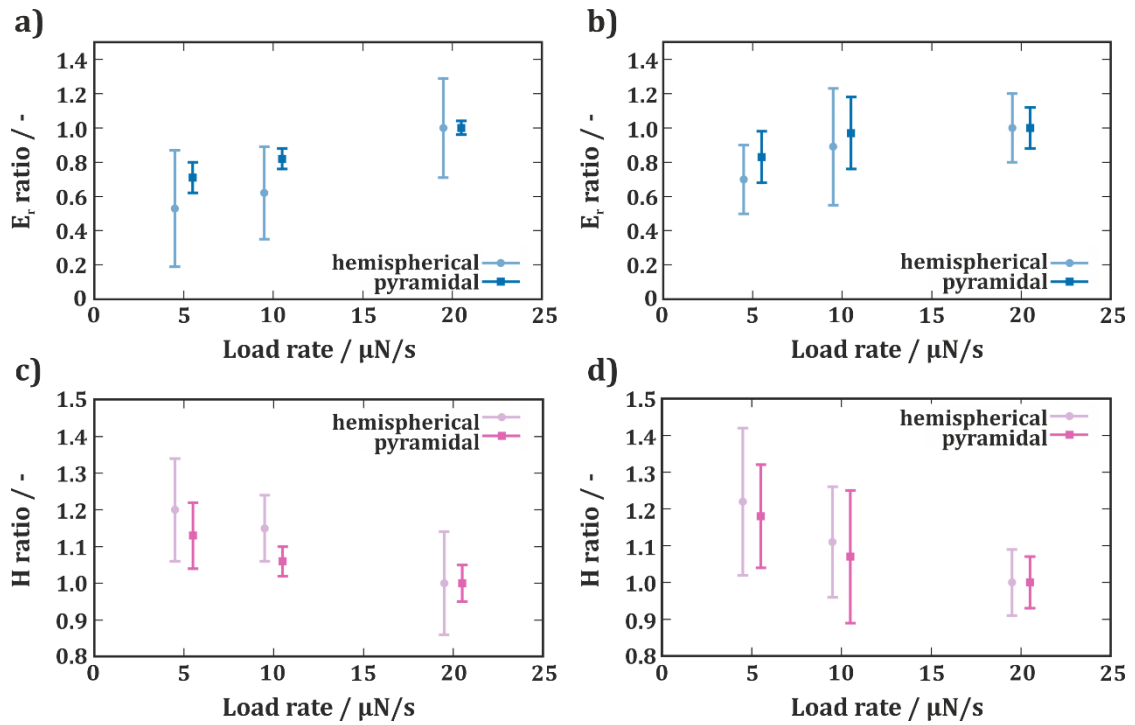
74

Figure 4.25: Normalized reduced modulus E_r and hardness H for the S2 cell wall layer of pulp fibers depending on the load rate for both, hemispherical and pyramidal indenters at (a, c) 60 % RH and (b, d) 75 % RH. The mean value of the maximum load rate was used to normalize the values.

In this work, the viscoelasticity of pulp fibers has been studied on the S1 layer surface of the pulp fiber in transverse direction and on microtome cross-sections of the S2 layer in longitudinal direction. For the transverse measurements, it was found that the GM2 model fits the experimental creep curves over the range of 10 % to 75 % RH very well, whereas for the longitudinal direction an additional Maxwell element is needed and, therefore, a GM3 model was applied to the data.

To compare the data of the transverse and longitudinal direction, the data measured in transverse direction has been re-evaluated using the GM3 model with the same relaxation times (τ_1 = 1 s, τ_2 = 15 s, and τ_3 = 240 s) as for the longitudinal direction.

In Figure 4.26, the results for the elastic moduli E_∞ and E_0 as well as for the viscosities η_1, η_2, and η_3 of both directions – longitudinal and transversal – are presented. As can be seen in Figure 4.26a, both elastic moduli in longitudinal direction have higher values than in the transverse direction. Whereas E_0 is quite similar for both directions, the E_∞ values show a larger difference between the directions up to 60 % RH. For the viscosities in

Figure 4.26b, only slight differences between both directions can be found. Overall, the viscosities are in the same range and stay quite constant over the whole RH range. Only at 75 % RH, η_1 and η_3 show higher values for the longitudinal direction. Comparing only the values of η_3 in Figure 4.26b, one can observe a slightly different trend with RH. Whereas η_3 in transverse direction is decreasing with increasing RH, η_3 in longitudinal direction is increasing.
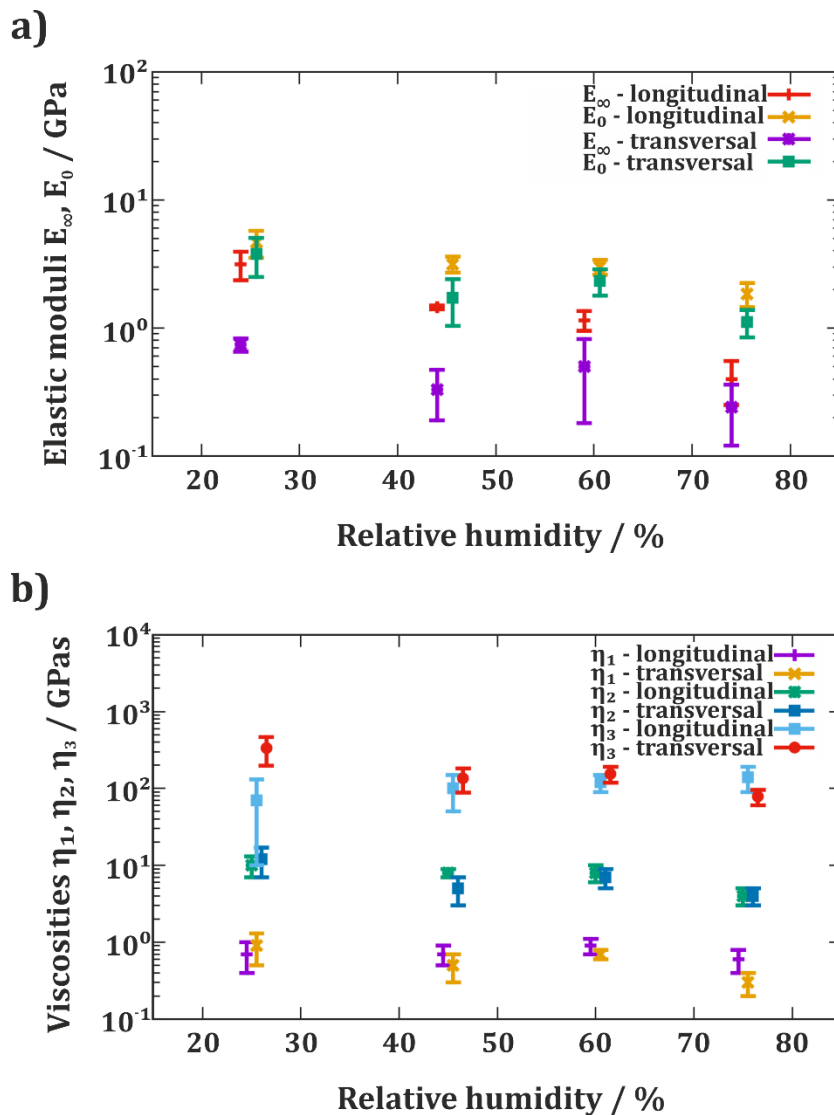

Figure 4.26: GM3 results for the viscoelastic properties of pulp fibers in longitudinal and transversal direction. (a) Elastic moduli (E_∞, E_0) and (b) viscosities (η_1, η_2, and η_3) in longitudinal and transversal direction.

76

In summary, the differences between longitudinal and transverse directions are surprisingly small. To obtain an additional visualization, the spectral representation which has been introduced in one of the parameter studies in section 3.2.5 is applied to the data of the GM3 model for the longitudinal and transverse directions. Since the relaxation times are $\tau_1 = 1\ s$, $\tau_2 = 15\ s$, and $\tau_3 = 240\ s$, the corresponding frequencies are the inverse values of the relaxation time. Thus, a frequency range between 0.001 and 10 rad/s has been chosen for a complete visualization.

Figure 4.27 to Figure 4.29 present the spectra for the storage modulus $E'(\omega)$ (a measure for the elastic response), the loss modulus $E''(\omega)$ (a measure for the viscous response), and the loss tangent $tan\delta(\omega)$ for the GM3 results at different RH in longitudinal and transverse directions.

In Figure 4.27, both directions show that the storage modulus is decreasing with increasing RH. Overall, the values for the storage modulus in longitudinal direction are higher than in transverse direction.
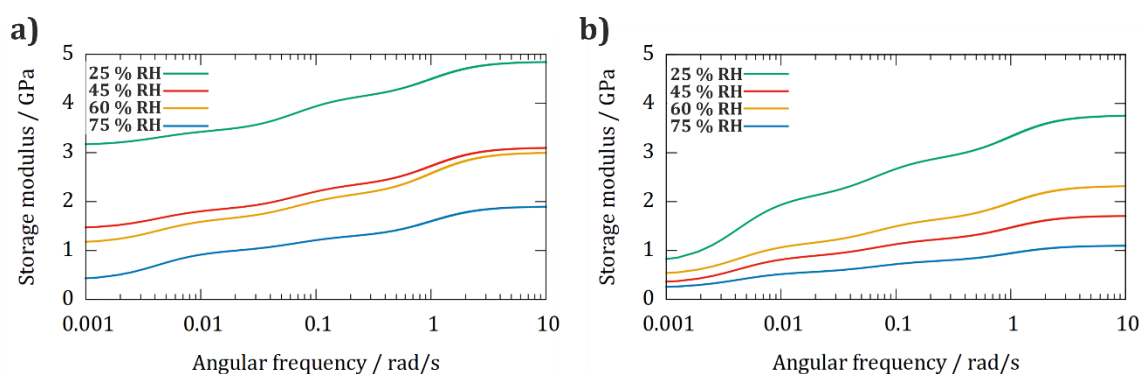

Figure 4.27: Spectra of the storage modulus E'(ω) for (a) the longitudinal and (b) the transverse direction for the different RH values.

Figure 4.28 presents the results for the loss modulus. In longitudinal direction, the values show little change. With increasing RH, the peaks corresponding to $\tau_1 = 1\ s$ and $\tau_2 = 15\ s$ are slightly decreasing whereas the peak corresponding to $\tau_3 = 240\ s$ is slightly increasing. For the transverse direction, a clear decrease of all three peaks with increasing RH is visible.
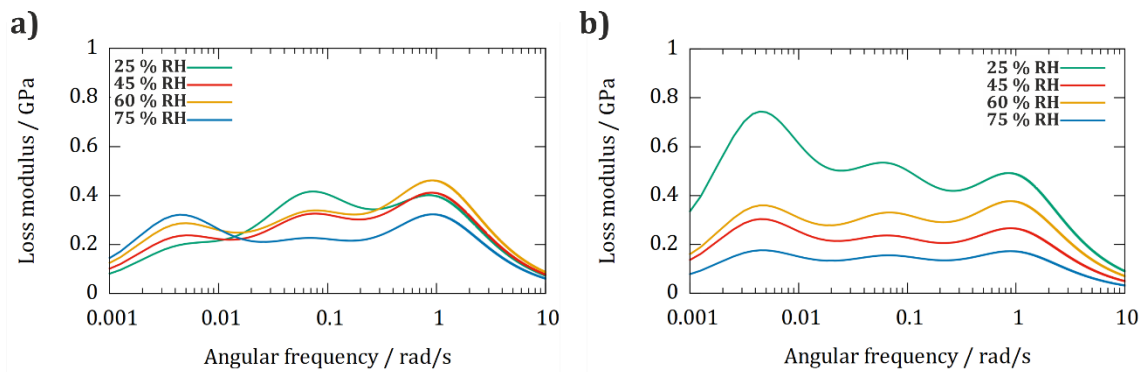
Figure 4.28: Spectra of the loss modulus E''(ω) for (a) the longitudinal and (b) the transverse direction for the different RH values.

Considering the spectra of the loss tangent, presented in Figure 4.29, three peaks for each relaxation time are visible again. However, these peaks are not as pronounced as for the loss modulus. The longitudinal direction exhibits a slight increase with increasing RH. Until 60 % RH, the values stay below 0.2. However, the peak in the spectrum that is corresponding to $\tau_3 = 240\,s$ shows a clear increase with RH and is pronounced at 75 % RH. In transverse direction, the values for the loss tangent are larger and quite constant at all RH. Again, only the peak corresponding to $\tau_3 = 240\,s$ exhibits a decrease with increasing RH. Taking a closer look, a similarity between the spectrum of 75 % RH in longitudinal direction and the transverse direction can be recognized.
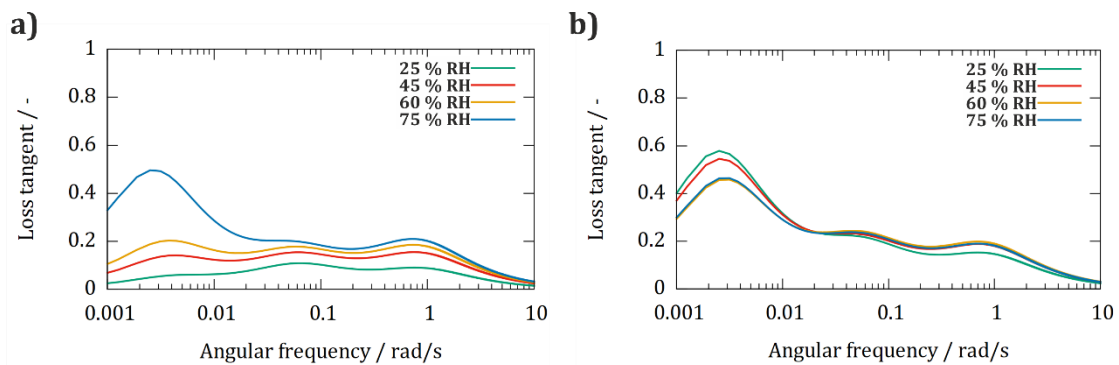

Figure 4.29: Spectra of the loss tangent tanδ(ω) for (a) the longitudinal and (b) the transverse direction for the different RH values.

A comparison of the curves for the loss tangent of both directions at 25 % RH and 75 % RH in Figure 4.30 shows this trend more clearly. At 25 % RH, there is a clear difference between the spectra. At 75 % RH, however, the spectra are nearly identical. This

78

indicates that at 75 % RH the damping behavior of the longitudinal direction is quite similar to the behavior of the transverse direction, at all RH.
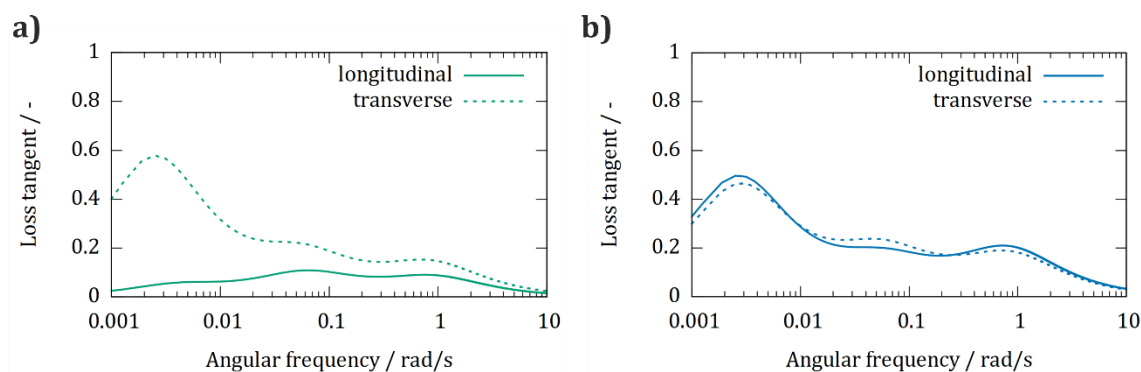
a)

b)

Figure 4.30: Spectra of the loss tangent tanδ(ω) for both directions at (a) 25 % RH, and (b) at 75 % RH.

The viscoelastic characterization of the S2 layer revealed that higher forces compared to the transverse direction are needed to obtain reliable experimental curves which are not influenced by signal noise and thermal drift. Furthermore, only the GM3 model results in a sufficient fitting of the curves. The results demonstrate that with increasing RH, the elastic and viscous parameters are decreasing as has been found for the transverse direction before.

Comparing the results of the transverse direction with the results of the S2 layer in the longitudinal direction reveals only marginal differences. Some of the elastic and viscous parameters have lower values for the transverse direction, but overall, the difference is – surprisingly – smaller than expected.

By additionally using a spectral representation of the data in both directions, an overview of the data in the frequency range of the experimental window – which is also reflected in the relaxation times – is given. Here, the storage modulus shows higher values at all RH for the longitudinal direction. The loss modulus shows a clear decrease with increasing RH for the transverse direction, whereas for the longitudinal direction the peaks corresponding to the fast relaxation times are decreasing and the third one corresponding to the slow relaxation time is increasing. The loss tangent shows the lowest values (<0.2) for the longitudinal direction between 25 % RH and 60 % RH. At 75 % RH, however, the spectrum is nearly identical to the transverse direction. Overall, the spectra for the transverse direction barely change with humidity.

4.5 Hygroscopic properties of cellulose films

The hygroscopic behavior of cellulosic materials and its influence on mechanical properties is a topic of research. An idea based on previous experiments with cantilevers coated with porous silica layers [94],[95] inspired the following experiments. A tipless cantilever was coated with a thin cellulose film. Here, two methods of coating have been tested, which have been described in the experimental section (chapter 3.1.4).

In Figure 4.31, an experiment with a coated cantilever is presented which has been obtained by Christian Ganser. An increase in RH results in a positive increase of the deflection of the cantilever due to the swelling of the cellulose film. The cantilever is bending upwards. For decreasing RH, this effect is reversed. The cellulose film shrinks and bends the cantilever downwards.
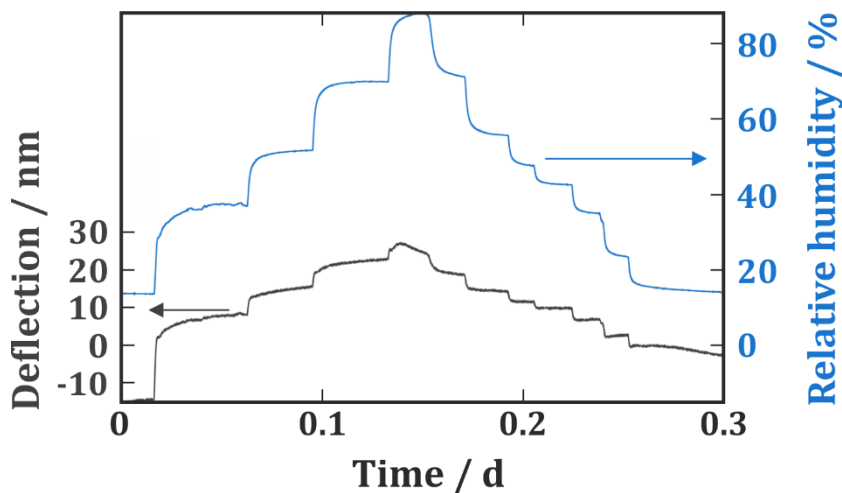

Figure 4.31: Deflection and RH against time plot for a cantilever with a manually deposited cellulose film coating. The black line indicates the deflection of the cantilever, whereas the blue line depicts the RH.

Interestingly, the deflection curve is not fully reversible after a full RH circle. One possible explanation was that the humidity steps have not been at equilibrium, i. e., the changes have been applied too fast.

Thus, the experiment has been repeated by the candidate with longer equilibration times. The results for one example are presented in Figure 4.32. Here, RH has been increased in three steps. The first two steps are still quite short and show similar results

like in Figure 4.31. With increasing RH, the deflection of the cantilever is increasing as well. Step three, on the other hand, has a long holding time and shows, in the beginning, the same increasing cantilever deflection, but after a maximum is reached, the deflection is decreasing again although the RH value stays quite constant. This behavior is reproducible for both deposition techniques of the cellulose film.
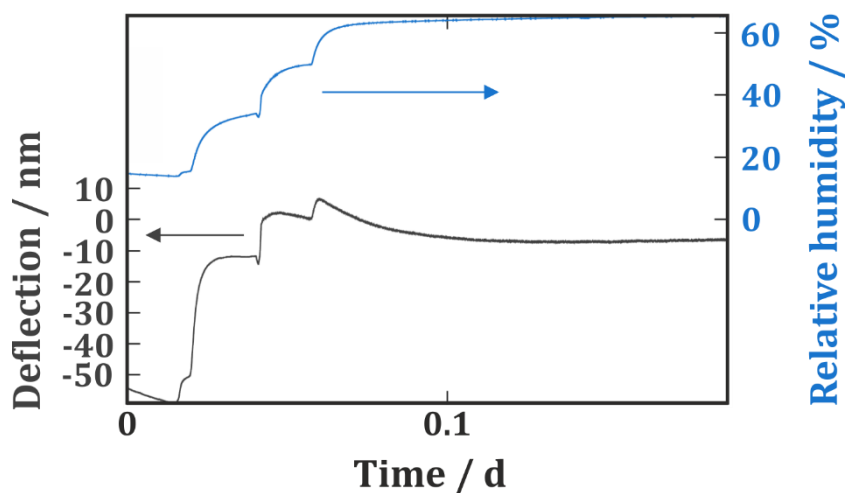

Figure 4.32: Deflection and RH against time plot for a cantilever coated with a cellulose film by manual deposition.

Finally, a cantilever without any coating was tested by the same procedure to make sure that other influences can be neglected. In Figure 4.33, the results of an experiment with an uncoated, pure silicon cantilever are presented. It reveals the same long-time effect as seen with the cellulose film coating. The effect of the change in RH is even larger than for a cantilever with cellulose film coating, which is very unintuitive. Apparently, the moisture is interacting with the cantilever more strongly than expected. One possibility to eliminate this effect would be to coat the cantilever first with a hydrophobic coating if in the future somebody will follow up on this idea.
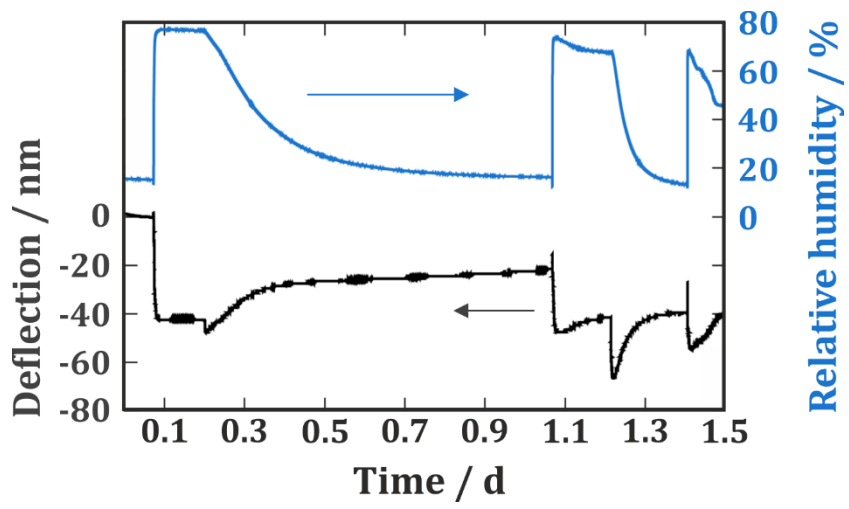
Figure 4.33: Deflection and RH against time plot for an uncoated cantilever.

4.6   Frictional properties of cellulose blend films

The results reported in this chapter have also been obtained in the framework of the CD Laboratory for Fiber Swelling and Paper Performance as a consequence of a side topic in collaboration with S. Spirk (Institute of Bioproducts and Paper Technology, TU Graz) and T. Nypelö (Division of Applied Chemistry, Department of Chemistry and Chemical Engineering, Chalmers University, Gothenburg, Sweden). The synthesis of the films has been done by G. Teichert in Graz and Gothenburg. The original goal of this study was to see if by blending cellulose with a cellulose derivative at different ratios, a tribological synergy can be found [136]. Cellulose derivate phase separation in thin films was applied to generate patterned films with distinct surface morphology. Two cellulose derivatives were transformed into two-phase blend films with one phase comprising trimethylsilyl cellulose (TMSC) regenerated to cellulose with hydroxyl groups exposed to the film surface. Adjusting the volume fraction of the spin coating solution resulted in variation of the surface fraction with the other, hydroxypropyl cellulose stearate (HPCE) phase. Large parts of chapter 4.6 have already been published in [41].

To study frictional properties of blend films of cellulose derivatives, pure TMSC and HPCE film and blend films containing both derivatives with three composition ratios, 3:1, 1:1, and 1:3 were spin coated. Furthermore, the TMSC domains have been regenerated to cellulose. In Figure 4.34 and Figure 4.35, the surface morphology of the pure TMSC, cellulose and HPCE films as well as the blend films are presented. To quantify the observed surface features for the individual blend films, ten individual cross-sections of the features were obtained from the topography images. The Gwyddion software was utilized to determine the height and width of the features for each film. The values are given as mean ± standard deviation.

The TMSC:HPCE blend films (Figure 4.34) are characterized by domains on the surface which formed either cavities (TMSC:HPCE 3:1) or protrusions at the lower sub-micrometer scale. Protrusions with a height of *(35 ± 10) nm* and a width of *(780 ± 130) nm* were determined for TMSC:HPCE 1:1. For TMSC:HPCE 1:3 films, a height of *(55 ± 10) nm* and width of *(340 ± 50) nm* was determined. It seems that the protrusions increased in height with increasing HPCE content but decreased in lateral size.
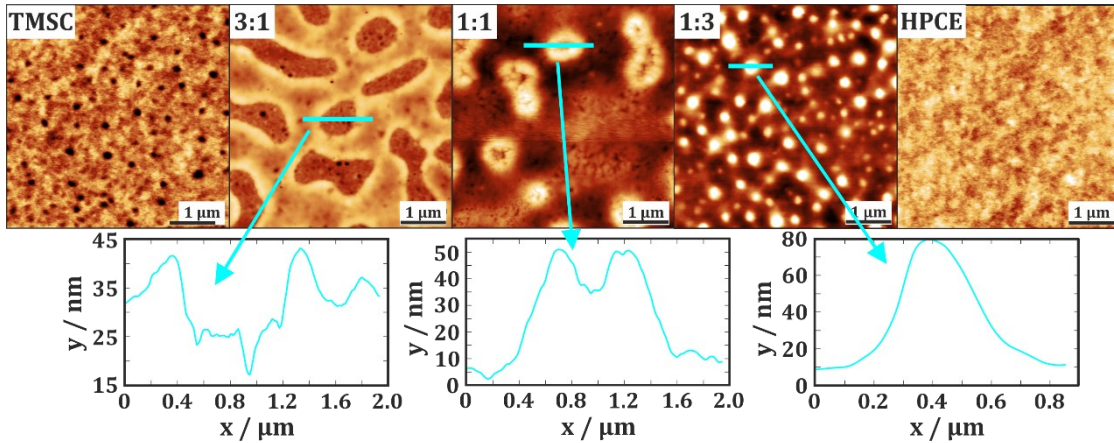
Figure 4.34: 5 x 5 μm² AFM topography images of TMSC:HPCE with corresponding line profiles of the surface features. The z-scale for the pure films is 10 nm and for all the blend films 60 nm. The height is increasing with increasing brightness. After [41].

The regeneration of TMSC into cellulose results in the densification of the film and a reduction in film thickness of the regenerated domains (Figure 4.35). HPCE is unaffected by the treatment. Therefore, the regeneration of the cellulose resulted in an inverted morphology compared to the TMSC:HPCE blend films which can be seen by comparing Figure 4.34 and Figure 4.35. Again, the dominating surface features are protrusions and cavities. On the cellulose:HPCE 3:1 surface, protrusions with arbitrary size and a height of (40 ± 10) nm are visible, whereas the cellulose:HPCE 1:1 and 1:3 films are characterized by cavities which decrease in lateral size. While the 1:1 sample shows random-shaped surface features with a lateral width of *(660 ± 80) nm*, the 1:3 blend film surface exhibits more spherical-shaped features with a width of only *(250 ± 25) nm*.

To further characterize the surface, a roughness analysis for all the 5 x 5 μm² topography images was performed according to [137]. The values for the RMS roughness σ and the lateral correlation length ξ of the blend films prior (TMSC:HPCE) and after (cellulose:HPCE) regeneration are presented in Table 5. The RMS roughness of the resulting blend films increased by factors of 4 to 20 compared to the pure films. TMSC, cellulose, and HPCE have an RMS value of *1.5 nm*, *1.5 nm*, and *1.1 nm*, respectively. For the TMSC:HPCE blend films, the 1:3 composition featured the largest RMS value with *14.2 nm* while after regeneration by HCl vapors, the cellulose:HPCE 3:1 film exhibited the largest RMS value with *19.8 nm* overall. In Figure 4.37a, the RMS roughness values are plotted and compared. The lateral correlation length has the lowest values for the pure films. For the TMSC:HPCE blend films, the 1:1 composition has the largest ξ value whereas for the

cellulose:HPCE blend films, the 3:1 composition featured the largest ξ value. Overall, the value increased by a factor of about three compared to the pure TMSC and HPCE films. Compared to the pure cellulose film, it is even a factor of about six.
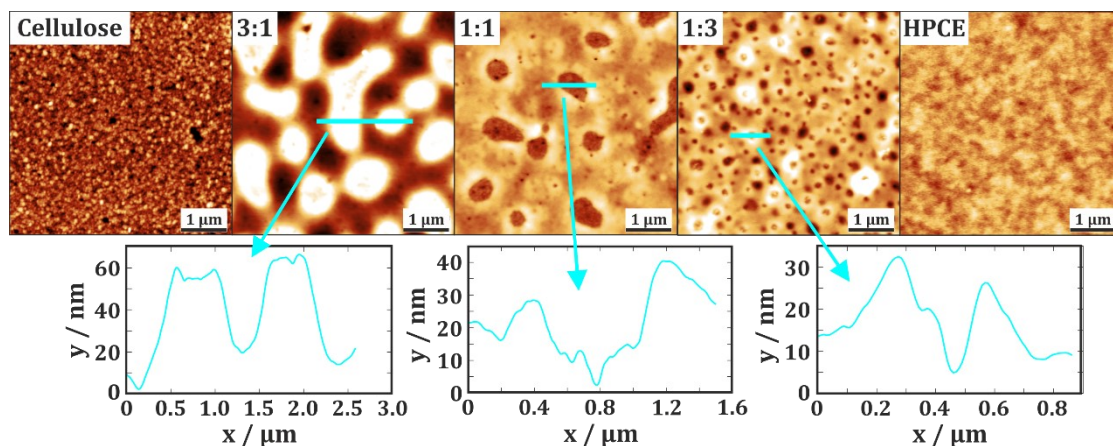

Figure 4.35: 5 x 5 µm² AFM topography images of cellulose:HPCE blend films with the corresponding line profiles of the surface features. The z-scale for the pure films is 10 nm and for all the blend films 60 nm. The height is increasing with increasing brightness. After [41].

By treating the cellulose:HPCE films with chloroform, it is possible to remove the HPCE phase and so identify the cellulose phases on the films. The TMSC:HPCE 3:1 blend film consisted of a continuous TMSC matrix with HPCE cavities. Regeneration of the TMSC to cellulose resulted in a shrinkage of the TMSC domains. Therefore, the HPCE domains were protruding from the surface of the cellulose:HPCE blend films. With increasing HPCE amount, the matrix increasingly consisted of HPCE, and the TMSC domains formed protrusions, which collapsed during cellulose regeneration.

Table 5: Roughness analysis of 5 x 5 μm² images. RMS roughness σ and lateral correlation length ξ of the roughness of the blend films prior (TMSC:HPCE) and after (cellulose:HPCE) regeneration. After [41].

Blend films	RMS roughness σ / nm	Lateral correlation length ξ / nm
TMSC	1.50 ± 0.05	95 ± 5
TMSC:HPCE 3:1	7.60 ± 0.30	185 ± 15
TMSC:HPCE 1:1	12.60 ± 0.80	320 ± 20
TMSC:HPCE 1:3	14.15 ± 0.75	145 ± 10
HPCE	1.10 ± 0.05	120 ± 10
Cellulose	1.50 ± 0.20	55 ± 10
Cellulose:HPCE 3:1	19.80 ± 0.30	310 ± 10
Cellulose:HPCE 1:1	8.00 ± 0.40	180 ± 5
Cellulose:HPCE 1:3	10.20 ± 0.10	155 ± 5
HPCE	1.10 ± 0.10	140 ± 10

The contact mode FFM images are presented in Figure 4.36 and indicate a difference between the friction of the neat and the cellulose/HPCE blend films. The pure films show a rather uniform friction signal, whereas TMSC:HPCE and cellulose:HPCE blend films indicate a material contrast, though it is rather weak. It should be mentioned that measurements in contact mode on polymer films are not straightforward. To not destroy the delicate surface, applied forces on the AFM probe need to be rather low. Furthermore, on polymer surfaces, the AFM tip can easily pick up debris, which would also alter the obtained signal. For the TMSC:HPCE 1:3 sample (Figure 4.36a), it can be clearly seen that the probe is strongly interacting with the surface. As presented in Figure 4.34, the surface of the TMSC:HPCE 1:3 blend film is characterized by protrusions which are about 250 nm in width. These protrusions are not clearly visible in the friction image anymore. Here, it is most likely that the probe is damaging the soft surface.
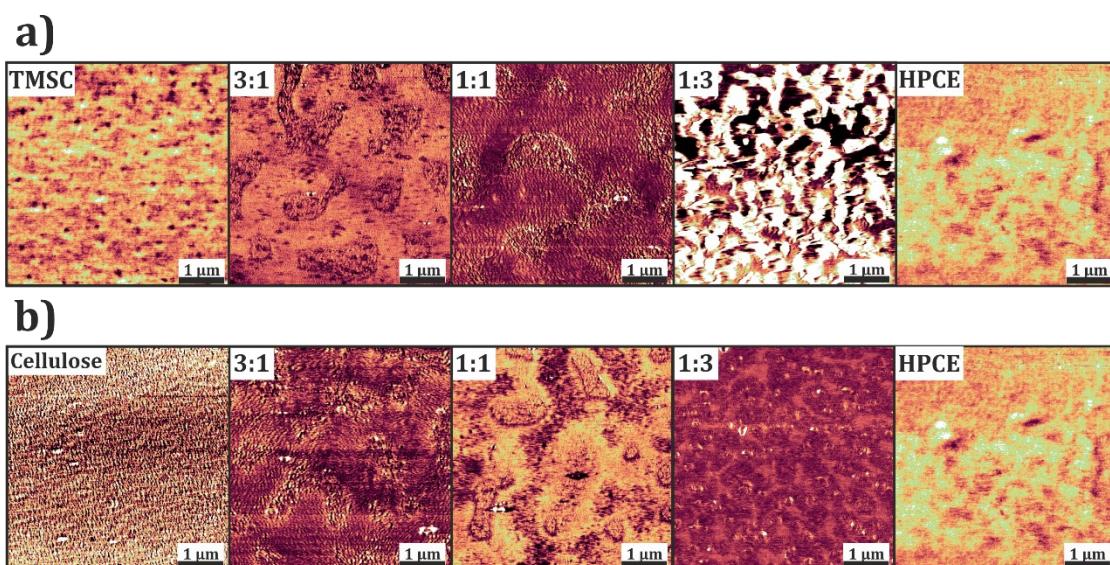
a)

b)

Figure 4.36: 5 x 5 μm² AFM contact mode friction force images of the (a) cellulose:HPCE, and (b) TMSC:HPCE blend films. The z-scale of all images is 5 mV. Adapted from [41].

In Figure 4.37, all the results of the morphological and mechanical characterization are summarized. The results for the RMS roughness (Figure 4.37a) have already been discussed. The adhesion force (Figure 4.37b) and the elastic modulus (Figure 4.37c) have been obtained by force mapping, as is explained in chapter 2.7. For the elastic modulus, the approach curve has been fitted with the Hertz model (chapter 2.5). Here, it should be noted that the calculated elastic modulus is describing the surface of the films and should be understood as an estimation, rather than an exact value for the bulk material of the films. The adhesion force values of the blend films are lower (*20-50 nN*) than the values of the pure TMSC/cellulose and HPCE films with about *65 nN*, and *105 nN*, respectively. Similar results are obtained for the elastic modulus. For the pure cellulose film, the values are highest and close to *20 GPa*. Also, HPCE shows higher elastic modulus values than the blend films. Only the TMSC film is in the same range as the blend films. Here, it should be considered that the films have been spin coated on silicon substrates and vary in thickness between *40–140 nm*. The thicknesses have been determined by profilometry [41]. After regeneration, the cellulose film is quite thin with a thickness of about *40 nm*, the thinnest film of all the samples, whereas the pure TMSC and HPCE films both have a thickness of about *100 nm*. Therefore, it is likely that the obtained results for the elastic modulus are influenced by the substrate. With AFM-NI it was found that the reduced modulus E_r of cellulose films under ambient conditions was *6.3 ± 1.0 GPa* [8]. In general, it can be stated

that the blend films are much softer than cellulose and HPCE. The average friction coefficients (Figure 4.37d) were lower for the blend films than for the pure films. It should be noted here that friction force data is in good agreement with those reported for cellulose spheres interacting with modified silica surfaces in a similar applied force range (~*5 nN*) [138].
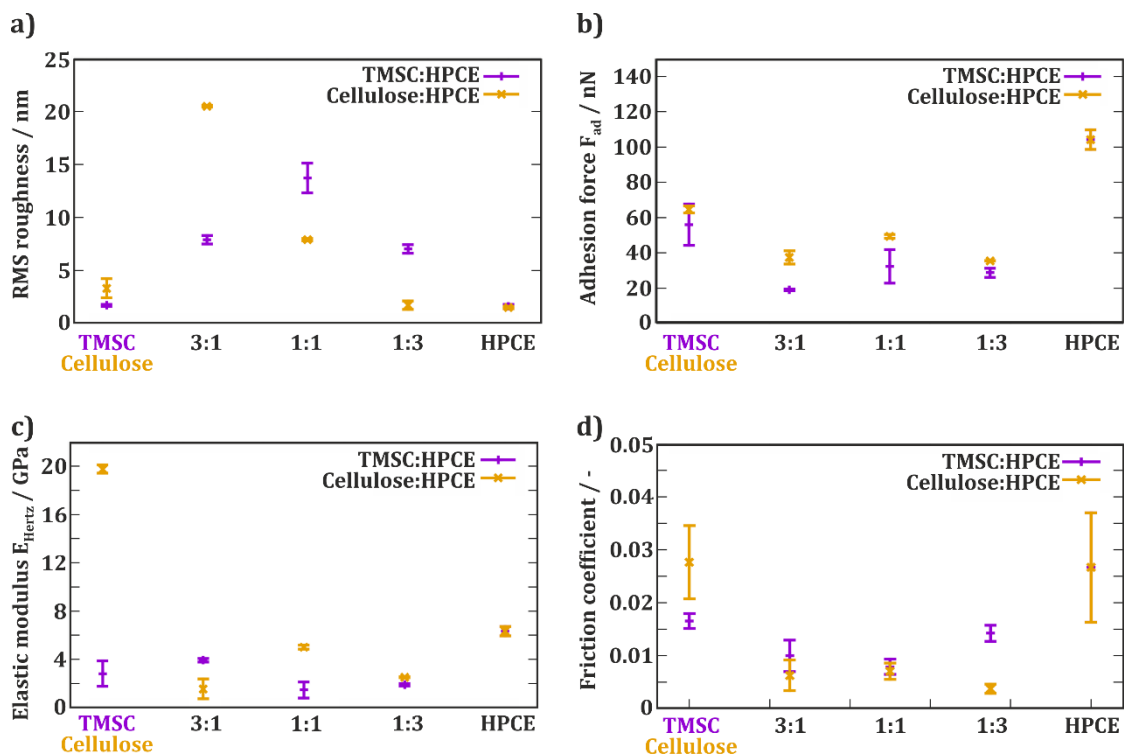

Figure 4.37: (a) RMS roughness, (b) adhesion force, (c) elastic modulus, and (d) friction coefficient for cellulose:HPCE and TMSC:HPCE blend films. Adapted from [41].

The morphology and frictional properties of two different series of blend films, Cellulose:HPCE and TMSC:HPCE, have been studied. Phase separation and regeneration influenced the surface morphology and resulted in a roughness variation of the blend films between *1.1 nm* and *19.8 nm*. The friction data corresponded well to additional adhesion measurements and showed lower values for the blend films compared to the pure films. This indicates that the friction coefficient of the films can be tuned by varying the composition.

The study also demonstrated the applicability of FFM to obtain – at least semi-quantitatively – mechanical parameters of cellulose-based polymer blend films.

5   Conclusions & Outlook

In this thesis, it was demonstrated that atomic force microscopy-based methods can be applied and adapted for the mechanical characterization of different cellulosic materials. Measurements with AFM nanoindentation have the considerable advantage that they can access the material very locally and provide nanoscale insight in complex materials. Furthermore, the implementation of the experiments is possible in a controlled humidity environment, which is an advantage for the investigation of a hygroscopic material like cellulose.

The focus of this thesis was on the development of an AFM-based method to reliably evaluate the viscoelastic properties of cellulosic fibers – especially pulp fibers – in specific directions and at different moisture conditions.

To achieve this goal, contact mechanics have been combined with a phenomenological viscoelastic model, consisting of springs and dashpots. The interaction between the AFM tip and the sample surface needs to be carefully described – especially for rough surfaces like cellulose fibers. Here, the Johnson-Kendall-Roberts (JKR) model was applied since the adhesion force of the surface was too high to be neglected. To eliminate the influence of roughness – which is crucial for a well-defined contact – the surface of the sample has been plastically pre-deformed before the viscoelastic properties have been tested. For the viscoelasticity, the Generalized Maxwell (GM) model, which is a standard material model for polymers, proved to be the best choice for the experimental data.

First, the AFM-based method has been tested with well-known polymers (PMMA and PC) and the results have been compared to NI and tensile testing. This validation of the method was successful, the AFM results correlated well with the NI results. For tensile testing, differences have been found, which can be explained by the difference in deformation. Here, the whole sample is in tension, whereas in AFM-based methods and in NI the surface is locally compressed, hence the local plastic deformation is hindered by the undeformed surrounding material.

Finally, the procedure has been applied to cellulosic fibers at different humidity conditions. Here, experiments have been obtained in the transverse direction as well as for the S2 layer of the fiber in longitudinal direction, as illustrated in Figure 5.1. The S2 layer has been accessed by microtome cutting of thin paper strips. For that, the fibers are

embedded in the polymer resin GMA. The investigation of the fiber cuts with Raman spectroscopy revealed that no significant amount of GMA is penetrating the fibers. Furthermore, to confirm that GMA is not influencing the mechanical analysis of the S2 layer, it was also investigated with AFM-NI.
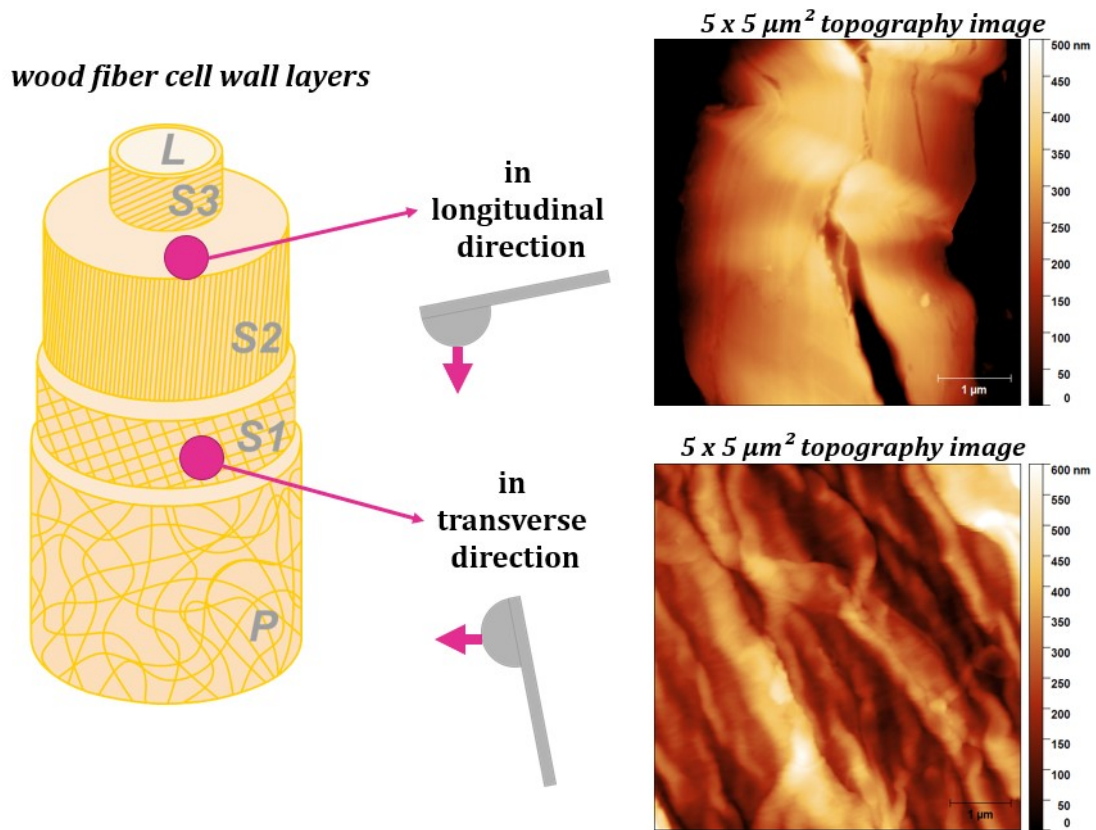

Figure 5.1: Illustration of a wood fiber with its different cell wall layers. The pink dots indicate the layers which have been characterized by the AFM-based viscoelastic method presented in this work. The sketches of the AFM probe indicate the fiber directions in which measurements have been obtained and are accompanied by a representative 5 x 5 μm² topography image of the investigated surfaces.

In transverse direction, pulp and viscose fibers have been studied at five different RH values (10 %, 25 %, 45 %, 60 %, and 75 % RH) as well as in water. Both fiber types show the same trend, the elastic and viscous parameters of the GM2 model decreased with increasing RH and revealed a pronounced drop of a few orders of magnitude in water. The experimental data of the water measurements had to be modeled with a GM3 model containing an additional Maxwell element to achieve adequate fitting quality, whereas for

the experimental data of the viscose fiber the GM2 model was still sufficient. For measurements in water, a poroelastic approach might yield more insight.

In longitudinal direction, viscoelastic behavior of the S2 layer was also revealed, however, not with a pronounced difference to the transverse fiber direction as was initially expected. The maximum applied load during the viscoelastic testing needed to be doubled to achieve indentation depths large enough to not be influenced by thermal drift and noise. The experimental data were evaluated with the GM3 model. The relaxation times were determined to be $\tau_1 = 1\,s$, $\tau_2 = 15\,s$, and $\tau_3 = 240\,s$ – reflecting the experimental window. For the elastic parameters, a decrease with increasing RH was obtained, whereas the viscosities showed only a slight decrease. Here, the measurement in water was not possible due to the swelling of the GMA.

Comparing the results of the transverse direction with the results of the S2 layer in the longitudinal direction reveals only marginal differences. Some of the elastic and viscous parameters have lower values for the transverse direction, but overall, the difference is – surprisingly – smaller than expected. The spectral representation of the data in both directions gives an overview of the data in the frequency range of the experimental window – which is also reflected in the relaxation times. Here, the storage modulus, the loss modulus, and the loss tangent show differences between the two directions. Only at 75 % RH, the spectrum of the loss tangent in longitudinal direction is nearly identical to the transverse direction.

The experimental AFM data proved also to be useful for the development of mechanical models. In a material model for the pulp fiber, the viscoelastic data has been used to describe the matrix properties in transverse direction. Here, the experimental AFM data has been used as an input parameter. Such a model can be applied in paper network simulations or fibers in the dry state when compressibility is not so important.

Another focus of this thesis was on cellulose films. For bending experiments at different RH, a tipless cantilever has been coated with a cellulose film. Changes in RH resulted in the deflection of the cantilever due to the swelling or shrinking of the cellulose film. Validation experiments, however, revealed that the uncoated cantilever also reacts to an RH change. It is unclear if the measured deformations should be attributed to swelling of the cellulose film or humidity effects on the cantilever.

In a further study, it was found that by blending cellulose films with a cellulose derivative interesting morphology can be obtained, and the properties of the films can be

tuned. This is of interest for adsorption studies. The tunability of the mechanical and frictional properties of these films have been investigated at different blending ratios. Due to the phase separation of the films, the morphology is characterized by protrusions and cavities of varying sizes. This leads for the blend films compared to the pure films to an increase in roughness, but to a decrease in friction coefficient as determined by friction force microscopy.

In this thesis, AFM-based methods to explore viscoelasticity have been developed, validated, and adapted to cellulosic materials. To further investigate the time dependent behavior of humid or wet cellulosic materials, poroelasticity might be an interesting approach [58],[139],[140]. Pulp fibers are porous and the accurate measurement of pore radii and their distributions is a very tricky task. With a poroelastic approach, new insights on the permeability and, consequently, the porosity, might be found. Also, the role of different liquids can be investigated.

Although AFM is an excellent method to access local properties of fibers, the sample preparation is a tedious task. The whole method relies very much on the tip-sample interaction and shear and tensile deformation modes are not accessible. Here, Brillouin light scattering microscopy (BLSM) [141] might play an important role in the future and has been proven to be adaptable to cellulose fibers [142]. This non-contact method is based on the interaction of laser light with acoustic phonons and provides viscoelastic properties in the GHz regime. Since the method is based on interaction with light, of course, the spatial resolution cannot be compared to AFM. In material science [143], the BLSM technique is well known and is now gaining a lot of attention from the life science community for cell mechanics [144]. BLSM also provides the possibility to measure the full elastic stiffness tensor [146], [147] – normal and shear stiffnesses in all three dimensions – which is in particular interesting for an anisotropic material like cellulosic fibers. The technique will provide an elegant approach for comprehensive mechanical characterization for cellulosic fibers using one single method, which has not been possible up to now.

6   Appendix A

After [147], the differential equation for a Generalized Maxwell model with *n* elements can be obtained by applying

$$\sigma = E_0\varepsilon + \sum_{i=1}^{n} E_i\eta_i \, (E_i + \eta_i\partial t)^{-1}\dot{\varepsilon} \tag{16}$$

For *n = 3*, the so-called GM3 model, this results in the equation

$$\sigma = A\varepsilon + B\dot{\varepsilon} + C\ddot{\varepsilon} + D\dddot{\varepsilon} - E\dot{\sigma} - F\ddot{\sigma} - G\dddot{\sigma} \tag{17}$$

With the coefficients A, B, C, D, E, F, and G being:

$$A = E_\infty$$

$$B = \left(\frac{E_1\tau_1 + E_2\tau_2 + E_3\tau_3}{E_\infty} + \tau_1 + \tau_2 + \tau_3\right)E_\infty$$

$$C = \tau_1\tau_2(E_\infty + E_1 + E_2) + \tau_1\tau_3(E_\infty + E_1 + E_3) + \tau_2\tau_3(E_\infty + E_2 + E_3)$$

$$D = \tau_1\tau_2\tau_3 E_0$$

$$E = \tau_1 + \tau_2 + \tau_3$$

$$F = \tau_1\tau_2 + \tau_1\tau_3 + \tau_2\tau_3$$

$$G = \tau_1\tau_2\tau_3$$

7 List of Publications

C. Czibula, C. Ganser, M. Kratzer, R. Schennach, B. Friedel, C. Teichert, "Exploring Paper/AgNW based composites for photovoltaic devices by atomic force microscopy methods" in: Schabel, H.J. Schaffrath (eds.) "Progress in Paper Physics Seminar 2016 Conference Proceedings", Darmstadt, 2016, pp. 213-216, ISBN: 978-3-00-054001-1.

C. Czibula, C. Ganser, M. Kratzer, C. Teichert, R. Schennach, M. Penn, M. Ebner, M. Pramstrahler, F. Pilat, T. Chien, B. Friedel, "Silver Nanowires: A Versatile Tool for Conductive Paper", in: "Advances in Pulp and Paper Research vol. 2", (eds. W. Batchelor, D. Söderberg), Transactions of the Fundamental Research Symposium held in Oxford 2017, pp. 723-737, ISBN: 978-0-9926163-3-5.

C. Czibula, C. Ganser, D. Tscharnuter, T. Schöberl, C. Teichert, U. Hirn, "Investigating the transversal viscoelastic properties of paper fibers by atomic force microscopy", in "The issues in mechanics of pulp and paper materials", Proceedings of 4th Int. Conf. in memory of Prof. Valery Komarov, Arkhangelsk, Russia, Sept. 14-16 2017, pp. 74-79, ISBN: 978-5-261-01081-4.

C. Ganser, **C. Czibula**, D. Tscharnuter, T. Schöberl, C. Teichert, U. Hirn, "Combining adhesive contact mechanics with a viscoelastic material model to probe local material properties by AFM", *Soft matter* **14** (2018) 140-150.

C. Czibula, G. Teichert, M. Nau, M. Hobisch, C. Palasingh, M. Biesalski, S. Spirk, C. Teichert, T. Nypelö, "Design of Friction, Morphology, Wetting, and Protein Affinity by Cellulose Blend Thin Film Composition", *Front. Chem.* **7** (2019) 239.

T. Seidhofer, **C. Czibula**, C. Teichert, C. Payerl, U. Hirn, M. Ulz, "A minimal continuum representation of a transverse isotropic viscoelastic pulp fibre based on micromechanical measurements", *Mech. Of Mat.* **135** (2019) 149-161.

C. Czibula, C. Ganser, T. Seidlhofer, C. Teichert, U. Hirn, "Transverse viscoelastic properties of pulp fibers investigated with an atomic force microscopy method", *J. Mater. Sci.* **54** (2019) 11448-61.

C. Czibula, C. Ganser, T. Seidlhofer, C. Teichert, U. Hirn, "Transverse viscoelastic properties of pulp fibers investigated with atomic force microscopy", in "The issues in mechanics of pulp and paper materials", Proceedings of 5th Int. Conf. in memory of Prof. Valery Komarov, Arkhangelsk, Russia, Sept. 11-14 2019, pp. 60-64, ISBN: 978-5-6042336-6-5.

K. Elsayad, G. Urstöger, **C. Czibula**, C. Teichert, J. Gumulec, J. Balvan, M. Pohlt, U. Hirn, "Mechanical properties of cellulose fibers measured by Brillouin spectroscopy", *Cellulose* (2020) https://doi.org/10.1007/s10570-020-03075-z.

T. Seidlhofer, **C. Czibula**, C. Teichert, U. Hirn, M. Ulz, "Compressible plasticity material model for pulp fibers", submitted to *Mech. Of Mat.* (2020).

C. Czibula, A. Brandberg, A. Matković, O. Glyshko, U. Hirn, C. Teichert, "Characterization of the S2 layer in longitudinal direction", in preparation for *Cellulose* (2020).

C. Czibula, C. Ganser, T. Seidlhofer, C. Teichert, U. Hirn, "Viscoelastic characterization of the S2 layer of pulp fibers" in preparation for *J. Mater Sci.* (2020).

B. Prem, **C. Czibula**, R. Saf, R. Supplit, A. Holzner, C. Mayrhofer, C. Teichert, G. Trimmel, "Influence of the blend ratio on the mechanical properties of elastomer-thermoplastic blends" in preparation (2020).

P. Christöfl, **C. Czibula**, M. Berer, G. Oreski, C. Teichert, G. Pinter, "Merging nanoindentation with AFM and compression test on PMMA to probe local viscoelastic material properties" in preparation for *Soft Matter* (2020).

8 Acknowledgments

9 Literature

[1] Eder, M., Arnould, O., Dunlop, J. W. C. C., Hornatowska, J., Salmén, L. "Experimental Micromechanical Characterisation of Wood Cell Walls." *Wood Sci. Technol.*, **47**, 1, (2013) 163–182.

[2] Kolseth, P., de Ruvo, A. *An Attempt to Measure the Torsional Strength of Single Wood Pulp Fibres*.

[3] Wimmer, R., Lucas, B. H., Tsui, T. Y., Oliver, W. C. "Longitudinal Hardness and Young's Modulus of Spruce Tracheid Secondary Walls Using Nanoindentation Technique." *Wood Sci. Technol.*, **31**, 2, (1997) 131–141.

[4] Gindl, W., Gupta, H. S., Schöberl, T., Lichtenegger, H. C., Fratzl, P. "Mechanical Properties of Spruce Wood Cell Walls by Nanoindentation." *Appl. Phys. A Mater. Sci. Process.*, **79**, 8, (2004) 2069–2073.

[5] Gindl, W., Schöberl, T., Scho, T. "The Significance of the Elastic Modulus of Wood Cell Walls Obtained from Nanoindentation Measurements." *Compos. Part A Appl. Sci. Manuf.*, **35**, (2004) 1345–1349.

[6] Gindl, W., Gupta, H. S., Grünwald, C. "Lignification of Spruce Tracheid Secondary Cell Walls Related to Longitudinal Hardness and Modulus of Elasticity Using Nano-Indentation." *Can. J. Bot.*, (2002) 1029–1033.

[7] Adusumalli, R. B., Mook, W. M., Passas, R., Schwaller, P., Michler, J. "Nanoindentation of Single Pulp Fibre Cell Walls." *J. Mater. Sci.*, **45**, 10, (2010) 2558–2563.

[8] Ganser, C., Hirn, U., Rohm, S., Schennach, R., Teichert, C. "AFM Nanoindentation of Pulp Fibers and Thin Cellulose Films at Varying Relative Humidity." *Holzforschung*, **68**, 1, (2014) 53–60.

[9] Ganser, C., Teichert, C. "AFM-Based Nanoindentation of Cellulosic Fibers." In *Applied Nanoindentation in Advanced Materials*; Tiwari, A., Ed.; Wiley; pp 247–267.

[10] Schmied, F. J., Teichert, C., Kappel, L., Hirn, U., Schennach, R. "Joint Strength Measurements of Individual Fiber-Fiber Bonds: An Atomic Force Microscopy Based Method." *Rev. Sci. Instrum.*, **83**, 7, (2012) 1–8.

[11] Fischer, W. J., Hirn, U., Bauer, W., Schennach, R. "Testing of Individual Fiber-Fiber Joints under Biaxial Load and Simultaneous Analysis of Deformation." *Nord. Pulp Pap. Res. J.*, **27**, 2, (2012) 237–244.

[12] Persson, B. N. J., Ganser, C., Schmied, F., Teichert, C., Schennach, R., Gilli, E., Hirn, U. "Adhesion of Cellulose Fibers in Paper." *J. Phys. Condens. Matter*, **25**, 4, (2013) 045002.

[13] Hirn, U., Schennach, R. "Comprehensive Analysis of Individual Pulp Fiber Bonds Quantifies the Mechanisms of Fiber Bonding in Paper." *Sci. Rep.*, **5**, 1, (2015) 10503.

[14] Gibson, L. J. "The Hierarchical Structure and Mechanics of Plant Materials." *J. R. Soc. Interface*, **9**, 76, (2012) pp 2749-2766.

[15] Taiz, L., Zeiger, E., Moller, I., Murphy, A. *Plant Physiology and Development*; Sinauer Associates: Sunderland, MA.

[16] Salmén, L. "Wood Cell Wall Structure and Organisation in Relation to Mechanics." In *Plant Biomechanics*; Geitmann, A., Gril, J., Eds.; Springer: Cham; pp 3–19.

[17] Chang, M. C. "Harnessing Energy from Plant Biomass." *Current Opinion in Chemical Biology*. December 2007, pp 677–684.

[18] Conference Catch Up http://sydney.edu.au/environment-institute/blog/conference-catch-up/ (accessed Nov 27, 2019).

[19] Niklas, K. *Plant Biomechanics: An Engineering Approach to Plant Form and Function*; University of Chicago press.

[20] Conners, T. E. "Wood: Ultrastructure." *Encycl. Mater. Sci. Technol.*, **7**, (2004) 9751–9759.

[21] Reza, M., Ruokolainen, J., Vuorinen, T. "Out-of-Plane Orientation of Cellulose Elementary Fibrils on Spruce Tracheid Wall Based on Imaging with High-Resolution Transmission Electron Microscopy." *Planta*, **240**, 3, (2014) 565–573.

[22] Kollmann, F. F. P., Kuenzi, E. W., Stamm, A. J. *Principles of Wood Science and Technology*.

[23] Stroock, A. D., Pagay, V. V., Zwieniecki, M. A., Michele Holbrook, N. "The Physicochemical Hydrodynamics of Vascular Plants." *Annu. Rev. Fluid Mech.*, **46**, 1, (2014) 615–642.

[24] Lee, J., Holbrook, N. M., Zwieniecki, M. A. "Ion Induced Changes in the Structure of Bordered Pit Membranes." *Front. Plant Sci.*, **3**, (2012) 55.

[25] Ilvessalo-Pfäffli, M.-S. *Fiber Atlas. Identification of Papermaking Fibers*; Springer: Berlin, Heidelberg.

[26] *Paper Physics*; Niskanen, K., Ed.; Finnish Paper Engineer's Association/ Paperi ja Puu Oy.

[27] Weber, F., Koller, G., Schennach, R., Bernt, I., Eckhart, R. "The Surface Charge of Regenerated Cellulose Fibres." *Cellulose*, **20**, 6, (2013) 2719–2729.

[28] *Handbook of Textile Fibre Structure: Volume 2: Natural, Regenerated, Inorganic and Specialist Fibres*; Eichhorn, S. J., Hearle, J. W. S., Jaffe, M., Kikutani, T., Eds.; Woodhead Publishing Limited: Cambridge.

[29] Klemm, D., Heublein, B., Fink, H.-P. P., Bohn, A. *Cellulose: Fascinating Biopolymer and Sustainable Raw Material*; Vol. 44, pp 3358–3393.

[30] Smole, M. S., Peršin, Z., Kreže, T., Kleinschek, K. S., Ribitsch, V., Neumayer, S. "X-Ray Study of Pre-Treated Regenerated Cellulose Fibres." *Mater. Res. Innov.*, **7**, 5, (2003) 275–282.

[31] Jiang, G., Huang, W., Li, L., Wang, X., Pang, F., Zhang, Y., Wang, H. "Structure and Properties of Regenerated Cellulose Fibers from Different Technology Processes." *Carbohydr. Polym.*, **87**, 3, (2012) 2012–2018.

[32] Saito, T., Hirota, M., Tamura, N., Isogai, A. "Oxidation of Bleached Wood Pulp by TEMPO/NaClO/NaClO$_2$ System: Effect of the Oxidation Conditions on Carboxylate Content and Degree of Polymerization." *J. Wood Sci.*, **56**, 3, (2010) 227–232.

[33] Schaub, M., Wenz, G., Wegner, G., Stein, A., Klemm, D. "Ultrathin Films of Cellulose on Silicon Wafers." *Adv. Mater.*, **5**, 12, (1993) 919–922.

[34] Kontturi, E., Thu, P. C., Niemantsverdriet, J. W. "Cellulose Model Surfaces - Simplified Preparation by Spin Coating and Characterization by X-Ray Photoelectron Spectroscopy, Infrared Spectroscopy, and Atomic Force Microscopy." **19**, (2003) 5735–5741.

[35] Rohm, S., Hirn, U., Ganser, C., Teichert, C., Schennach, R. "Thin Cellulose Films as a Model System for Paper Fibre Bonds." *Cellulose*, **21**, 1, (2014) 237–249.

[36] Strasser, S., Niegelhell, K., Kaschowitz, M., Markus, S., Kargl, R., Stana-Kleinschek, K., Slugovc, C., Mohan, T., Spirk, S. "Exploring Nonspecific Protein Adsorption on Lignocellulosic Amphiphilic Bicomponent Films." *Biomacromolecules*, **17**, 3, (2016) 1083–1092.

[37] Niegelhell, K., Süßenbacher, M., Sattelkow, J., Plank, H., Wang, Y., Zhang, K., Spirk, S. "How Bound and Free Fatty Acids in Cellulose Films Impact Nonspecific Protein Adsorption." *Biomacromolecules*, **18**, 12, (2017) 4224–4231.

[38] Kontturi, E., Spirk, S. "Ultrathin Films of Cellulose: A Materials Perspective." *Front. Chem.*, **7**, July, (2019) 1–18.

[39] Kontturi, E., Nyfors, L., Laine, J. "Utilizing Polymer Blends to Prepare Ultrathin Films with Diverse Cellulose Textures." *Macromol. Symp.*, **294**, 2, (2010) 45–50.

[40] Nyfors, L., Suchy, M., Laine, J., Kontturi, E. "Ultrathin Cellulose Films of Tunable Nanostructured Morphology with a Hydrophobic Component." *Biomacromolecules*, **10**, 5, (2009) 1276–1281.

[41] Czibula, C., Teichert, G., Nau, M., Hobisch, M., Palasingh, C., Biesalski, M., Spirk, S., Teichert, C., Nypelö, T. "Design of Friction, Morphology, Wetting, and Protein Affinity by Cellulose Blend Thin Film Composition." *Front. Chem.*, **7**, May, (2019) 1–10.

[42] Nägeli, C., Nägeli, K. W. "Die Stärkekörner: Morphologische, Physiologische, Chemisch-Physikalische Und Systematisch-Botanische Monographie." *Pflanzenphysiologische Untersuchungen*, No. 2 (1858) 623 pp.

[43] Skaar, C. *Wood-Water Relations*; Springer: Berlin, Heidelberg.

[44] Perkitny, T., Kingston, R. S. T. "Review of the Sufficiency of Research on the Swelling Pressure of Wood." *Wood Sci. Technol.*, **6**, 3, (1972) 215–229.

[45] Virta, J., Koponen, S., Absetz, I. "Measurement of Swelling Stresses in Spruce (Picea Abies) Samples." *Build. Environ.*, **41**, 8, (2006) 1014–1018.

[46] Ispas, M. "Experimental Investigations on Swelling Pressure of Natural and Heat-Treated Ash Wood." *Bull. Transilv. Univ. Brasov*, **6**, 1, (2013) 55–62.

[47] Moliński, W., Raczkowski, J. "Mechanical Stresses Generated by Water Adsorption in Wood and Their Determination by Tension Creep Measurements." *Wood Sci. Technol.*, **22**, 3, (1988) 193–198.

[48] Necesany, V. "Effect of Some Environmental Factors on the Cell Wall Structure." *Holzforschung*, **25**, 1, (1971) 4–8.

[49] Perkitny, T., Kokociński, W. "Untersuchungen Über Das Eindringen von Wasser Und Das Fortschreiten Der Quellungsenergie in Befeuchteten Holzkörpern." *Holz als Roh- und Werkst.*, **26**, 12, (1968) 469–478.

[50] Krauss, A. "Swelling Pressure of Spruce Wood Along the Grains Moistened in Humid Air or Water." *Folia For. Pol. Ser. B*, **35**, (2004) 13–22.

[51] Nečesaný, V. "Der Quellungsdruck von Holz Und Seinen Bestandteilen." *Eur. J. Wood Wood Prod.*, **23**, 5, (1965) 183–187.

[52] Rybarczyk, W., Ganowicz, R. "A Theoretical Description of the Swelling Pressure of Wood." *Wood Sci. Technol.*, **8**, 3, (1974) 233–241.

[53] Stamm, A. J. *Colloidal Chemistry of Cellulosic Materials*; U.S. Dept. of Agriculture.

[54] Lopez-Sanchez, P., Rincon, M., Wang, D., Brulhart, S., Stokes, J. R., Gidley, M. J. "Micromechanics and Poroelasticity of Hydrated Cellulose Networks." *Biomacromolecules*, **15**, 6, (2014) 2274–2284.

[55] Isobe, N., Kimura, S., Wada, M., Deguchi, S. "Poroelasticity of Cellulose Hydrogel." *J. Taiwan Inst. Chem. Eng.*, **92**, (2018) 118–122.

[56] Li, J., Illeperuma, W. R. K., Suo, Z., Vlassak, J. J. "Hybrid Hydrogels with Extremely High Stiffness and Toughness." *ACS Macro Lett.*, **3**, 6, (2014) 520–523.

[57] Helfricht, N., Doblhofer, E., Bieber, V., Lommes, P., Sieber, V., Scheibel, T., Papastavrou, G. "Probing the Adhesion Properties of Alginate Hydrogels: A New Approach towards the Preparation of Soft Colloidal Probes for Direct Force Measurements." *Soft Matter*, **13**, 3, (2017) 578–589.

[58] Oyen, M. L. "Mechanical Characterisation of Hydrogel Materials." *Int. Mater. Rev.*, **59**, 1, (2014) 44–59.

[59] Pelton, R. "A Model of the External Surface of Wood Pulp Fibers." *Nord. Pulp Pap. Res. J.*, **8**, 1, (1993) 113–119.

[60] Scallan, A. M., Grignon, J. "The Effect of Cations on Pulp and Paper Properties." *Sven. Papperstidning*, **2**, (1979) 40–47.

[61] Banks, H. T., Hu, S., Kenz, Z. R. "A Brief Review of Elasticity and Viscoelasticity for Solids." *Adv. Appl. Math. Mech.*, **3**, 1, (2011) 1–51.

[62] Roylance, D. *Engineering Viscoelasticity*; Cambridge.

[63] Vincent, J. *Structural Biomaterials*; Princeton University Press: Princeton.

[64] Cisse, O., Placet, V., Guicheret-Retel, V., Trivaudey, F. F., Boubakar, M. L. "Creep Behaviour of Single Hemp Fibres. Part I: Viscoelastic Properties and Their Scattering under Constant Climate." *J. Mater. Sci.*, **50**, 4, (2015) 1996–2006.

[65] Flügge, W. *Viscoelasticity*; Springer.

[66] Hardin, B. O. "The Nature of Damping in Sands." *J. Soil Mech. Found. Div*, **92**,.

[67] Ganser, C., Czibula, C., Tscharnuter, D., Schöberl, T., Teichert, C., Hirn, U. "Combining Adhesive Contact Mechanics with a Viscoelastic Material Model to Probe Local Material Properties by AFM." *Soft Matter*, **14**, 1, (2018) 140–150.

[68] Czibula, C., Ganser, C., Seidlhofer, T., Teichert, C., Hirn, U. "Transverse Viscoelastic Properties of Pulp Fibers Investigated with an Atomic Force Microscopy Method." *J. Mater. Sci.*, **54**, 17, (2019) 11448–11461.

[69] Butt, H. J., Kappl, M. *Surface and Interfacial Forces*; Wiley-VCH Verlag: Weinheim.

[70] Hertz, H. "Ueber Die Berührung Fester Elastischer Körper." *J. Reine Angew. Math.*, **92**, (1881) 156–171.

[71] Johnson, K. L., Kendall, K., Roberts, A. D. "Surface Energy and the Contact of Elastic Solids." *Proc. R. Soc. A Math. Phys. Eng. Sci.*, **324**, 1558, (1971) 301–313.

[72] Klapetek, P. *Quantitative Data Processing in Scanning Probe Microscopy*, 2nd ed.; Elsevier: Amsterdam.

[73] Chyasnavichyus, M., Young, S. L., Tsukruk, V. V. "Probing of Polymer Surfaces in the Viscoelastic Regime." *Langmuir*, **30**, 35, (2014) 10566–10582.

[74] Chyasnavichyus, M., Young, S. L., Geryak, R., Tsukruk, V. V. "Probing Elastic Properties of Soft Materials with AFM: Data Analysis for Different Tip Geometries." *Polym. (United Kingdom)*, (2015) 1–9.

[75] Oliver, W. C., Pharr, G. M., Oliver, W. C., Pharr, G. M. "An Improved Technique for Determining Hardness and Elastic Modulus Using Load and Displacement Sensing Indentation Experiments." *J. Mater. Res.*, **7**, 6, (1992) 1564–1583.

[76] Yan, D., Li, K. "Conformability of Wood Fiber Surface Determined by AFM Indentation." *J Mater. Sci.*, **48**, 1, (2013) 322–331.

[77] Binnig, G., Quate, C. F., Gerber, C. "Atomic Force Microscope." *Phys. Rev. Lett.*, **56**, (1986) 930.

[78] Putman, C. A. J., Van der Werf, K. O., De Grooth, B. G., Van Hulst, N. F., Greve, J. "Tapping Mode Atomic Force Microscopy in Liquid." *Appl. Phys. Lett.*, **64**, 18, (1994) 2454–2456.

[79] Schmitz, I., Schreiner, M., Friedbacher, G., Grasserbauer, M. "Phase Imaging as an Extension to Tapping Mode AFM for the Identification of Material Properties on Humidity-Sensitive Surfaces." *Appl. Surf. Sci.*, **115**, 2, (1997) 190–198.

[80] Raghavan, D., Gu, X., Nguyen, T., Van Landingham, M., Karim, A. "Mapping Polymer Heterogeneity Using Atomic Force Microscopy Phase Imaging and Nanoscale Indentation." *Macromolecules*, **33**, 7, (2000) 2573–2583.

[81] Teichert, C., Haas, A., Wallner, G. M., Lang, R. W. "Nanometer Scale Characterization of Polymer Films by Atomic-Force Microscopy." *Macromol. Symp.*, **181**, 1, (2002) 457–466.

[82]   Tamayo, J., García, R. "Deformation, Contact Time, and Phase Contrast in Tapping Mode Scanning Force Microscopy." *Langmuir*, **12**, 18, (1996) 4430–4435.

[83]   Butt, H. J., Cappella, B., Kappl, M. "Force Measurements with the Atomic Force Microscope: Technique, Interpretation and Applications." *Surf. Sci. Rep.*, **59**, 1–6, (2005) 1–152.

[84]   Villarrubia, J. S. "Morphological Estimation of Tip Geometry for Scanned Probe Microscopy." *Surf. Sci.*, **321**, (1994) 287–300.

[85]   Ganser, C. "Influence of Water on Mechanical Properties of Cellulosic Materials Studied by AFM Based Methods," Montanuniversitaet Leoben.

[86]   Aspelmeyer, M., Kippenberg, T. J., Marquardt, F. "Cavity Optomechanics." *Rev. Mod. Phys.*, **86**, 4, (2014) 1391–1452.

[87]   Lang, H. P., Ramseyer, J. P., Grange, W., Braun, T., Schmid, D., Hunziker, P., Jung, C., Hegner, M., Gerber, C. "An Artificial Nose Based on Microcantilever Array Sensors." *J. Phys. Conf. Ser.*, **61**, 1, (2007) 663–667.

[88]   Huber, F., Lang, H. P., Backmann, N., Rimoldi, D., Gerber, C. "Direct Detection of a BRAF Mutation in Total RNA from Melanoma Cells Using Cantilever Arrays." *Nat. Nanotechnol.*, **8**, 2, (2013) 125–129.

[89]   Huber, F., Lang, H. P., Zhang, J., Rimoldi, D., Gerber, C. "Nanosensors for Cancer Detection." *Swiss Med Wkly*, **145**, (2015) 14092.

[90]   Lang, H., Baller, M., Berger, R., Gerber, C., Gimzewski, J., Battiston, F., Fornaro, P., Ramseyer, J., Meyer, E., Güntherodt, H. "An Artificial Nose Based on a Micromechanical Cantilever Array." *Anal. Chim. Acta*, **393**, 1–3, (1999) 59–65.

[91]   Paris, O., Burgert, I., Fratzl, P. "Biomimetics and Biotemplating of Natural Materials." *MRS Bull.*, **35**, 3, (2010) 219–225.

[92]   Dawson, C., Vincent, J. F. V., Rocca, A.-M. "How Pine Cones Open." *Nature*, **390**, 6661, (1997) 668–668.

[93]   Elbaum, R., Zaltzman, L., Burgert, I., Fratzl, P. "The Role of Wheat Awns in the Seed Dispersal Unit." *Science*, **316**, 5826, (2007) 884–886.

[94]   Ganser, C., Fritz-Popovski, G., Morak, R., Sharifi, P., Marmiroli, B., Sartori, B., Amenitsch, H., Griesser, T., Teichert, C., Paris, O. "Cantilever Bending Based on Humidity-Actuated Mesoporous Silica/Silicon Bilayers." *Beilstein J. Nanotechnol.*, **7**, (2016) 637–644.

[95]   Paris, O., Lang, D., Li, J., Schumacher, P., Deluca, M., Daniel, R., Tkadletz, M., Schalk, N., Mitterer, C., Todt, J., Keckes, J., Zhang, Z., Fritz-Popovski, G., Ganser, C., Teichert, C., Clemens, H. "Complementary High Spatial Resolution Methods in Materials Science and Engineering." *Adv. Eng. Mater.*, **19**, 4, (2017) 1–22.

[96]   Reyssat, E., Mahadevan, L. "Hygromorphs: From Pine Cones to Biomimetic Bilayers." *J. R. Soc. Interface*, **6**, 39, (2009) 951–957.

[97] Meyer, G., Amer, N. M. "Simultaneous Measurement of Lateral and Normal Forces with an Optical-beam-deflection Atomic Force Microscope." *Appl. Phys. Lett.*, **57**, 20, (1990) 2089–2091.

[98] Mate, C. M., McClelland, G. M., Erlandsson, R., Chiang, S. "Atomic-Scale Friction of a Tungsten Tip on a Graphite Surface." In *Scanning Tunneling Microscopy*; Springer; pp 226–229.

[99] Marti, O., Colchero, J., Mlynek, J. "Combined Scanning Force and Friction Microscopy of Mica." *Nanotechnology*, **1**, 2, (1990) 141–144.

[100] Overney, R. M., Meyer, E., Frommer, J., Brodbeck, D., Lüthi, R., Howald, L., Güntherodt, H.-J., Fujihira, M., Takano, H., Gotoh, Y. "Friction Measurements on Phase-Separated Thin Films with a Modified Atomic Force Microscope." *Nature*, **359**, 10, (1992) 133–135.

[101] Overney, R. M., Meyer, E., Frommer, J., Güntherodt, H.-J. "Force Microscopy Study of Friction and Elastic Compliance of Phase-Separated Organic Thin Films." *Langmuir*, **10**, 4, (1994) 1281–1286.

[102] Hlawacek, G., Shen, Q., Teichert, C., Lex, A., Trimmel, G., Kern, W. "Hierarchy of Adhesion Forces in Patterns of Photoreactive Surface Layers." *J. Chem. Phys.*, **130**, 4, (2009).

[103] Shen, Q., Edler, M., Griesser, T., Knall, A.-C. C., Trimmel, G., Kern, W., Teichert, C. "Ex Situ and in Situ Characterization of Patterned Photoreactive Thin Organic Surface Layers Using Friction Force Microscopy." *Scanning*, **36**, 6, (2014) 590–598.

[104] Hammerschmidt, J. A., Moasser, B., Gladfelter, W. L., Haugstad, G., Jones, R. R. "Polymer Viscoelastic Properties Measured by Friction Force Microscopy." *Macromolecules*, **29**, 27, (1996) 8996–8998.

[105] Sondhauß, J., Lantz, M., Gotsmann, B., Schirmeisen, A. "β-Relaxation of PMMA: Tip Size and Stress Effects in Friction Force Microscopy." *Langmuir*, **31**, 19, (2015) 5398–5405.

[106] Fischer, W. J., Zankel, A., Ganser, C., Schmied, F. J., Schroettner, H., Hirn, U., Teichert, C., Bauer, W., Schennach, R. "Imaging of the Formerly Bonded Area of Individual Fibre to Fibre Joints with SEM and AFM." *Cellulose*, **21**, 1, (2014) 251–260.

[107] Ganser, C., Weber, F., Czibula, C., Bernt, I., Schennach, R., Teichert, C. "Tuning Hardness of Swollen Viscose Fibers." *Bioinspired, Biomim. Nanobiomaterials*, **3**, 3, (2014) 131–138.

[108] Wiltsche, M., Donoser, M., Kritzinger, J., Bauer, W. "Automated Serial Sectioning Applied to 3D Paper Structure Analysis." *J. Microsc.*, **242**, 2, (2011) 197–205.

[109] Hirn, U., Kritzinger, J., Bauer, W. "Automated 3D Measurement of Fiber Cross Section Morphology in Handsheets." *Artic. Nord. Pulp Pap. Res. J.*, (2012).

[110] Castellanos-Gomez, A., Buscema, M., Molenaar, R., Singh, V., Janssen, L., van der Zant, H. S. J. J., Steele, G. A. "Deterministic Transfer of Two-Dimensional Materials by All-Dry Viscoelastic Stamping." *2D Mater.*, **1**, 1, (2014) 1–34.

104

[111] Hutter, J. L., Bechhoefer, J. "Calibration of Atomic-Force Microscopy Tips." *Rev. Sci. Instrum.*, **64**, 7, (1993) 1868.

[112] Seidlhofer, T., Czibula, C., Payerl, C., Teichert, C., Hirn, U., Ulz, M. H. "A Minimal Continuum Representation of a Transverse Isotropic Viscoelastic Pulp Fibre Based on Micromechanical Measurements." *Mech. Mater.*, **135**, May, (2019) 149–161.

[113] Lakes, R. *Viscoelastic Materials*; Cambridge University Press: New York.

[114] Kalihari, V., Haugstad, G., Frisbie, C. D. "Distinguishing Elastic Shear Deformation from Friction on the Surfaces of Molecular Crystals." *Phys. Rev. Lett.*, **104**, 8, (2010) 086102.

[115] Klünsner, T., Shen, Q., Hlawacek, G., Teichert, C., Fateh, N., Fontalvo, G. A., Mitterer, C. "Morphology Characterization and Friction Coefficient Determination of Sputtered V_2O_5 Films." *Thin Solid Films*, **519**, 4, (2010) 1416–1420.

[116] Varenberg, M., Etsion, I., Halperin, G. "An Improved Wedge Calibration Method for Lateral Force in Atomic Force Microscopy." *Rev. Sci. Instrum.*, **74**, 7, (2003) 3362–3367.

[117] Nečas, D., Klapetek, P. "Gwyddion: An Open-Source Software for SPM Data Analysis." *Open Phys.*, **10**, 1, (2012) 181–188.

[118] Czibula, C., Seidlhofer, T., Ganser, C., Teichert, C., Hirn, U. "AFM-Based Low Frequency Viscoelastic Characterization of Wood Pulp Fibers at Different Relative Humidity." *Prep.*, (2020).

[119] Hindmarsh, A. C. "ODEPACK, A Systematized Collection of ODE Solvers." In *IMACS Transactions on Scientific Computation*; Stepleman, R. S., Ed.; Scientific Computing: North-Holland, Amsterdam; Vol. 1, pp 55–64.

[120] Levenberg, K. "A Method for the Solution of Certain Non-Linear Problems in Least Squares." *Q. Appl. Math.*, **2**, 2, (1944) 164–168.

[121] Park, S. W., Schapery, R. A. "Methods of Interconversion between Linear Viscoelastic Material Functions. Part I - A Numerical Method Based on Prony Series." *Int. J. Solids Struct.*, **36**, 11, (1999) 1653–1675.

[122] Renaud, F., Dion, J. L., Chevallier, G., Tawfiq, I., Lemaire, R. "A New Identification Method of Viscoelastic Behavior: Application to the Generalized Maxwell Model." *Mech. Syst. Signal Process.*, **25**, 3, (2011) 991–1010.

[123] Briscoe, B. J., Fiori, L., Pelillo, E. "Nano-Indentation of Polymeric Surfaces." *J. Phys. D Appl. Phys.*, **31**, 19, (1998) 2395.

[124] Jee, A.-Y., Lee, M. "Comparative Analysis on the Nanoindentation of Polymers Using Atomic Force Microscopy." *Polym. Test.*, **29**, 1, (2010) 95–99.

[125] Ganser, C. "Surface Characterization of Cellulose Fibers by Atomic Force Microscopy in Liquid Media and under Ambient Conditions," Montanuniversitaet Leoben.

[126] Wild, P., Omholt, I., Steinke, D., Schuetze, A. "Experimental Characterization of the Behaviour of Wet Single Wood-Pulp Fibres under Transverse Compression." *J. Pulp Pap. Sci.*, **31**, (2005) 116–120.

[127] Hartler, N., Nyrén, J. "Transverse Compressibility of Pulp Fibers. 2. Influence of Cooking Method, Yield, Beating, and Drying." *Tappi*, **53**, 5, (1970) 820–823.

[128] Dunford, J. A., Wild, P. M. "Cyclic Transverse Compression of Single Wood-Pulp Fibres." *J Pulp Pap. Sci*, **28**, 4, (2002) 136–141.

[129] Scallan, A. M., Tigerström, A. "Swelling and Elasticity of the Cell Wall of Pulp Fibres." *J. Pulp Pap. Sci.*, **18**, 5, (1992) 188–193.

[130] Nilsson, B., Wagberg, L., Gray, D. "Conformability of Wet Pulp Fibres at Small Length Scales." In *Proc. 12th Fundamental Research Symposium*; Oxford; pp 211–224.

[131] Pettersson, T., Hellwig, J., Gustafsson, P.-J., Stenström, S. "Measurement of the Flexibility of Wet Cellulose Fibres Using Atomic Force Microscopy." *Cellulose*, **24**, 10, (2017) 4139–4149.

[132] Kenealy, W. R., Jeffries, T. W. "Enzyme Processes for Pulp and Paper: A Review of Recent Developments." In *ACS Symposium Series*; Vol. 845, pp 210–239.

[133] Clarke, J. H., Davidson, K., Rixon, J. E., Halstead, J. R., Fransen, M. P., Gilbert, H. J., Hazlewood, G. P. "A Comparison of Enzyme-Aided Bleaching of Softwood Paper Pulp Using Combinations of Xylanase, Mannanase and α-Galactosidase." *Appl. Microbiol. Biotechnol.*, **53**, 6, (2000) 661–667.

[134] Yeni, Y. N., Yerramshetty, J., Akkus, O., Pechey, C., Les, C. M. "Effect of Fixation and Embedding on Raman Spectroscopic Analysis of Bone Tissue." *Calcif. Tissue Int.*, **78**, 6, (2006) 363–371.

[135] Gindl, W., Konnerth, J., Schöberl, T. "Nanoindentation of Regenerated Cellulose Fibres." *Cellulose*, **13**, (2006) 1–7.

[136] Emerson, J. A., Garabedian, N. T., Moore, A. C., Burris, D. L., Furst, E. M., Epps, T. H. "Unexpected Tribological Synergy in Polymer Blend Coatings: Leveraging Phase Separation to Isolate Domain Size Effects and Reduce Friction." *ACS Appl. Mater. Interfaces*, **9**, 39, (2017) 34480–34488.

[137] Teichert, C. "Self-Organization of Nanostructures in Semiconductor Heteroepitaxy." *Physics Report*. 2002, pp 335–432.

[138] Bogdanovic, G., Tiberg, F., Rutland, M. W. "Sliding Friction between Cellulose and Silica Surfaces." *Langmuir*, **17**, 19, (2001) 5911–5916.

[139] Galli, M., Comley, K. S. C., Shean, T. A. V., Oyen, M. L. "Viscoelastic and Poroelastic Mechanical Characterization of Hydrated Gels." *J. Mater. Res.*, **24**, 03, (2009) 973–979.

[140] Wahlquist, J. A., DelRio, F. W., Randolph, M. A., Aziz, A. H., Heveran, C. M., Bryant, S. J., Neu, C. P., Ferguson, V. L. "Indentation Mapping Revealed Poroelastic, but Not Viscoelastic, Properties Spanning Native Zonal Articular Cartilage." *Acta Biomater.*, **64**, (2017) 41–49.

[141] Brillouin, L. "Diffusion de La Lumière et Des Rayons X Par Un Corps Transparent Homogène." *Ann. Phys. (Paris).*, **9**, 17, (1922) 88–122.

[142] Elsayad, K., Urstöger, G., Czibula, C., Teichert, C., Gumulec, J., Balvan, J., Pohlt, M., Hirn, U. "Mechanical Properties of Cellulose Fibers Measured by Brillouin Spectroscopy." *Cellulose*, (2020) 1–12.

[143] Koski, K. J., Yarger, J. L. "Brillouin Imaging." *Appl. Phys. Lett.*, **87**, 6, (2005).

[144] Elsayad, K. "Trends in Cell Biology Probing Mechanical Properties in Biology Using Brillouin Microscopy Trends in Cell Biology." *Trends Cell Biol.*, **29**, 8, (2019) 608–611.

[145] Koski, K. J., Akhenblit, P., McKiernan, K., Yarger, J. L. "Non-Invasive Determination of the Complete Elastic Moduli of Spider Silks." *Nat. Mater.*, **12**, 3, (2013) 262–267.

[146] Williams, D. R., Nurco, D. J., Rahbar, N., Koski, K. J. "Elasticity of Bamboo Fiber Variants from Brillouin Spectroscopy." *Materialia*, **5**, January, (2019) 100240.

[147] Ranz, T. *Elementare Materialmodelle Der Linearen Viskoelastizität Im Zeitbereich*.